Polarisation Observables from Strangeness Photoproduction on a Frozen Spin Target with CLAS at Jefferson Lab

Stuart Fegan

Presented as a Thesis for the Degree of Doctor of Philosophy

Nuclear Physics Group

School of Physics and Astronomy

University of Glasgow

Abstract

This thesis presents the first, preliminary, measurements of the Σ and G polarisation observables from strangeness photoproduction on a frozen spin polarised target, for the reactions $\gamma p \rightarrow K^{+}\Lambda$ and $\gamma p \rightarrow K^{+}\Sigma^{0}$. The data were collected at the Thomas Jefferson National Accelerator Facility using the CLAS detector in Experimental Hall B in conjunction with the FROST longitudinally polarised frozen spin target and a linearly polarised photon beam in the energy range W = 1.66 to 2.32 GeV.

The work forms part of a wider experimental program seeking to obtain experimental data on the excitation spectrum of the nucleon in order to better understand its structure via the measurement of polarisation observables, whose sensitivity to resonances makes them a desirable quantity to measure. By studying strangeness reactions, it may be possible to find "missing" baryon resonances, predicted by symmetric quark models but not observed in previous experiments, whose results are consistent with the di-quark model. It is thought these "missing" resonances remain undiscovered because they have different coupling strengths for different reaction channels, such as the strangeness reactions, whereas the current data is dominated by studies of πN reactions.

Measurements of the photon asymmetry, Σ, have been made which agree with previous CLAS measurements, validating the use of the FROST polarised target for the measurement of other polarisation observables, such as the G beam-target double observable. The G observable was measured on the FROST target via two techniques; from beam asymmetry measurements for the two available states of target polarisation, and a novel double asymmetry method intended to combine all the available polarised data.

Some inconsistencies between the G measurements for each state of target polarisation are observed, particularly at forward angles, and are much greater once dilution effects from the target material are accounted for. As well as these dilution effects, the double asymmetry technique is also limited by insufficient constraint of the associated parameters from the limited data available on the reactions studied.

For $K^+\Lambda$, the results are compared to the Kaon-MAID isobaric model calculations, both with and without the inclusion of the missing D_{13} resonance. Both calculations are inconclusive when compared with the data, although at higher energies the calculation without the D_{13} state better matches the trend of the results. For $K^+\Sigma$, the model prediction, which does not include any missing states, shows agreement with the trend of the data for some of the energy bins. In light of this new data, refitting of the models should be undertaken, as the next step in the theoretical interpretation of these results.

These measurements provide new information to the world dataset of polarisation observables, and with further analysis of the associated systematics of beam polarisation and dilution, the data will provide new insights into the process of strangeness photoproduction.

Declaration

The data presented in this thesis were obtained as part of the g9a collaboration at the Thomas Jefferson National Accelerator Facility, Virginia, USA, and the Nuclear Physics Experimental Group, School of Physics and Astronomy, The University of Glasgow. I participated fully in the preparation and execution of the experiment. The analysis of the experimental data is my own work. This thesis was composed by myself.

Stuart Fegan

October 2011

Acknowledgements

Many people have played a part in the completion of this thesis, if I had unlimited space, and time to remember, I would thank each and every one of you, apologies to anyone offended by their omission.

Firstly, I must thank my supervisors, Prof. Guenther Rosner and Dr. Ken Livingston, for the opportunity to join the Nuclear Physics Group and work on this experiment. Ken's supervision was second to none, and he was usually always there when needed for help and advice, as well as general IT support when I was young and unschooled in the ways of Linux. More importantly, his time spent reading this thesis, and the comments and suggestions made, were greatly appreciated, particularly at the end when he seemed to be spending almost as much time on it as I was. Thanks a million Ken, I'm not sure I could have got there without you.

When Guenther left the group in 2011, Prof. David Ireland stepped in to take over his role as academic supervisor, and deserves a mention. Hopefully it wasn't too much of a task, having already observed my progress in an unofficial capacity.

As if three supervisors wasn't enough, I also had the ability to call upon Bryan McKinnon and David Hamilton for additional support. Bryan's insights were especially useful when it came to the intricacies of CLAS photon analysis, as well as being another pair of eyes to look over the thesis and pick up on things Ken and I might otherwise have missed, while David could always be relied upon for words of encouragement or physics inspiration from a more detached point of view.

At Jefferson Lab, the g9/FROST group deserves thanks for the successful preparation and running of the experiment, as well as interest and feedback as my work progressed. In particular, the comments and suggestions of Eugene Pasyuk, Franz Klein and Mike Dugger provided invaluable insight, for which I am very greatful.

Life at Jefferson Lab would have been a lot duller without the company of my fellow Glasgow "JLabbers"; Craig Paterson, Russell Johnstone, Neil Hassall, Gary Smith and Johan Sjöegren, as well as our Edinburgh colleagues; Daria Sokhan and Jo McAndrew. Thankfully the Plaza Azteca has reopened so future generations can enjoy the same average Mexican food we did on the first night of any trip.

All the staff and students in the Nuclear Physics Group during my time here have contributed to an enjoyable experience, and I'd like to single out my contemporaries, David Howdle and Seian Al Jebali, for special mention. Best wishes to you both for the future, it's been a pleasure to have shared this time with you.

Asides from those already mentioned from room 414, time in the office was also shared with Parada Hutauruk, Joe Mancell, Siân Nutbeam, and Maddalena Boselli, thank you for not getting too annoyed by my loud complaints and quiet muttering.

When I'd done quite enough complaining in the office, the rest of the group would then be subjected to the tyranny of coffee, my attempt at maintaining a long-standing group tradidion of venturing out for caffeinated refreshment. Thanks to David Mahon, Gordon Hill, Euan Cowie, Jen Bowles, Rachel Montgomery, Stef Lewis, Jonathan Burns, Neil Thompson, Jeffrey Phillips, Mark Anderson and all the others who came along every day, or every now and again, for sparing me the indignity of taking coffee alone.

A special mention should also go to the GNU Image Manipulation Program. Handy when it comes to quickly editing images for reports and talks, even handier for grafting faces of NPE members onto a variety of album covers and film posters.

Thanks also to my family and friends outside of nuclear physics for their support and understanding, and conversation that doesn't always lead to polarisation observables and strangeness photoproduction.

Finally, this thesis is dedicated to the memory of my brother, Scott. His interest in how things work was an inspiration to me as a child, and probably the reason I followed a path into science. He remains an inspiration to me today, and not a day goes by where I don't miss him.

"Truth is great and will prevail if left to herself" - Thomas Jefferson

Contents

List of Figures

List of Tables

Chapter 1

Introduction

The work presented here is concerned with the measurement of the Σ beam polarisation observable and the 'G' beam-target double polarisation observable for the reactions $\gamma p \rightarrow K^+\Lambda^0$ and $\gamma p \rightarrow K^+\Sigma^0$ on a polarised butanol (proton) target. The measurements of the Σ observable were also compared to previous data, for verification of the methods used to account for the bound nucleons contained in the molecular target materials used.

The analysis performed here is part of a wider experimental program seeking to obtain experimental data on the excitation spectrum of the nucleon in order to better understand its structure. This opening chapter will discuss the motivation for the extraction of polarisation observables for strangeness photoproduction reactions and review the underlying physics behind the field of nucleon resonance spectroscopy.

1.1 Motivation

Baryon spectroscopy is the study of excited states of the nucleon. These excited states, or resonances, are of interest in the field of hadronic physics as they aid in the study of the internal structure of the nucleon and the interactions of the quarks therein. Such studies require not only a determination of the existence of these states, but a detailed knowledge of their quantum numbers and physical properties.

Figure 1.1 shows the total photoproduction cross section on the proton for several meson production channels. Resonant behaviour can be seen in several reaction

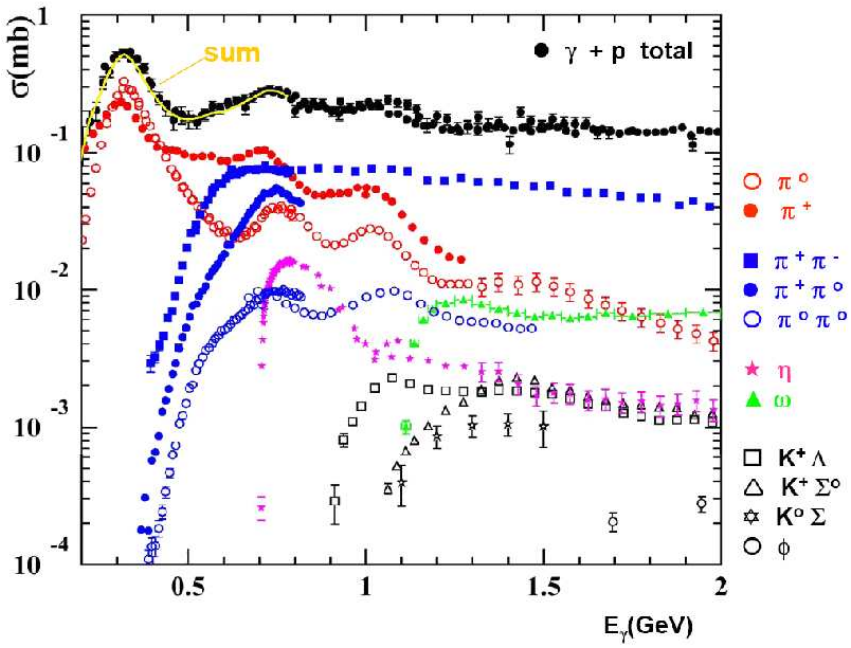

Figure 1.1: Cross-sections on the proton for meson photoproduction in the energy range 0.2 - 2.0 GeV. Resonant structures are visible at several energies for various reaction channels, although many other resonances are hidden in cross section measurements due to the wide and overlapping nature of the contributing states [1].

channels, and several states appear to contribute to the overall measurement.

Phenomenological models of the nucleon, in the energy regime where many resonances exist, are based on non-perturbative descriptions of Quantum Chromodynamics (QCD). These models consider the degrees of freedom of the quarks in the nucleon in order to predict a series of resonances. The differences between these models lead to the prediction of slightly different excitation spectra of the nucleon, which includes several states not seen in the existing data, giving rise to the so-called "Missing Resonance" problem. The experimental observation of these excited states provides evidence favouring or contradicting the models, and allows experimentally consistent models to be improved upon.

By exciting nucleons in a target with an incident electromagnetic beam of sufficient energy, these resonant states can be created and studied from their decay products. Studying an individual resonance requires finding and separating its signature in experimental data from the multitude of other states which are also present. This can be particularly difficult for some states, depending on the width of the cross section, proximity in energy to other states, and the coupling strength to the reaction

studied.

It is clear from figure 1.1 that cross section measurements alone are not sufficient to distinguish the resonance spectrum, and other experimental probes of resonant structure are required. The recent availability of high-quality, high-statistics data from polarised beams and targets at facilities such as Jefferson Lab enable the study of polarisation observables; properties associated with the polarised particles or the polarised photon beam in a reaction, highly sensitive to the presence of resonances. Additionally, strangeness reaction channels, such as $\gamma p \rightarrow K^+\Lambda^0$ and $\gamma p \rightarrow K^+\Sigma^0$, allow the possibility of measuring the polarisation of the recoiling hyperon, providing access to the full set of polarisation observables associated with strangeness photoproduction.

In conjunction with data from complimentary analyses on past, present, and future experiments at the same facility, this work will help facilitate a near model-independent partial wave analysis for strangeness photoproduction; a so-called "Complete Experiment", which is expected to identify "Missing Resonances" if they exist and help determine the baryon spectrum.

1.1.1 Quantum Chromodynamics

The strongly-interacting systems studied by hadronic physics are described by the theory of Quantum Chromodynamics (QCD), which describes strong force interactions in the standard model. QCD is a non-abelian gauge theory of coloured quarks, thought to come in six flavours - up, down, strange, charm, top and bottom.

In the context of the standard model, QCD is able to describe a range of composite sub-atomic particles, known as hadrons, via combinations of these quarks, and account for numerous hadronic states through the arrangement of associated quantum numbers such as isospin and flavour, which have been introduced to the standard model at various points during its development [2].

The introduction of the strangeness quantum number, and attempts to categorise the numerous hadronic states observed by experiment in terms of symmetries led to the grouping of hadrons according to the "eight-fold way" [3], developed independently by Gell-Mann and Ne'eman. This scheme arranged the hadrons into

multiplets of nearly equal masses, along axes of strangeness and charge, as shown in figure 1.2. The connection between this scheme and the resulting correspondence of the then-known hadrons to the SU(3) symmetry group led to the prediction, and eventual discovery, of the Ω^-, a powerful demonstration of successful feedback between theory and experiment.

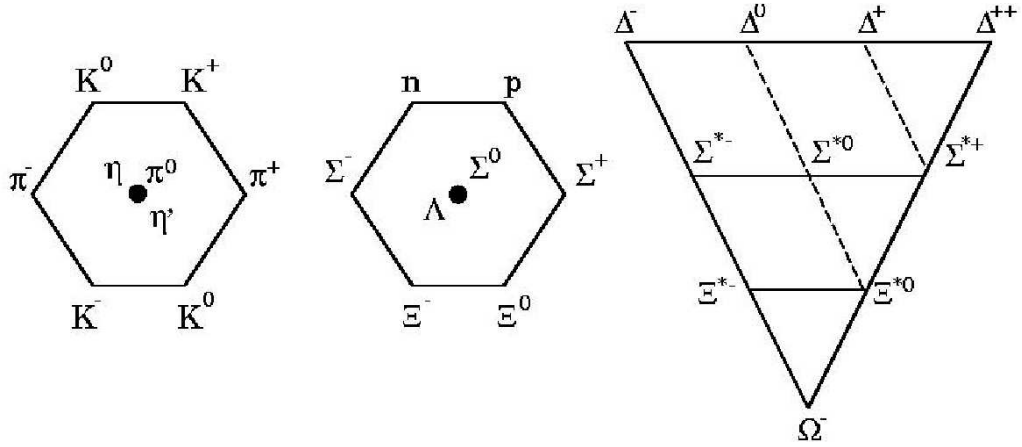

Figure 1.2: Hadron Multiplets of the "Eight-fold Way". From left; the meson nonet, spin $\frac{1}{2}$ baryon octet and spin $\frac{3}{2}$ baryon decuplet.

As a consequence of the SU(3) symmetry group representation of the hadrons, it became clear that they were not fundamental particles, but in fact composites made up of fundamental particles which were named 'quarks'. These were initially thought to come in three flavours, up, down, and strange, the three light quarks we know today, with the range of hadronic states explainable because of flavour symmetry between them.

This model of the quarks, based on symmetry, became increasingly challenged as new hadronic states were discovered, and the heavy quarks (charm, top and bottom), and associated quantum numbers, followed as experimental discovery and theoretical descriptions progressed.

However, the issue of the Δ^{++} state, composed of three up quarks of parallel spins, was at odds with the Pauli exclusion principle, which, as fermions, quarks must obey. To resolve this, a new quantum number, called colour, was introduced, which has three conditions; red, green and blue. Only colourless combinations of the quarks are allowed, either by combining the three colours in a baryon, or a coloured-anticoloured pair in a meson. This allows the Pauli exclusion principle to

hold for particles like the Δ^{++} without the experimental observation of colour.

To date, no experiment has ever observed free quarks, due to a property of QCD known as confinement. This arises from the fact that the force between two colour charges does not decrease with increased separation, which means that quarks cannot be removed from a hadron.

Another notable property of QCD is that of asymptotic freedom. At higher energies, the strong interaction weakens and becomes easier to calculate, due to the decrease of the QCD coupling constant with increasing energy.

At sufficiently high energies, perturbation theory is able to describe the sub-nucleon interactions governed by QCD in the same manner in which the photon and electron interactions are described in Quantum Electrodynamics (QED). However, at the lower energies of the quark-hadron interface, the running coupling constant of QCD approaches unity, and perturbative approaches can no longer accurately describe the underlying processes. QCD then enters the non-perturbative regime, where there are no rigorous solutions. This is a problem in studies of how quarks combine to form nucleons, and in understanding the excitation spectrum of the nucleon.

Attempts to predict the excited baryon spectrum numerically using the discrete space-time approaches of lattice QCD are beginning to yield spectra similar to those predicted by phenomenological models (these models will be discussed in the next subsection) [4], albeit with unphysical quark masses. Despite these recent advances, lattice QCD so far remains unable to fully describe the excited baryon spectrum.

1.1.2 Quark Models

Phenomenological quark models are employed in the field of hadronic physics as a result of the non-perturbative nature of QCD at low energies, and the current limitations of lattice QCD in accurately predicting the properties of hadronic states. These models describe the internal structure of the nucleon in terms of three constituent valence quarks, interacting through a potential [5, 6, 7].

Considering the flavour, spin, and orbital angular momentum of the quarks in SU(6)$\otimes$O(3) symmetric quark models enables the prediction of a series of resonant

states of the nucleon [5, 8], by considering the possible permutations of the allowed degrees of freedom in the model. Many of these resonances have been observed and studied in detail by various experiments [9].

Other models based on this approach also exist, and are able to predict their own spectra of nucleon resonances. One such model is the di-quark model, where two of the three quarks in the nucleon are bound. This binding restricts the degrees of freedom in this system compared to the symmetric quark model, and leads to the prediction of fewer states. The symmetric and di-quark models, and their differing angular momentum degrees of freedom, are represented in figure 1.3.

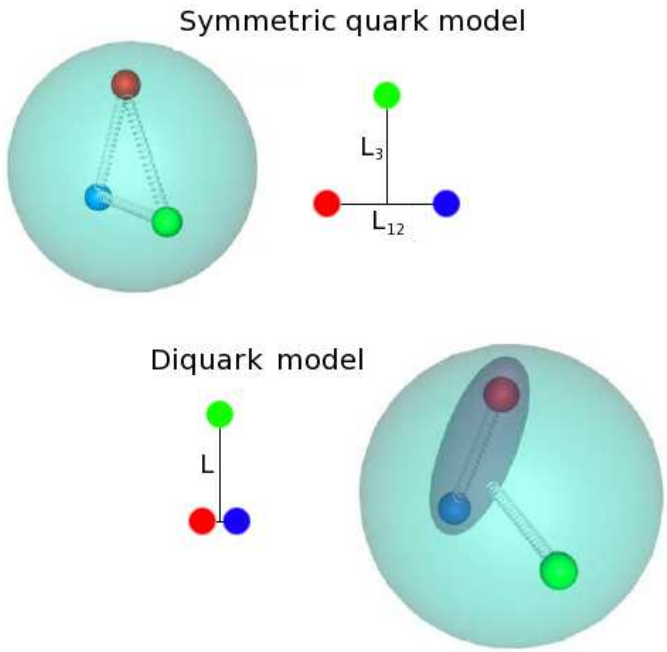

Figure 1.3: Schematic representation of the symmetric quark model (top) and the diquark model (bottom), showing the restriction on the possible orbital angular momentum states imposed by the bound pair of quarks in diquark model.

A problem arises when comparing the predictions of the symmetric and di-quark models with the current experimentally-observed baryon spectrum. Not only are the two models consistent with experimental data, but the symmetric models predict far more resonances than have currently been observed. This "missing" resonance problem is one of the burning questions in hadronic physics, and its resolution will have profound implications for our understanding of the nucleon and the behaviour of the quarks therein.

1.1.3 Resolving the Missing Resonance Problem

As well as identifying resonances, it is also important to determine their associated quantum numbers, and parameters such as masses and widths, allowing comparison with the predictions of the quark models and the potential to identify previously unobserved states from experimental data.

Table 1.1 shows the Particle Data Group (PDG) star ratings for the baryon resonances predicted by the QCD-improved quark shell model of Forsyth and Cutosky [8]. The star ratings indicate the level of confidence in the existence of the state based on experimental evidence and range from 1 star, for a state with poor evidence of existence, through to 4 stars for a state whose existence is certain. The missing states of the symmetric quark model have very few or no stars at all, indicating that experimental evidence for the state is minimal, or has not yet been found.

N^*	Status	SU(6)×O(3)	Parity	Δ^*	Status	SU(6)×O(3)
P_{11} (938)	****	$(56,0^+)$	+	P_{33} (1232)	****	$(56,0^+)$
S_{11} (1535)	****	$(70,1^-)$				
S_{11} (1650)	****	$(70,1^-)$		S_{31} (1620)	****	$(70,1^-)$
D_{13} (1520)	****	$(70,1^-)$	-	D_{33} (1700)	****	$(70,1^-)$
D_{13} (1700)	***	$(70,1^-)$				
D_{15} (1700)	****	$(70,1^-)$				
P_{11} (1520)	****	$(56,0^+)$		P_{31} (1875)	****	$(56,2^+)$
P_{11} (1710)	***	$(70,0^+)$	+	P_{31} (1835)		$(70,0^+)$
P_{11} (1880)		$(70,2^+)$				
P_{11} (1975)		$(20,1^+)$				
P_{13} (1720)	****	$(56,2^+)$		P_{33} (1600)	***	$(56,0^+)$
P_{13} (1870)	*	$(70,0^+)$		P_{33} (1920)	***	$(56,2^+)$
P_{13} (1910)		$(70,2^+)$	+	P_{33} (1985)		$(70,2^+)$
P_{13} (1950)		$(70,2^+)$				
P_{13} (2030)		$(20,1^+)$				
F_{15} (1680)	****	$(56,2^+)$		F_{35} (1905)	****	$(56,2^+)$
F_{15} (2000)	**	$(70,2^+)$	+	F_{35} (2000)	**	$(70,2^+)$
F_{15} (1995)		$(70,2^+)$				
F_{17} (1990)	**	$(70,2^+)$	+	F_{37} (1950)	****	$(56,2^+)$

Table 1.1: PDG star ratings for baryon resonances. The star ratings indicate the level of confidence in the existence of the state based on experimental evidence and range from 1 star, for a state with poor evidence of existence, through to 4 stars for a state whose existence is certain.

The fact the symmetric quark model predicts more states than the di-quark model, and that both models agree with the existing data, has led to two hypotheses explaining these missing resonances; either the absence of these states in the experimental data is because the additional states predicted by the symmetric quark model do not exist, or the experiments performed so far have been unable to definitively observe them.

The majority of the experimental data on baryon resonances has come from πN scattering experiments. To test the hypothesis of being unable to see the missing resonances with current experiments, i.e. the weak coupling of missing resonances to the πN channel, meson photoproduction has emerged as an important experimental technique within hadronic physics, with experiments being performed on several meson reaction channels [10, 11, 12].

The meson photoproduction cross section data shown in figure 1.1 also seems to show that different channels appear to be more sensitive to some resonances. Some studies have suggested several of the missing resonances may couple strongly to strangeness photoproduction channels, such as $K\Lambda$ and $K\Sigma$, due to their larger decay amplitudes in these channels [13].

The difficulty in resolving individual resonances from cross-section measurements alone is aided by the use of electromagnetic probes, whose reaction amplitudes are more straightforward to consider, than those of hadronic probes, as EM interactions are governed by QED. Additionally, polarisation information can be accessed with these probes, with the effects of polarisation on the reaction particles giving new insights into the properties of resonances, and more ways to find evidence of their existence [14].

1.1.4 The Λ and Σ^0 Hyperons

The hyperons, denoted Y, is the name given to the family of strange baryons, states consisting of three light quarks, where at least one of these quarks is a strange quark. The Λ and Σ^0 hyperons belong to the same baryon octet as defined in the eightfold way, with spin $\frac{1}{2}$ and zero charge. Both have a strangeness of -1, being composed of an up, down and strange quark.

The Λ has a mass of 1115.68 MeV/c^2 and a mean lifetime of 2.6×10^{-10} s, and the Σ a mass of 1192.64 MeV/c^2 and mean lifetime of 7.47×10^{-20} s. An important difference between the two particles is that the Λ has isospin of zero, and the Σ has isospin 1. This difference has major implications with regard to the excited states that can decay to $K^+\Lambda$ and $K^+\Sigma^0$ final states. The $K\Sigma^0$ final state can involve excitation to N* and Δ resonances, while $K\Lambda$ reactions can only involve isospin $\frac{1}{2}$ N* states, with no Δ states contributing.

As a result of their short lifetimes, neither of these hyperons will be detectable in the final state of a reaction by the experimental equipment used, and are instead reconstructed from their detected decay products. The two main decay modes of the Λ are

$$\Lambda \rightarrow p\pi^-$$

with a branching ratio of 63.9%, and

$$\Lambda \rightarrow n\pi^0$$

with branching ratio of 35.8%.

Because of its parity-violating weak decay [15], the Λ hyperon is said to be self-analysing. This means that the hyperon polarisation can be measured from the angular distribution of its decay products, without the need for a polarimeter device. The Σ^0 polarisation can also be measured, by exploiting the self-analysing property of its daughter Λ, which will retain some of the parent Σ^0 polarisation as it undergoes magnetic dipole decay to a Λ [16].

1.2 Polarisation Observables

Polarisation observables are a property associated with the polarised particles in a reaction. In the case of strangeness photoproduction, these are the incident photon, the target nucleon, and the recoiling hyperon. These observables are of interest because of their sensitivity to the presence of nucleon resonances, and their potential to facilitate model-independent analyses, by making a suitable combination of

measurements.

Consideration of the scattering amplitudes describing the states and channels contributing to the overall amplitude of kaon photoproduction [17] leads to their expression in terms of the four "CGLN amplitudes" defined by Chew, Goldberger, Low and Nambu [18]. The CGLN amplitudes can be expressed in terms of scattering angle and energy, but are more conveniently expressed in terms of transversity amplitudes, a set of four complex amplitudes completely describing the photoproduction process. By taking bilinear combinations of these four amplitudes, 16 polarisation observables can be defined [19].

The polarisation observables are grouped into single and double types, with the single polarisation observables arising from polarisation in one particle in a reaction, and the double observables accessible when pairs of particles in the interaction are polarised. The double observables have three sub-groupings, according to which pair of particles carry polarisation: Beam-Target, arising from combinations of polarisation modes of the photon beam (linear and circular) and the target (transverse and longitudinal); Beam-Recoil, arising from combinations of beam polarisation modes and the recoil polarisation (x' and z'); and Target-Recoil, from the combinations of the target and recoil polarisation modes. The 16 single and double polarisation observables associated with strangeness photoproduction, their representation in terms of transversity amplitudes $b_1, \ldots, b_4$, and the polarised experiments required to access them, are shown in table 1.2.

As a result of their definition in terms of the four transversity amplitudes, the full set of observables contain redundant information and can be related by the following

Symbol	Transversity representation	Experiment Required	Type
σ_0	$\|b_1\|^2 + \|b_2\|^2 + \|b_3\|^2 + \|b_4\|^2$	- / - / -	Single
Σ	$\|b_1\|^2 + \|b_2\|^2 - \|b_3\|^2 - \|b_4\|^2$	P_{lin} / - / -	
T	$\|b_1\|^2 - \|b_2\|^2 - \|b_3\|^2 + \|b_4\|^2$	- / P_y / -	
P	$\|b_1\|^2 - \|b_2\|^2 + \|b_3\|^2 - \|b_4\|^2$	- / - / y	
G	$2Im(b_1 b_3^* + b_2 b_4^*)$	P_{lin} / P_z / -	Beam-Target
H	$-2Re(b_1 b_3^* - b_2 b_4^*)$	P_{lin} / P_x / -	
E	$-2Re(b_1 b_3^* + b_2 b_4^*)$	P_{circ} / P_z / -	
F	$2Im(b_1 b_3^* - b_2 b_4^*)$	P_{circ} / P_x / -	
O_x	$-2Re(b_1 b_4^* - b_2 b_3^*)$	P_{lin} / - / x'	Beam-Recoil
O_z	$-2Im(b_1 b_4^* + b_2 b_3^*)$	P_{lin} / - / z'	
C_x	$2Im(b_1 b_4^* - b_2 b_3^*)$	P_{circ} / - / x'	
C_z	$-2Re(b_1 b_4^* + b_2 b_3^*)$	P_{circ} / - / z'	
T_x	$2Re(b_1 b_2^* - b_3 b_4^*)$	- / x / x'	Target-Recoil
T_z	$2Im(b_1 b_2^* - b_3 b_4^*)$	- / x / z'	
L_x	$2Im(b_1 b_2^* + b_3 b_4^*)$	- / z / x'	
L_z	$2Re(b_1 b_2^* + b_3 b_4^*)$	- / z / z'	

Table 1.2: Single and double polarisation observables associated with kaon photoproduction. N.B. the Σ polarisation observable is a separate entity to the Σ hyperon, and care should be taken to avoid confusion. The transversity representations of the observables and the polarised experiments required to measure them are also shown in the format (beam/target/recoil). The work in this thesis is primarily concerned with measuring the G observable, requiring a linearly polarised photon beam and a longitudinally polarised target. Information from [19].

set of expressions [17];

$$E^2 + F^2 + G^2 + H^2 = 1 + P^2 - \Sigma^2 - T^2 \tag{1.1}$$

$$FG - EH = P - \Sigma T \tag{1.2}$$

$$T_{x'}^2 + T_{z'}^2 + L_{x'}^2 + L_{z'}^2 = 1 + \Sigma^2 - P^2 - T^2 \tag{1.3}$$

$$T_{x'} L_{z'} - T_{z'} L_{x'} = \Sigma - PT \tag{1.4}$$

$$C_{x'}^2 + C_{z'}^2 + O_{x'}^2 + O_{z'}^2 = 1 + T^2 - P^2 - \Sigma^2 \tag{1.5}$$

$$C_{z'} O_{x'} - C_{x'} O_{z'} = T - P\Sigma \tag{1.6}$$

This redundancy of information implies that the transversity amplitudes can be determined by measuring a carefully chosen subset of the observables. Detailed investigations have demonstrated that measurement of the cross-section, σ_0, and single polarisation observables Σ, T and P, as well as four appropriately chosen

double polarisation observables (of which there are several examples) can determine the reaction amplitudes without ambiguities [19, 20], however, the available data and associated uncertainties do not provide sufficient constraint to eliminate these ambiguities and more than eight measurements will be needed [14].

The polarisation observables each contribute to the overall differential cross-section [17], with the various observables scaled by the appropriate degree of polarisation. To access the G observable, a polarised beam and target are required, and the cross-section can be expressed by

$$\begin{aligned}\frac{d\sigma}{d\Omega} = \ & \sigma_0\{1 - P_{lin}\Sigma cos2\phi \\ & + P_x(-P_{lin}Hsin2\phi - P_\lambda F) \\ & - P_y(-T + P_{lin}Pcos2\phi) \\ & - P_z(-P_{lin}Gsin2\phi + P_\lambda E)\}\end{aligned} \tag{1.7}$$

Where $\frac{d\sigma}{d\Omega}$ is the differential cross section, σ_0 is the unpolarised cross section, P_{lin} and P_λ are the degree of linear and circular polarisation of the photon beam, P_x, P_y, and P_z represent the x,y and z components of the degree of polarisation of the target, and ϕ is the kaon azimuthal angle. For a longitudinally polarised target, $P_x = P_y = 0$, and for the linearly polarised beam, $P_\lambda = 0$, so in this case equation 1.7 simplifies to

$$\frac{d\sigma}{d\Omega} = \sigma_0\{1 - P_{lin}\Sigma cos2\phi + P_z(P_{lin}Gsin2\phi)\} \tag{1.8}$$

Theoretical predictions of the polarisation observables vary depending upon the set of resonances included in the quark model used for the prediction. This can enable the presence of a resonance to be inferred by comparing experimental data with theoretical predictions of the observables for various models that include differing sets of resonances. This is demonstrated in figure 1.4, which shows several such predictions of the Σ observable for $K^+\Lambda$ photoproduction, some of which include a $D_{13}(1960)$ resonance.

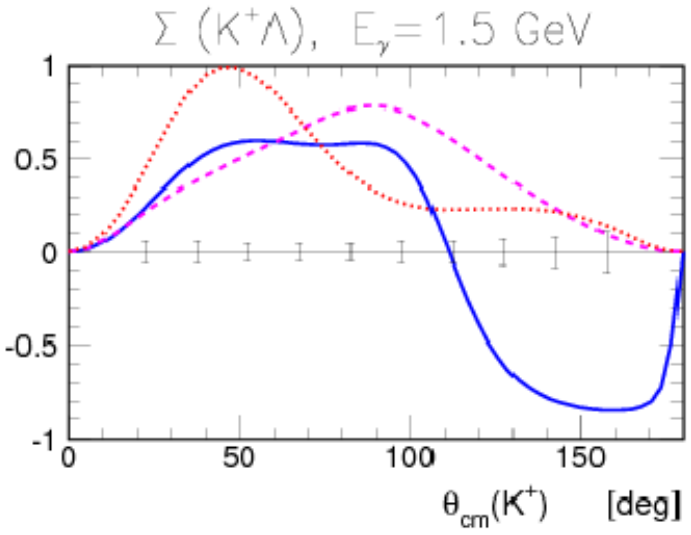

Figure 1.4: Model predictions of the beam polarisation observable, Σ, at photon energy of 1.5 GeV. The solid blue line represents the SAID partial wave analysis solution, the dotted red line a model of B. Saghai [21], and the pink dashed curve corresponds to the Mart-Bennhold model, which includes a $D_{13}(1960)$ resonance [22]. Image from [23].

1.3 The N* Physics Program at Jefferson Lab

The N* program at Jefferson Lab aims to isolate resonant states of the nucleon in order to measure the quantum numbers and properties of these states, including energy, lifetime and spin. This program encompasses a variety of experiments and analyses [23, 24, 25, 26, 27, 28] using electromagnetic probes at GeV energy scales with the CLAS detector [29], a large acceptance detector system which possesses sufficient resolution to probe resonances with both photon and electron beams.

The photon beams can be polarised, both circularly and linearly, with the coherent bremsstrahlung facility at the lab enabling the production of linearly polarised photon beams with a high degree of polarisation. Combined with the recoil polarisation accessible as a result of the self-analysing nature of the hyperon, and the frozen spin polarised targets developed at the lab [27, 30], the full set of 16 polarisation observables can be measured for strangeness photoproduction [23].

By performing a so-called "complete experiment", where a sufficient number of observables have been measured to unambiguously determine the reaction amplitudes for kaon photoproduction, a near model-independent partial wave analysis

(PWA) can be carried out, a fitting technique which parameterises these amplitudes in terms of contributing resonances.

The g9/FROST experiments utilised a polarised photon beam and polarised target to measure the beam-target double polarisation observables, and beam-recoil observables via the strangeness channels, completing the database of polarisation observables measured at Jefferson Lab for strangeness photoproduction on the proton.

1.4 Summary

Studies of the excited baryon spectrum are of great importance for our understanding of the internal structure of the nucleon in terms of quark interactions. The non-perturbative nature of QCD at the energy scale where nuclear and particle physics meet makes it difficult to understand how quarks combine to form nucleons, and to predict the possible excited states.

Although phenomenological quark models have proven successful in describing the current experimental data on resonances, a large number of predicted states remain unobserved, with different quark models predicting different excitation spectra of the nucleon.

Some quark model calculations have suggested that some of the unobserved states could be easier to observe in $K^+\Lambda$ and $K^+\Sigma^0$ final states, and measurements of the polarisation observables associated with these, and other meson photoproduction channels, is underway. The data from these experiments offers the prospect of measuring the baryon spectrum independently of the quark models, and identifying missing resonances, should they exist.

The work presented in this thesis makes the first measurements at Jefferson Lab of the beam polarisation observable Σ and the beam-target double polarisation observable G for the $\gamma p \to K^+\Lambda$ and $\gamma p \to K^+\Sigma^0$ reactions on a frozen spin polarised target. These results, and those from complimentary analyses on this data of other observables and on other reaction channels, should provide new insight into the meson photoproduction process and the excitation spectrum of the nucleon.

Before progressing with a description of the experimental facility and the analysis performed, it is first necessary to consider current state of world data for polarisation observables associated with strangeness photoproduction and the theoretical models used to predict the baryon spectrum.

Chapter 2

Previous Data and Model Predictions

This chapter will present an overview of the currently-available data on the polarisation observables for strangeness photoproduction, with particular focus on the experiments performed at Jefferson Lab as part of the N* physics program [28]. Data from selected other facilities will also be shown, for comparison with the Jefferson Lab data.

Additionally, some of the phenomenological models used to predict the baryon spectrum will be discussed, examining their relative merits and limitations in identifying resonant states from experimental data. Theoretical predictions of the polarisation observables of interest in the analysis made by phenomenologically-inspired models will also be shown.

2.1 Previous Measurements

Kaon photoproduction has been studied for over fifty years, with several early experiments contributing to a small dataset of mainly cross-section measurements [31, 32, 33]. By the early 1990s, new data was obtained for the $\gamma p \rightarrow K^+\Lambda$ and $\gamma p \rightarrow K^+\Sigma^0$ reactions using the SAPHIR detector and ELSA, the electron stretcher ring in Bonn [34]. The SAPHIR data was taken at photon energies ranging from 0.9 to 2.0 GeV, and consists of $\sim$7600 $K^+\Lambda$ and $\sim$5900 $K^+\Sigma^0$ events.

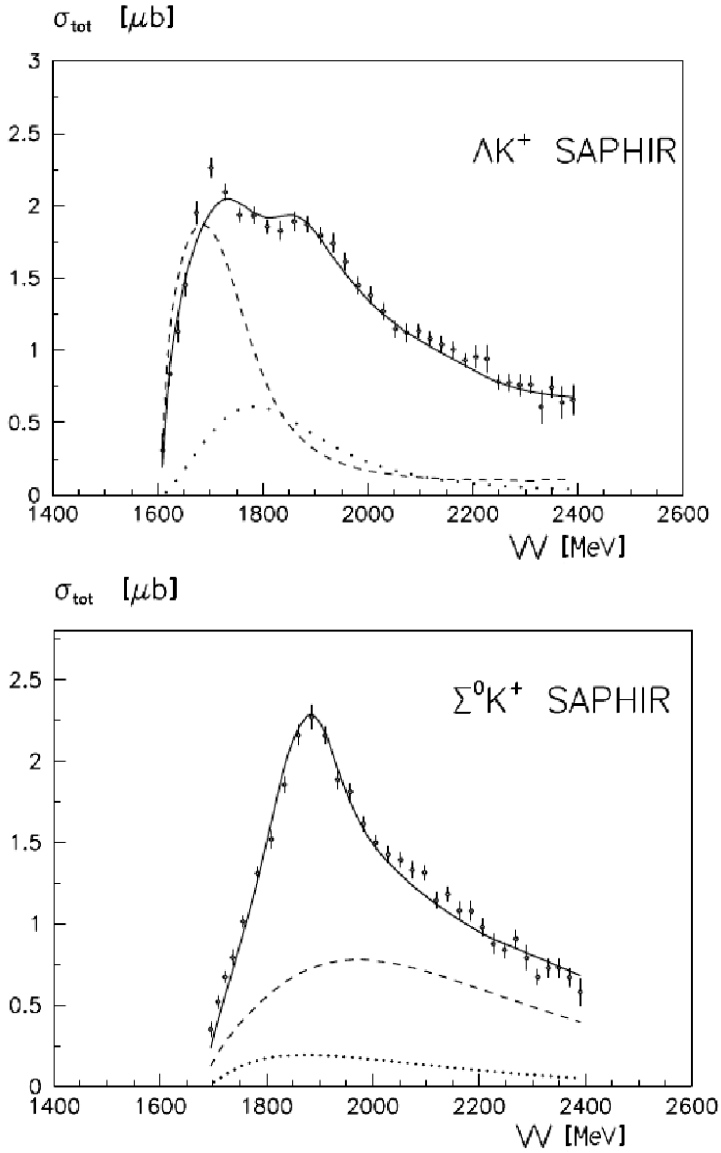

Figure 2.1: $K\Lambda$ and $K\Sigma$ cross section measurements from SAPHIR as a function of centre-of-mass energy (W). The solid line indicates the results of a fit to this data by the partial wave analysis of Sarantsev et. al. [35]. The dashed line shows the contribution from the S_{11} amplitude and the dotted lines show the contribution from the $P_{13}(1720)$

The SAPHIR cross section results for the $K^+\Lambda$ and $K^+\Sigma^0$ channels are shown in figure 2.1. The $K^+\Lambda$ results display a steep rise in the cross section from threshold to an initial peak at centre-of-mass energy (W) $\approx$ 1.7 GeV, with further structure seen at W $\approx$ 1.9 GeV ($E_\gamma \approx$ 1.1 and 1.5 GeV, respectively). The first peak corresponds to three resonances known to decay strongly to $K^+\Lambda$; $S_{11}(1650)$, $P_{11}(1710)$ and $P_{13}(1720)$, with theoretical studies suggesting a possible missing resonance to explain the structure at higher energy.

The $K^+\Sigma^0$ data exhibits a shallower climb to a peak at W $\approx$ 1.9 GeV, thought to arise from the $S_{31}(1900)$ and $P_{31}(1910)$ states which are expected to contribute to $K^+\Sigma^0$ photoproduction.

Following the SAPHIR work, higher-statistics measurements of the cross sections for both the $K^+\Lambda$ and $K^+\Sigma$ reactions were made using CLAS [36, 37]. These measurements covered centre-of-mass energies in the range 1.6 to 2.53 GeV and are shown in figures 2.2 and 2.3, alongside the SAPHIR data and older Bonn data from the ABBHHM collaboration [38].

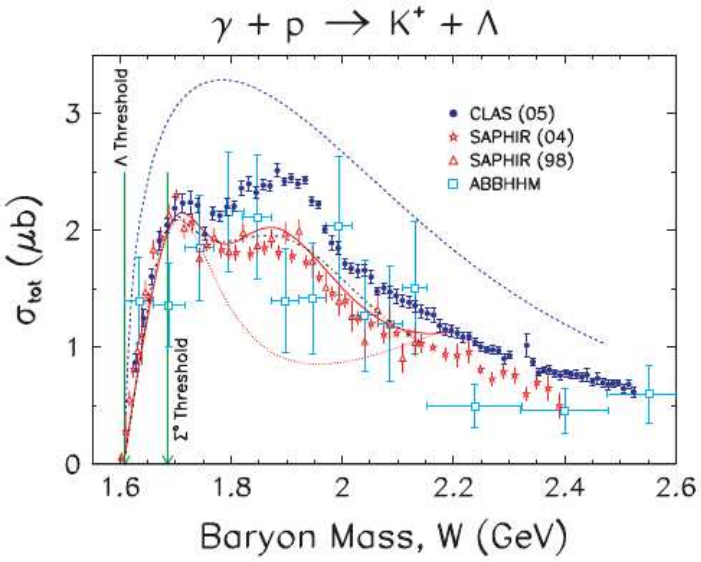

Figure 2.2: $K\Lambda$ Cross section measurements from CLAS (blue circles) shown alongside the data from two SAPHIR analyses (red stars and triangles), and older ABBHHM data (blue squares). Several theoretical models are also shown; a Regge model (dashed blue line), Kaon-MAID (solid red) with no $D_{13}(1985)$ resonance, and a model developed by Saghai (dot-dashed black). Image from [37].

The CLAS data reproduces the overall structure of the SAPHIR results, although the $K^+\Lambda$ cross sections are somewhat larger. Despite this, the same peaks are

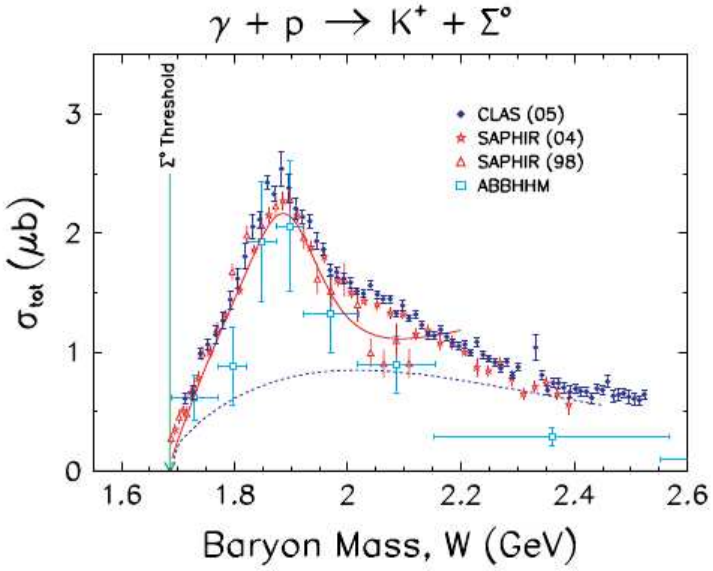

Figure 2.3: $K\Sigma$ Cross section measurements from CLAS (blue circles) shown alongside the data from two SAPHIR analyses (red stars and triangles), and older ABBHHM data (blue squares). Several theoretical models are also shown; A Regge model (dashed blue line), and Kaon-MAID (solid red). Image from [37].

seen for $K^+\Lambda$ at W $\approx$ 1.7 and 1.9 GeV, the lower energy peak consistent with the $P_{11}(1710)$ and $P_{13}(1720)$ states, and the higher peak due to several contributing resonances. For $K^+\Sigma$, the CLAS data exhibits a slight shoulder at W $\approx$ 2 to 2.1 GeV, in addition to the previously observed peak. This peak is thought to arise from several Δ resonances which couple to $K^+\Sigma$.

2.1.1 Polarisation Observables at CLAS

As discussed in chapter 1, cross-section measurements alone are a fairly blunt probe of the resonance spectrum, where even high quality, high statistics data are insufficient to unambiguously resolve every contributing state. The previous chapter also outlined how the sensitivity of polarisation observables to resonances has been identified for experimental study, owing to their derivation from the reaction amplitudes which fully describe photoproduction reactions, and how measuring an appropriate subset of the 16 observables is sufficient to determine these amplitudes without ambiguity.

One of the goals of the N* physics program at Jefferson Lab is to facilitate a model independent analysis by measuring more than the minimum required num-

ber of observables required to determine the reaction amplitudes unambiguously. The data from the various experiments comprising the program can be checked for consistency via the algebraic correlations between the observables (equations 1.1 to 1.6).

For strangeness photoproduction, the database for polarisation observables remained quite sparse until relatively recently, with no data at all for many observables [23]. Figure 2.4 shows this state of the data for the single polarisation observables on $K^+\Lambda$, and an indication of the kinematic range covered by the experiment on which the analysis in this thesis is performed.

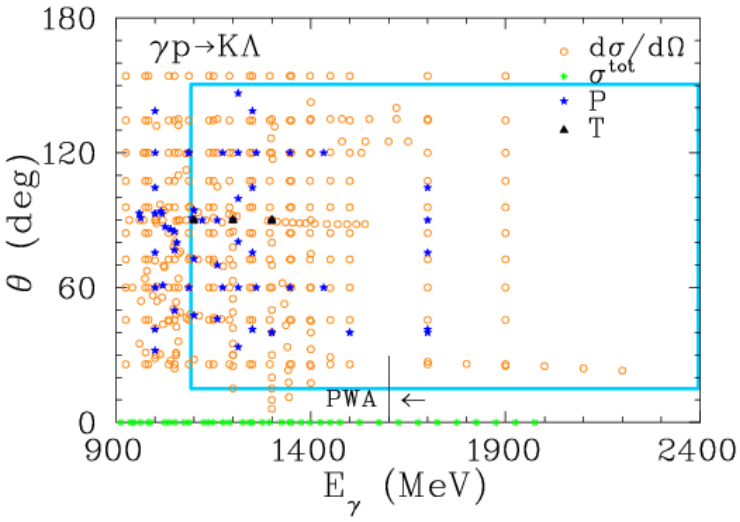

Figure 2.4: Database of single polarisation observables for $\gamma p \rightarrow K^+\Lambda$, with the kinematic range covered by the FROST experiments shown within the light blue box.

In addition to the cross section measurements shown in the previous subsection, the same data was used to measure P, C_x and C_z [16]. The C_x and C_z measurements for $K^+\Lambda$ are shown in figure 2.5.

Within the last decade, several facilities have released new results for strangeness photoproduction, and the gaps in the data for polarisation observables on these channels are being gradually filled in. The next subsection will present selected results from these other facilities, with the remainder of this subsection outlining progress at Jefferson Lab.

To date, Jefferson Lab's N* program has made extensive measurements of single

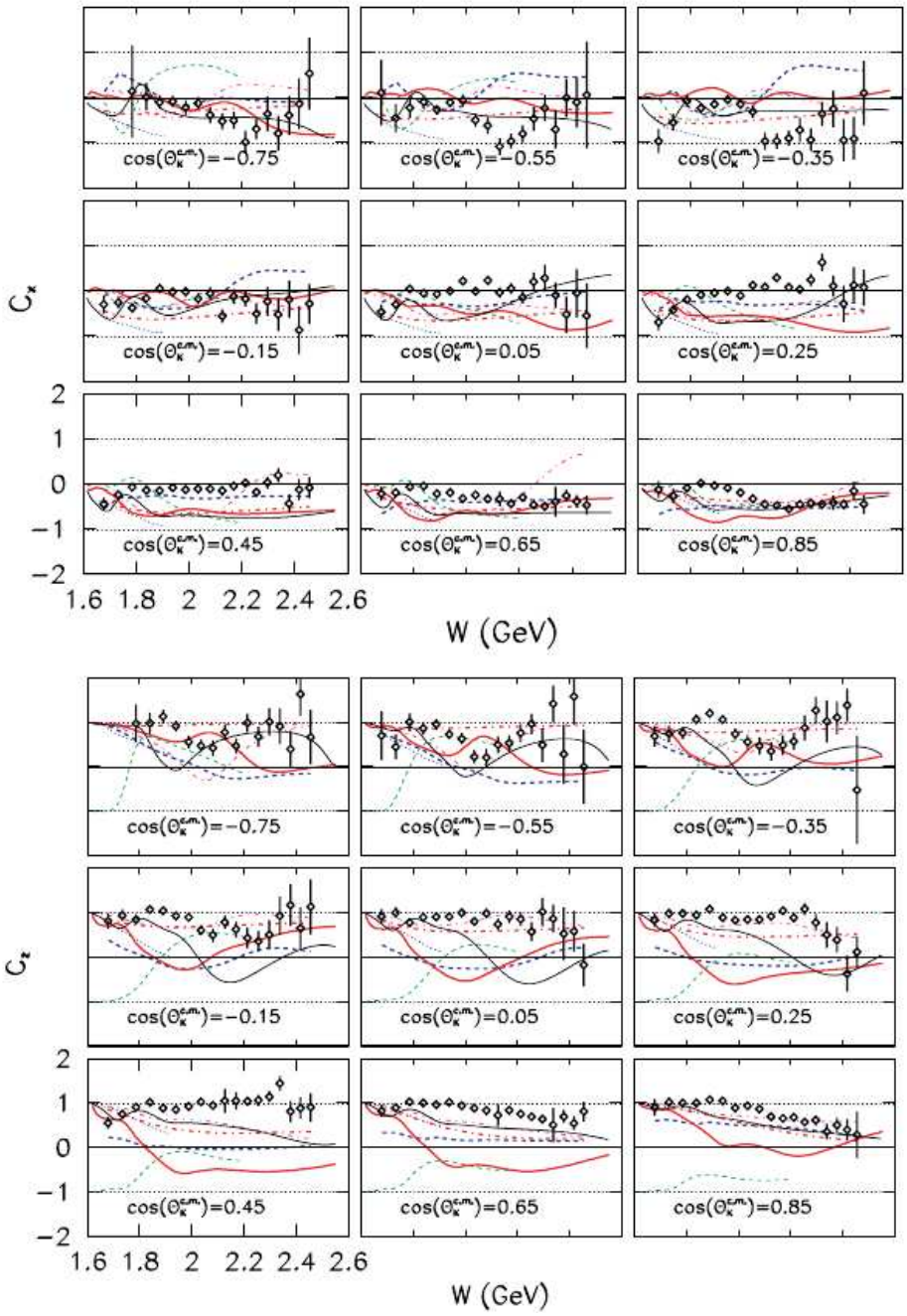

Figure 2.5: C_x and C_z beam-recoil double polarisation observables measured at CLAS for $\gamma p \rightarrow K^+\Lambda$ [16]. Several model predictions are also shown, including Kaon-MAID as a dashed green line, Regge-plus-resonance as a solid black line, and GENT model as a dot-dashed magenta line.

and beam-recoil double polarisation observables for the strangeness photoproduction channels [23, 28]. Analysis from the recent g8b experiment greatly enhanced the database for both $K^+\Lambda$ and $K^+\Sigma^0$ photoproduction, producing measurements of the Σ, P and T observables, alongside first measurements of the O_x and O_z beam-

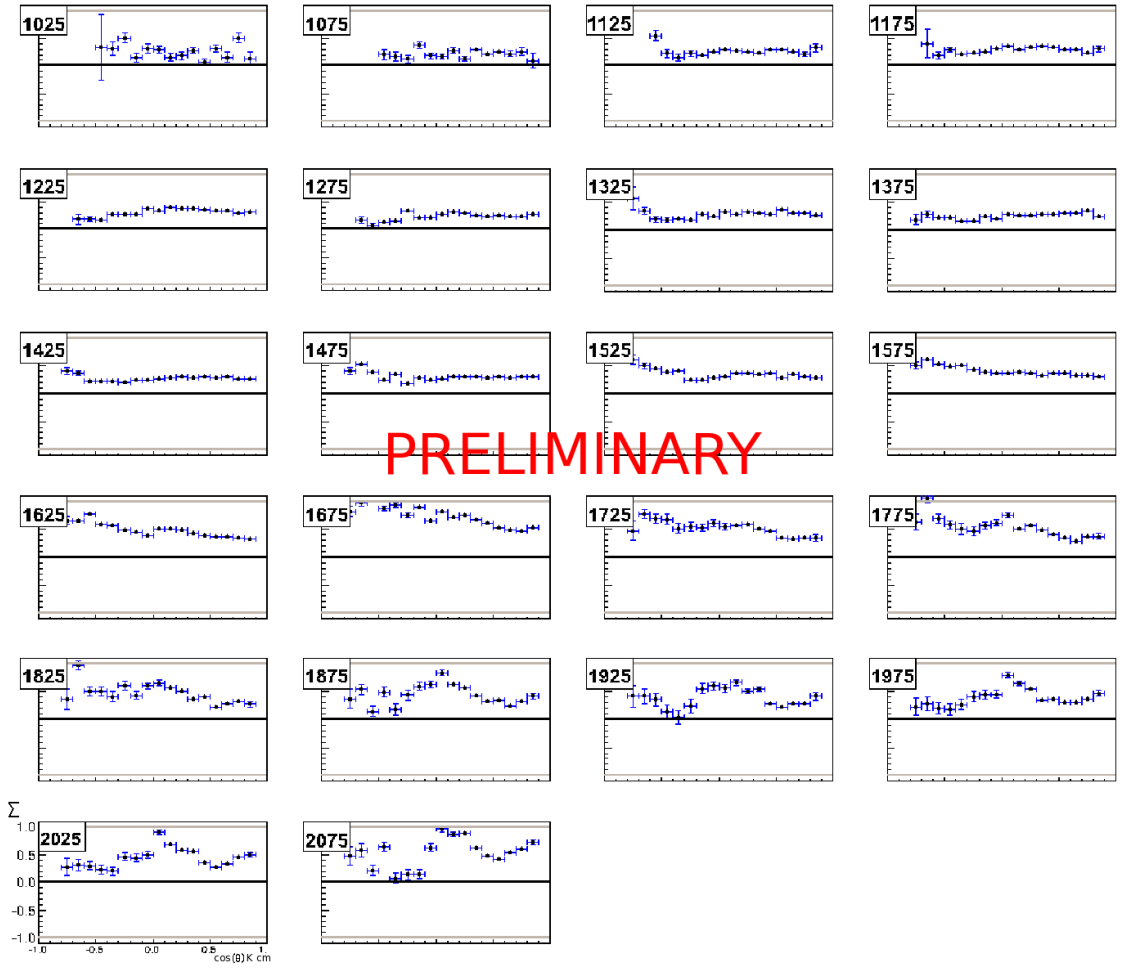

Figure 2.6: Preliminary measurements of the beam polarisation observable (Σ) for the reaction $\gamma p \rightarrow K^+\Lambda$ as a function of $cos\theta^{K+}_{cm}$ from the g8b experiment at CLAS [39] for a series of photon energy bins ranging from $E_\gamma = 1.025$ to 2.075 GeV. These energies are displayed in MeV in the boxes at the top left of each plot.

recoil double observables. The preliminary results of the g8b analysis are reported in the PhD thesis of C. Paterson [39], and will be published in the near future.

Figure 2.6 shows the g8b measurements of the beam polarisation observable, Σ, for a series of photon energy bins for $K^+\Lambda$. It can be seen that the Σ observable is positive over the full kinematic range for both these reactions, remaining largely flat for $K^+\Lambda$ up to photon energies around 1.375 GeV, where it begins to display a peak at backwards angles. A second structure at $\cos\,\theta^{K+}_{cm} = 0$ emerges at photon energy around 1.775 GeV. Preliminary results from g8b for the target asymmetry are shown in figure 2.7.

Other work at Jefferson Lab has looked to neutron channels to widen the search

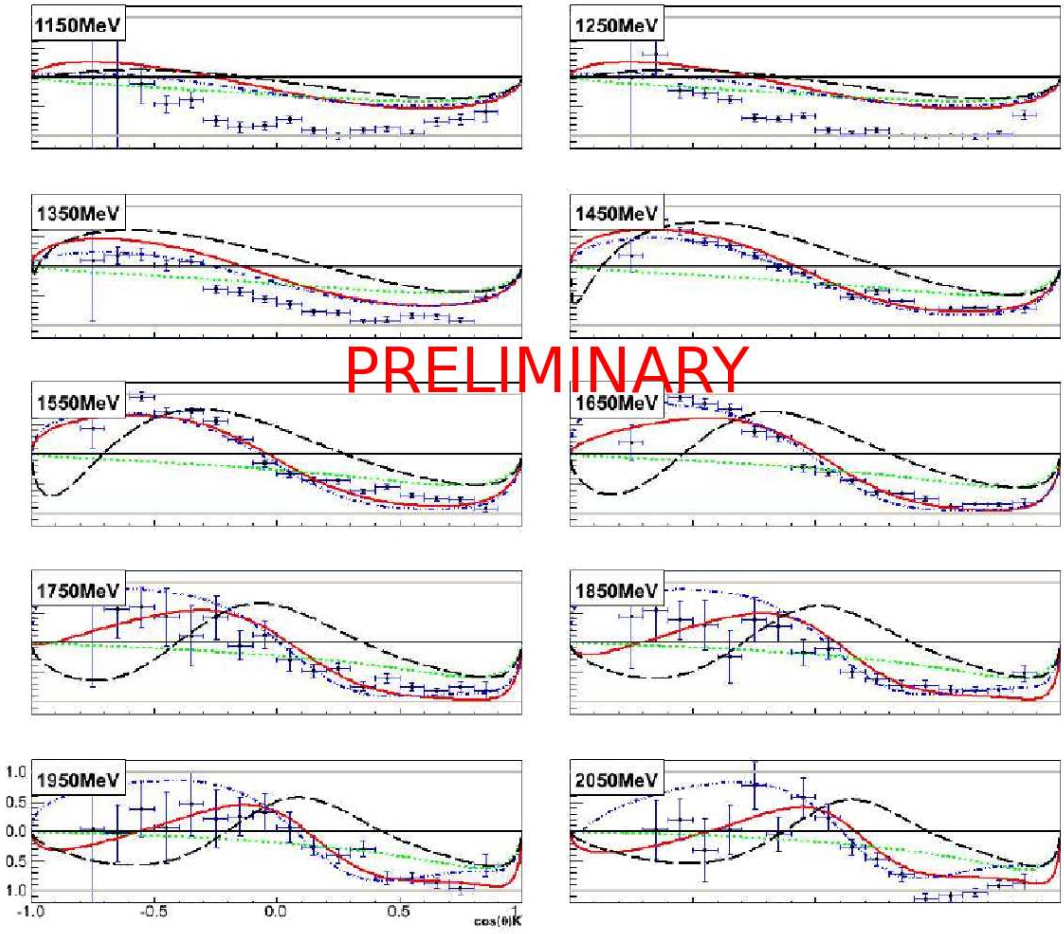

Figure 2.7: Preliminary measurements of the target asymmetry for the reaction $\gamma p \rightarrow K^+\Lambda$ as a function of $cos\theta^{K+}_{cm}$ from the g8b experiment at CLAS [39] for photon energy bins ranging from 1.150 to 2.050 GeV. Data is compared with model curves for the Gent Regge-plus-resonance model, with the Regge background (dotted green line), core resonances (dot-dashed blue line), $D_{13}(1900)$ (solid red line) and $P_{11}(1900)$ (dashed black line).

for resonances. In the absence of a free neutron target, deuterium has been used in the g13 experiment [40], and to show that the bound neutron is suitable for $\gamma n \rightarrow KY$ analyses, cross checking with free proton experiments, such as g8b, had to be performed on the bound proton. The preliminary results of the g13 experiment are presented in the PhD thesis of J. Johnstone [41]. By showing the bound proton data agrees with that for the free proton, ongoing neutron analyses [42] can be validated.

Figure 2.8 shows the comparison between CLAS measurements of Σ for the free and quasi-free proton on the $K^+\Lambda$ channel. These results are consistent over the entire kinematic range where the data overlaps, with a slight extension in photon energy range over the g8b data.

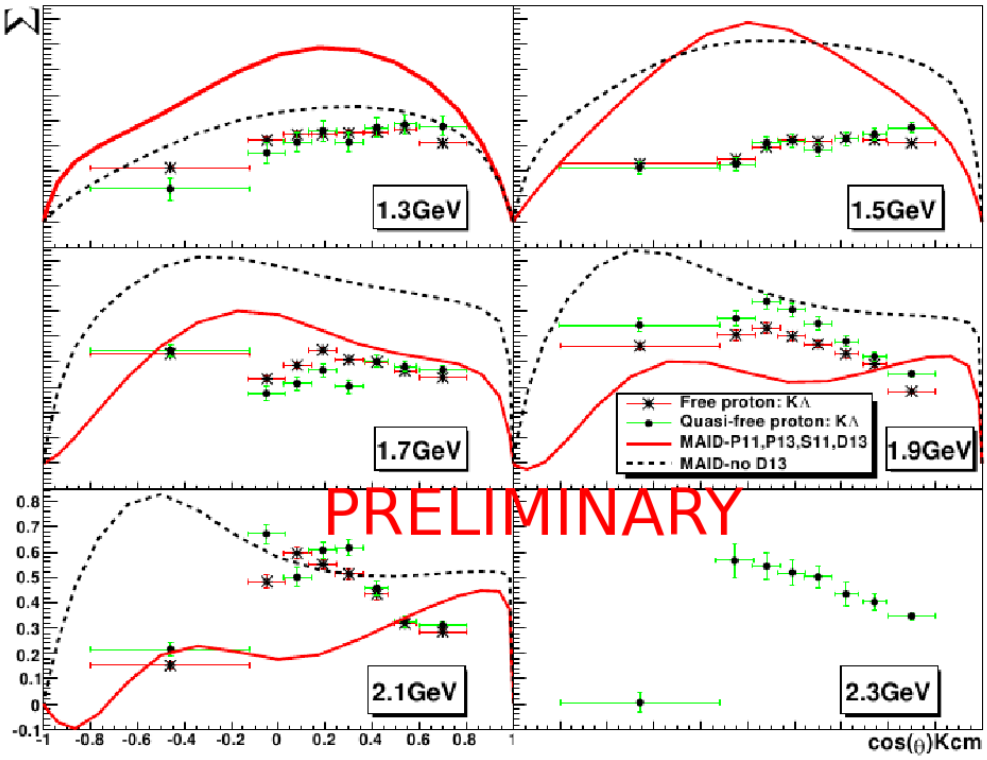

Figure 2.8: Preliminary measurements of the beam polarisation observable (Σ) for the reaction $\gamma p \rightarrow K^+\Lambda$ as a function of $cos\theta^{K+}_{cm}$ from the g13 experiment at CLAS [41] for a series of photon energy bins ranging from E_γ = 1.25 to 2.25 GeV. Quasi-free proton data (green error bars) are compared with the free proton data from the g8b experiment (red error bars), and model curves from the Kaon-MAID model with (red line) and without (dashed black line) a D_{13} resonance.

This principle of validating results from quasi-free protons on free proton data

is also applied to the analysis in this thesis, which uses molecular targets containing bound nucleons as well as hydrogen (protons). Similar comparisons will need to be performed on data from the molecular targets in this experiment to show that they can be used to measure polarisation observables on $\gamma p \rightarrow KY$ reactions. This will be discussed further in chapter 6.

2.1.2 Polarisation Observables at Other Facilities

In addition to CLAS, experimental programmes in strangeness photoproduction have also been performed by the GRAAL collaboration in Grenoble, France, and the LEPS collaboration at the Spring8 facility in Japan.

The LEPS data were taken using a photon beam produced by a backward-Compton scattering facility, and a detector system comprising of a silicon strip vertex detector and drift chambers to measure the momentum of the K^+ meson, with start and stop signals provided by appropriately positioned plastic scintillators. LEPS made the first photon asymmetry measurements on $K^+\Lambda$ and $K^+\Sigma$ photoproduction, at photon energies ranging from 1.5 to 2.4 GeV, for forward angular bins spanning $cos(\theta^{K^+}_{cm}) = 0.6$ to 1.0 [43].

The results of this experiment are shown in figure 2.9, and show the Σ observable to be positive, gradually increasing in photon energy. The results are also compared with model predictions of Kaon-MAID [44] and Janssen et. al. [45], which include a $D_{13}(1895)$ resonance, with the differences between the models and the data thought to arise from the lack of available data and large freedoms in the models.

At GRAAL, the 4π LAGRANγE detector was used in conjunction with a tagged polarised photon beam produced by Compton-scattering laser photons off circularly polarised electrons in the storage ring at the European Synchrotron Radiation Facility (ESRF) [46]. This data were taken at photon energies from threshold up to 1.5 GeV, and measured both the Σ (beam polarisation) and P (recoil) observables [47]. The T (target asymmetry), O_x and O_z observables were also measured [48]. The Σ results showed good agreement with the overlapping regions of the LEPS data, and the P results also agreeing with CLAS and SAPHIR data. A selection of these results are shown in figures 2.10 and 2.11. The comparison of Σ results between

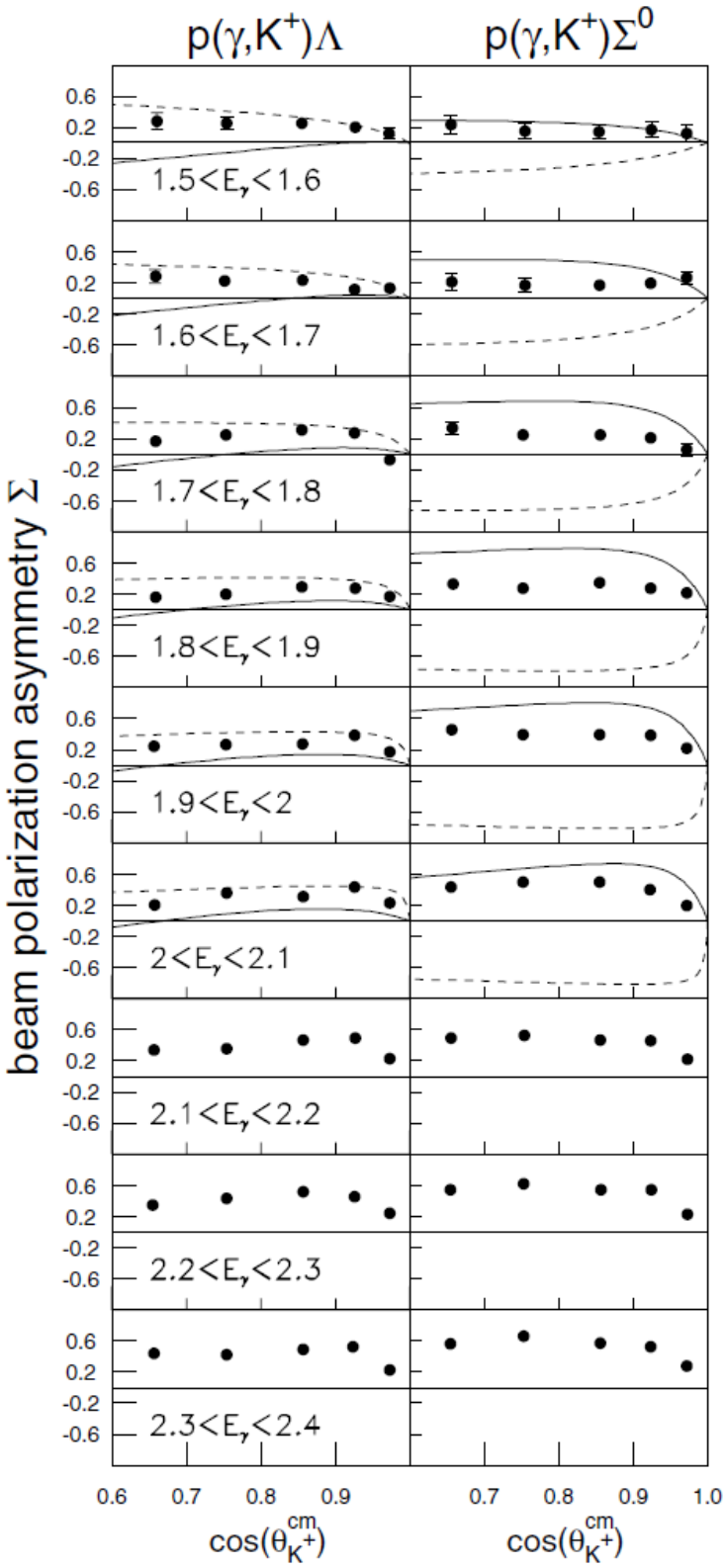

Figure 2.9: Photon Asymmetry Measurements from LEPS for $K^+\Lambda$ (left column) and $K^+\Sigma^0$ (right column) as a function of $cos\theta^{K+}_{cm}$ for a series of photon energy bins. Model predictions from Kaon-Maid (dashed lines) and by Janssen et. al. (solid lines) are shown. Image from [43].

GRAAL and the preliminary g8b data in figure 2.10 highlights the significant contribution the N* program at Jefferson lab will make to the world data on polarisation observables.

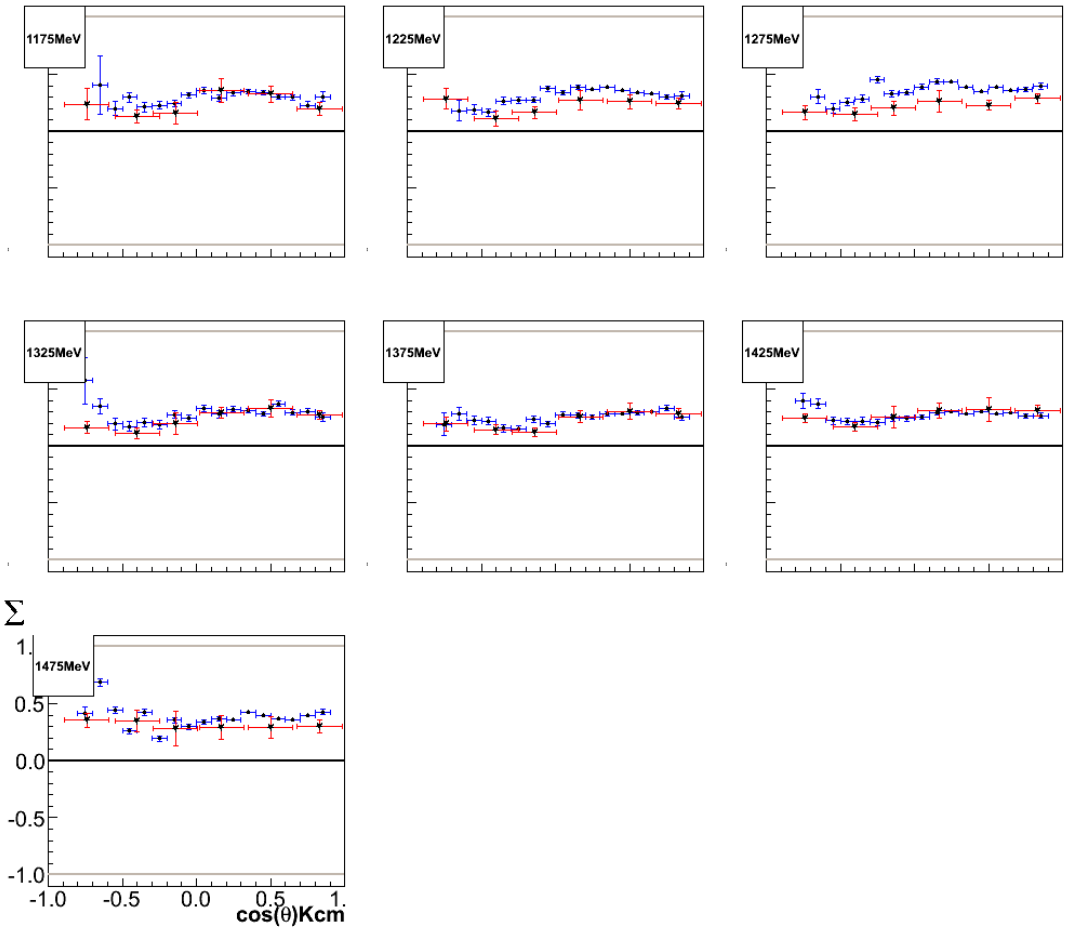

Figure 2.10: Photon Asymmetry Measurements from GRAAL for the reaction $\gamma p \rightarrow K^{+}\Lambda$ (red error bars), compared with preliminary data from the CLAS g8b experiment (blue error bars) in the photon energy range 1.175 to 1.475 GeV.

2.1.3 Beam-Target Double Polarisation Observables

Until now, polarisation observables for strangeness photoproduction have utilised polarised photon beams and the self-analysing nature of the hyperon to access the single polarisation observables and the beam-recoil double observables. Although some data is available for pion photoproduction going back to the 1970s [49], no previous measurements of beam-target observables have been made for the strangeness channels.

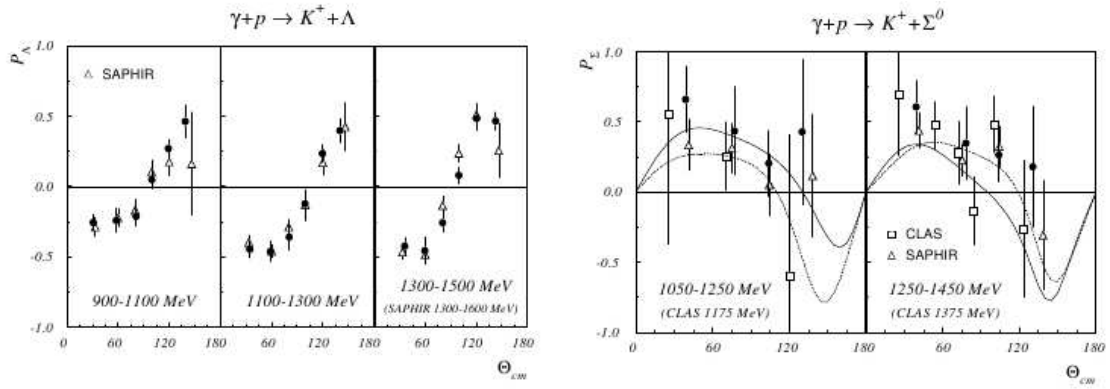

Figure 2.11: Recoil Polarisation Measurements from GRAAL for $K^+\Lambda$ and $K^+\Sigma^0$ (closed circles). Comparison is made with SAPHIR data (open triangles) for both $K^+\Lambda$ and $K^+\Sigma^0$ and with CLAS (open squares) for $K^+\Sigma^0$.

With the database for single and beam-recoil double observables beginning to fill in, a new generation of experiments are being performed using polarised targets in order to perform complete and over-determined measurements of the polarisation observables for meson photoproduction.

Several facilities have proposed and developed polarised targets for meson photoproduction, including MAMI in Mainz, Germany, and CLAS [30, 50, 51].

This thesis will provide first measurements of the Σ and G observables for the $K^+\Lambda$ and $K^+\Sigma^0$ reactions using the FROST polarised target. Other analyses on this data [52] are in progress, and preliminary results for E, one of the beam-recoil observables are shown in figure 2.12.

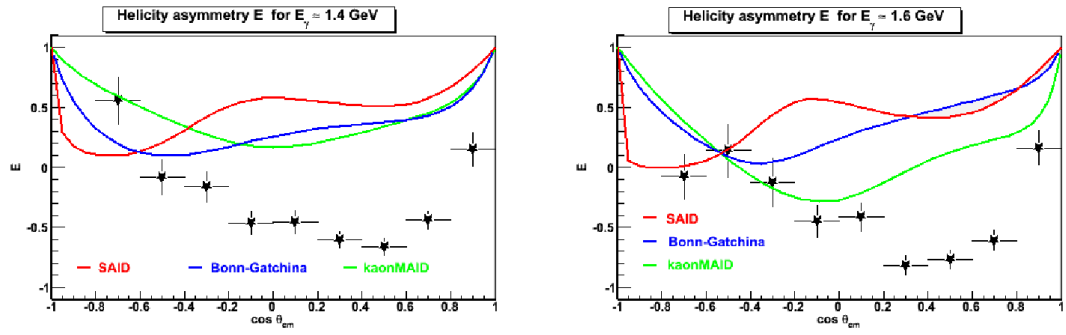

Figure 2.12: Preliminary measurements of the E double polarisation observable for the reaction $\gamma p \to K^+\Lambda$ as a function of $cos\theta^{K+}_{cm}$ from the g9a (FROST) experiment at CLAS [52] for two photon energy bins; $E_\gamma = 1.4$ and 1.6 GeV. Data are compared with the SAID partial wave analysis (red curve), Bonn-Gatchina model (blue curve) and Kaon-MAID (green curve) predictions.

With no previous data to compare to, the G observable results presented in this thesis will look to the predictions of theoretical models, which are discussed in the next section.

2.2 Theoretical Models

Theoretical descriptions of photoproduction reactions are a vital tool in interpreting experimental data in terms of the identification of resonances. Despite several decades of study, the underlying reaction mechanism in strangeness production is not well understood, with the presence of the strange quark potentially allowing the excitation of resonances not seen in pion photoproduction [23].

Several phenomenological models have emerged in the energy regime of non-perturbative QCD, including tree-level isobar, coupled channels, and Regge models. The remainder of this chapter will introduce these models, and discuss how they attempt to describe the nucleon resonance spectrum, as well as highlighting the successes and problems they encounter. Predictions of the G observable for the reactions of interest will also be shown, which will be compared with the final results in chapter 7.

2.2.1 Isobar and Coupled Channels Models

Tree-level isobar models attempt to describe the hadronic reaction by evaluating various tree-level Feynman diagrams for the resonant and non-resonant exchange of mesons and baryons. The possible particle exchanges in a reaction can be classified as s-, u-, and t-channel reactions, which can be related to the physical situation of the particle exchange. Exchange of excited states can occur in these channels, including N* resonances, which are exchanged in the s-channel. The Feynman diagrams for $\gamma p \rightarrow K^+\Lambda$ and $\gamma p \rightarrow K^+\Sigma^0$ are shown in figure 2.13.

The isobar model treats every particle in the reaction as an effective field, with associated properties including photocoupling amplitude, mass, and strong decay width. This approach produces a reliable first-order description of resonance parameters, but does not account for channel coupling effects or final state interactions.

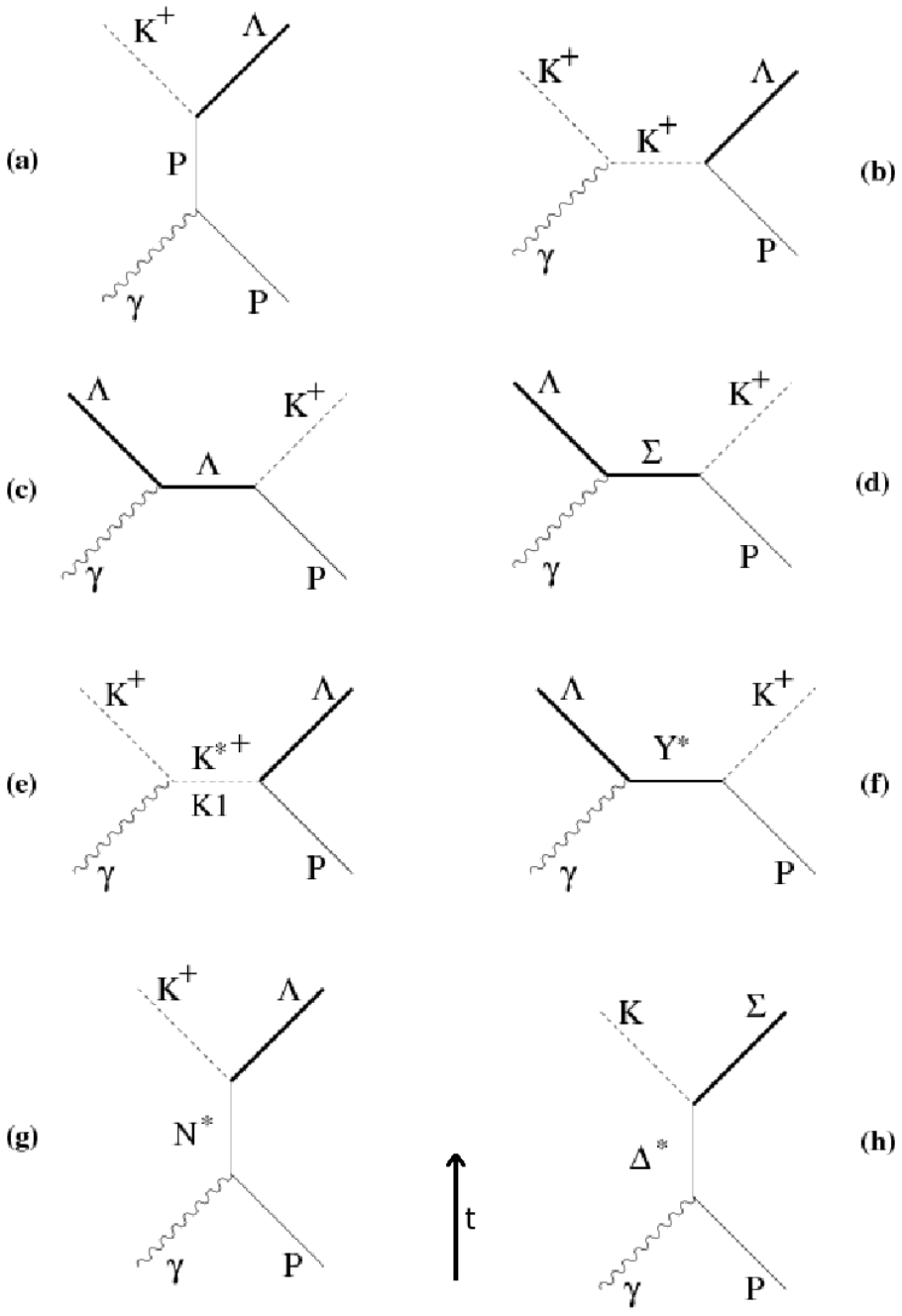

Figure 2.13: Feynman diagrams for the $\gamma p \to K^+\Lambda$ reaction are shown in diagrams (a) to (g), with the additional diagram (h) included for $\gamma p \to K^+\Sigma$. The time axis is oriented in the vertical direction. Diagrams (a) to (d) represent the Born terms and (e), (f) and (g) represent resonant contributions from the t, u and s-channels, respectively. From [23].

One of the first such isobar models to show evidence for a potential missing resonance in strangeness photoproduction was that of Mart and Bennhold [22]. This model attempted to reproduce the SAPHIR cross section results for $\gamma p \rightarrow K^{+}\Lambda$, and required the inclusion of a $D_{13}(1960)$ resonance from the constituent quark model of Capstick and Roberts [13] to replicate the structure seen at W $\approx$ 1.9 GeV. However, further investigations [21] have shown it is possible to reproduce these cross section results without the $D_{13}(1960)$ resonance, underlining the need to measure polarisation observables to increase the available information to feedback into theoretical models. Figures 2.14 and 2.15 show the Mart and Bennhold predictions of the cross section and the beam polarisation observable, respectively.

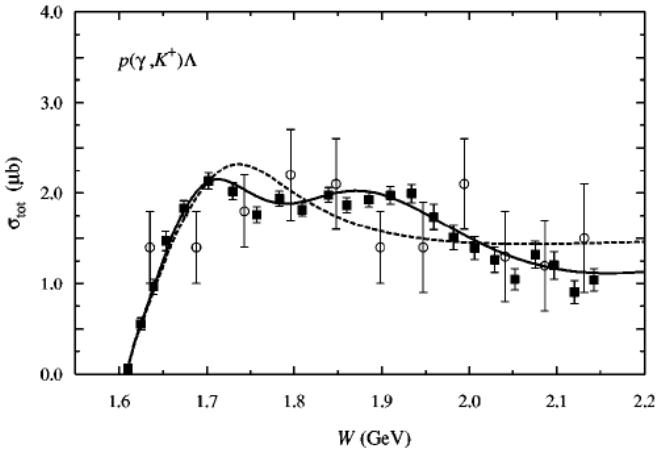

Figure 2.14: Total cross section calculations compared with SAPHIR data. The solid line indicates predictions of Mart and Bennhold with a $D_{13}(1960)$ resonance, the dashed line without. Image from [22].

The coupled channels approach attempts to overcome the failure of tree-level isobar models to account for intermediate πN states, as well as final state interactions. It is believed that the amplitudes of $\gamma N \rightarrow \pi N$ in the multi-step sequence $\gamma N \rightarrow \pi N \rightarrow KY$ will have a large effect on kaon photoproduction. Figure 2.16 shows coupled channels model calculations compared to differential cross section data from CLAS and SAPHIR, with different solutions arising from different descriptions of the background contributions to $K\Lambda$.

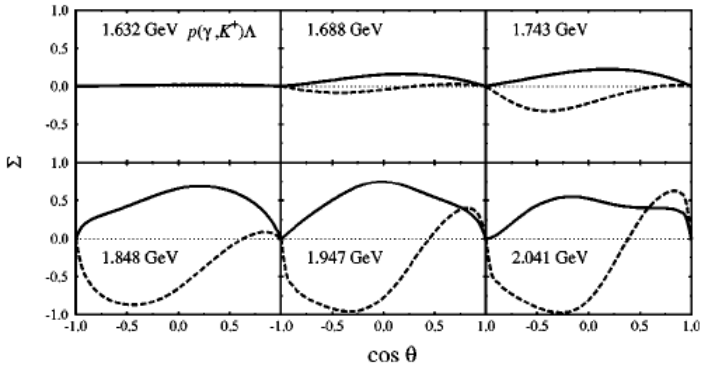

Figure 2.15: Photon asymmetry predictions of Mart and Bennhold as a function of $cos\theta^{K+}_{cm}$ for a series of centre-of-mass energy bins. The solid line indicates predictions with a $D_{13}(1960)$ resonance, the dashed line without. Image from [22].

2.2.2 Regge Models

At higher energies, Regge models are able to provide an accurate description of particle physics data. These models start by extending angular momentum into the complex plane, and groups particles with the same internal quantum numbers but different spins into "Regge trajectories". Photoproduction processes are then described at high energies, where individual resonances can no longer be resolved, by exchanging whole Regge trajectories rather than individual particles.

Regge approaches are expected to be valid at high energies and forward angles, but recent studies suggest that they could also reasonably describe meson photoproduction in the resonance region.

Corthals, et. al. [54] have adopted a "Regge-plus-resonance" approach to reproduce cross sections and polarisation predictions in hadronic reactions. This method differs from isobar models by using Regge exchange in the t-channel to describe the KY background, with a number of s-channel resonances added to extend the model into the resonance region. Higher-energy data can then be used to constrain the background contributions, as the resonances must vanish at these energies, leaving resonance couplings as the only free parameters in the resonance region.

Figure 2.17 shows several Regge-plus-resonance calculations for the beam polarisation observable; RPR-2, -3, and -4. RPR-2 and RPR-3 contain the $P_{13}(1900)$ and $P_{11}(1900)$ resonances, whereas RPR-4 does not. These studies have suggested that fine tuning of the background in models may be just as effective at explaining

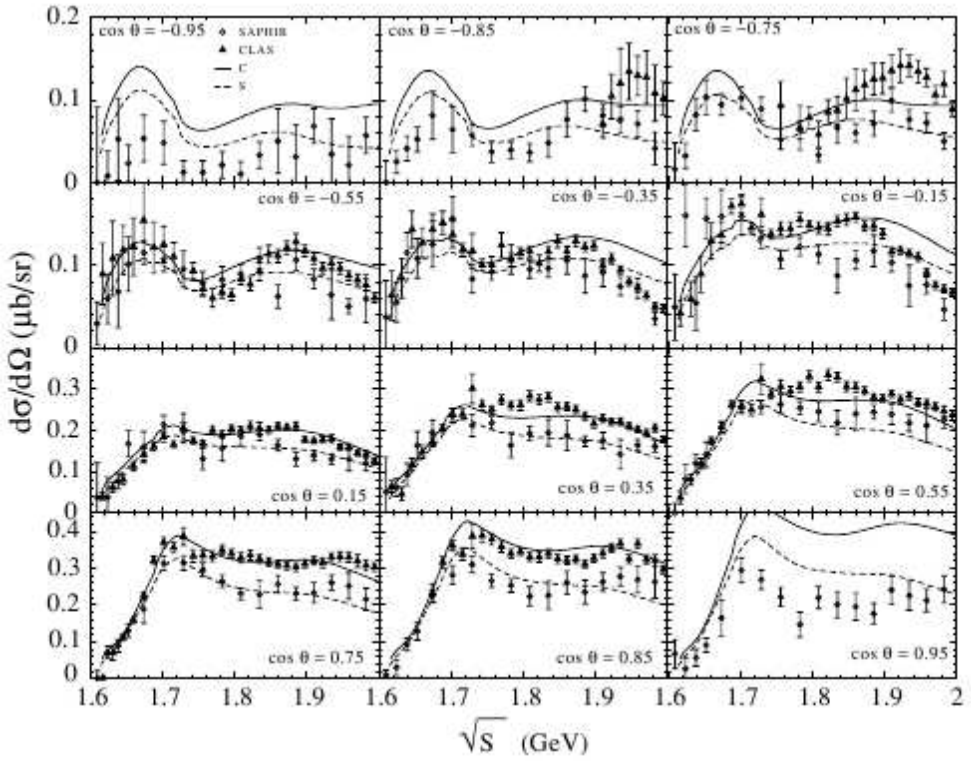

Figure 2.16: Predictions of the differential cross section via the coupled channels model of Shyklar et. al. [53]. The two lines differ in their description of the background contributions to $K^+\Lambda$, and are compared with CLAS and SAPHIR data.

certain structures in the polarisation observable results as the inclusion of a missing resonance [54].

2.2.3 Partial Wave Analyses

Partial Wave Analysis (PWA) is a process which separates the background and resonant contributions to the reaction amplitudes into a series of partial waves within a model framework. These waves are parameterised in terms of the properties of resonances, and the resulting functions are then fitted to experimental data. By introducing constraints via the inclusion of known and missing resonances into the models, signatures of resonances in the data can be identified.

The SAPHIR cross section results shown in figure 2.1 also show results of a PWA by Sarantsev et. al. [35], and figure 2.18 shows the same PWA results alongside CLAS data on the Λ recoil polarisation.

As discussed in chapter 1, over-determined measurements of the polarisation ob-

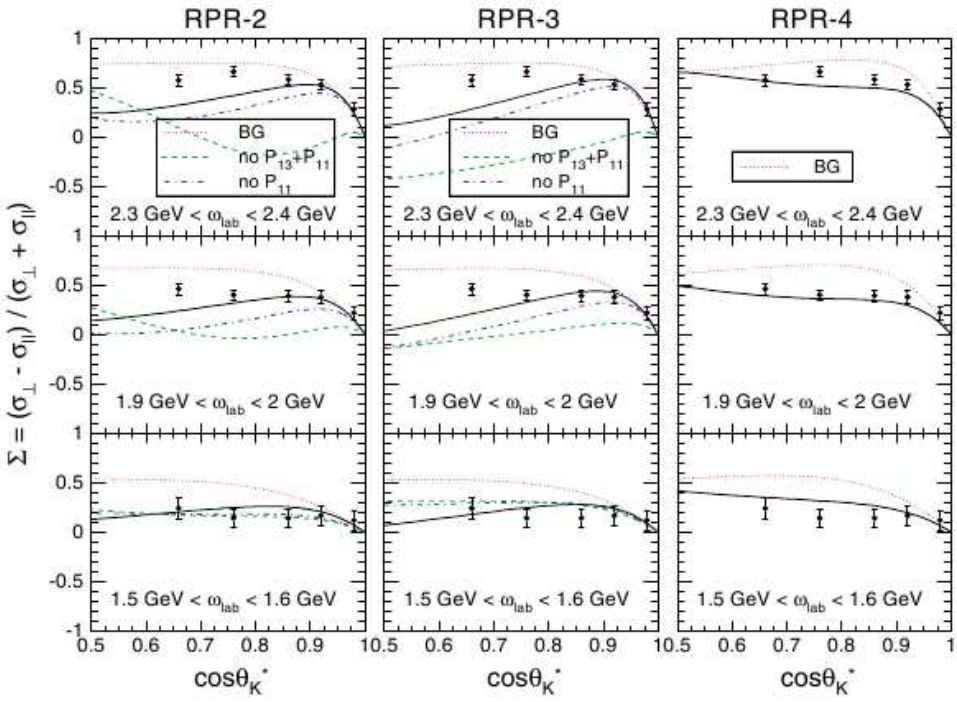

Figure 2.17: Regge-plus-resonance calculations of the photon asymmetry compared to LEPS data. RPR-2 and RPR-3 models contain the $P_{13}(1900)$ and $P_{11}(1900)$ resonances, RPR-4 does not. Image from [54].

servables associated with strangeness photoproduction will allow partial wave analysis to be carried out independently of theoretical models, and resonant contributions to be disentangled from background without ambiguity.

2.2.4 Predictions of the G Observable

Kaon-MAID is a unitary isobar model which employs an effective Lagrangian approach to describe photo- and electroproduction of kaons [44]. A web interface exists from which predictions of G observable for $K^+\Lambda$ and $K^+\Sigma^0$ were extracted for the energy bins used in the analysis. For $K^+\Lambda$, these were extracted with and without the inclusion of a $D_{13}(1900)$ resonance, and for $K^+\Sigma^0$ a full set of resonances, including $S_{31}(1900)$ and $P_{31}(1900)$.

The beam-target observables, including G, are predicted to be highly sensitive to resonances, particularly the $D_{13}(1900)$ missing resonance, although these predictions are based on models informed by incomplete data and may not necessarily match the values that will be measured. Figure 2.19 shows Kaon-MAID predictions of G,

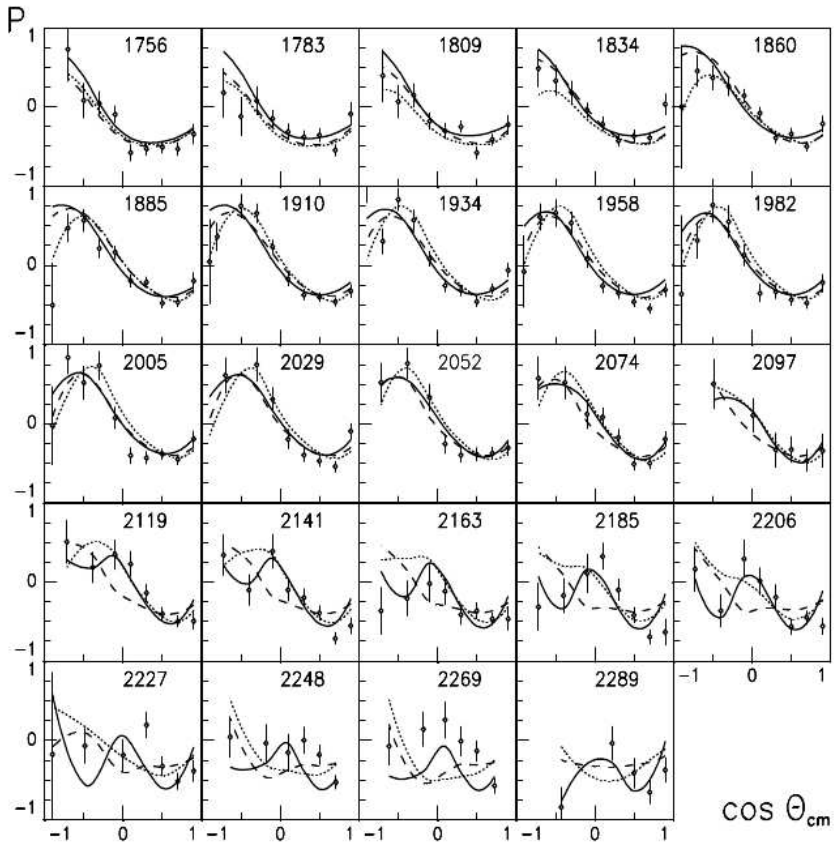

Figure 2.18: Results of the partial wave analysis results of Sarantsev et. al. on CLAS recoil polarisation data for the reaction $\gamma p \rightarrow K^+\Lambda$ as a function of $cos\theta^{K+}_{cm}$ for a series of photon energy bins. The solid line represents the fit results, the dashed line is the fit with $D_{13}(2170)$ omitted, and the dotted line omits the $P_{11}(1840)$. Image from [35].

with and without the inclusion of the $D_{13}(1900)$ resonance.

2.3 Summary

With a new generation of experiments featuring polarised beams and targets, as well as recoil polarisations via the self-analysing hyperon channels, the database of polarisation observables associated with strangeness photoproduction is beginning to look complete. The g9 (FROST) experiments are intended to extend the available polarisation data further, making first measurements of beam-target and target-recoil double observables, providing further constraint to the theoretical models used to interpret experimental data in terms of the excitation spectrum of the baryon.

The remainder of this thesis describes the setup of the g9a experiment at Jef-

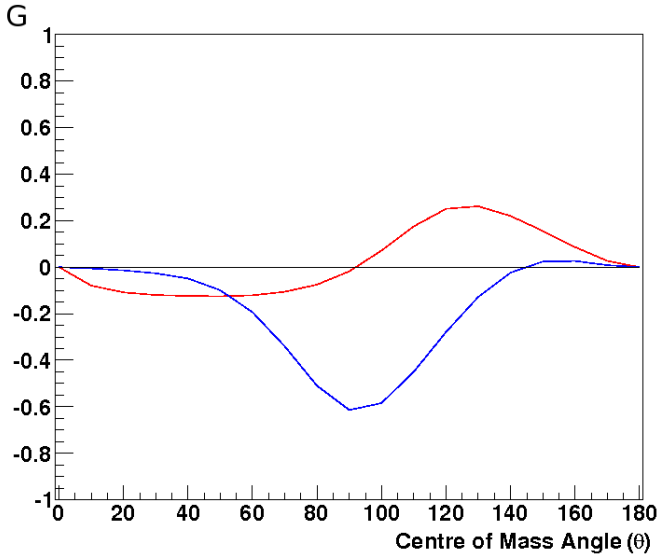

Figure 2.19: Kaon MAID predictions of the G observable for the reaction $\gamma p \rightarrow K^+\Lambda$ at photon energy of 1.7 GeV with (blue) and without (red) the $D_{13}(1900)$ missing resonance.

ferson Lab, and the analysis performed to obtain measurements of the Σ and G polarisation observables from a polarised target on the $K^+\Lambda$ and $K^+\Sigma^0$ strangeness photoproduction reactions.

Chapter 3

Experimental Detectors and Apparatus

In this chapter, the apparatus and detector components used to study the reactions $\gamma p \to K^+\Lambda^0$ and $\gamma p \to K^+\Sigma^0$ during the g9a run period will be described. The g9a (FROST) experiment [23] was performed at the Thomas Jefferson National Accelerator Facility, Newport News, Virginia, and ran from October 2007 until February 2008, using the CEBAF Large Acceptance Spectrometer (CLAS) in experimental Hall B, the FROST polarised target, and a polarised photon beam.

3.1 Experimental Overview

Figure 3.1 shows the basic setup of the g9a experiment. The electron beam from CEBAF is delivered to the hall, and passes through a radiator, emitting bremsstrahlung photons as the beam interacts with the radiator. The mixed photon-electron beam enters the photon tagging spectrometer, where the electrons are swept out of the beamline by a dipole magnet and detected by the tagger to determine photon beam energy. The photon beam then continues through a collimator before interacting with the FROST target, positioned at the centre of CLAS. A range of particles are produced as a result of the beam-target interaction, which are detected by the various detector systems comprising CLAS, and the data recorded used to analyse these reactions.

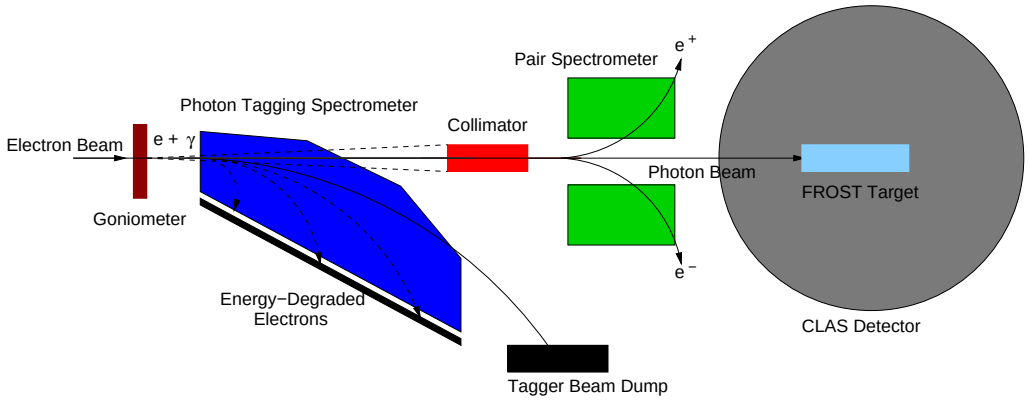

Figure 3.1: Layout of the equipment in Hall B for the g9a/FROST experiment (not to scale).

3.2 Jefferson Lab

The Thomas Jefferson National Accelerator Facility, also known as Jefferson Lab (or JLab), is a United States Department of Energy (DoE) national facility located in Newport News, Virginia [55]. Its research efforts are primarily focussed on studies of the atomic nucleus at quark and gluon level, at the energy scale where nuclear physics meets high energy particle physics.

This work is carried out using the Continuous Electron Beam Accelerator Facility (CEBAF) [56], which produces a 6 GeV electron beam that can be simultaneously delivered to up to three experimental halls, each of which contain various pieces of experimental equipment, designed and optimised for the experimental programme of each hall.

3.3 CEBAF

CEBAF, the Continuous Electron Beam Accelerator Facility [56] at Jefferson Lab, is a continuous wave electron accelerator, providing a high-luminosity electron beam of energies up to 6 GeV simultaneously to up to three experimental halls. The accelerator is of a racetrack configuration, 7/8 of a mile in circumference, with a series of liquid-helium cooled niobium cavities forming an anti-parallel pair of superconducting radio-frequency linear accelerators (linacs), one along each straight section, and a pair of re-circulation arcs to direct the electrons between the linacs.

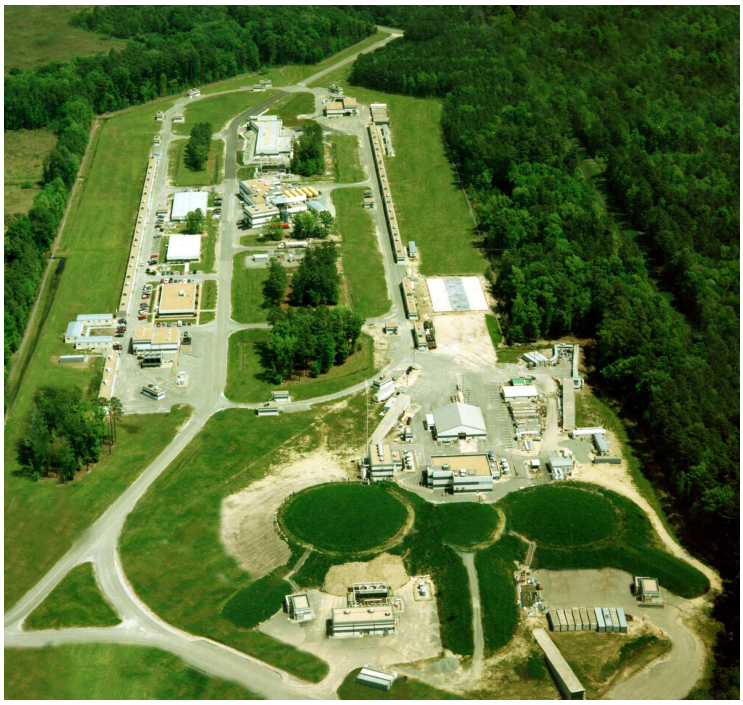

Figure 3.2: Aerial view of the Jefferson Lab accelerator, CEBAF, showing the racetrack configuration of the accelerator and the three experimental halls (the circular grass-covered hills in the foreground).

3.3.1 Beam Production

A schematic overview of CEBAF is shown in figure 3.3. Electrons are produced by a laser incident on a strained Gallium Arsenide (GaAs) photocathode, and initially accelerated by an anode. The electrons are then further accelerated to 67 MeV by two Superconducting Radio-Frequency (RF) cavities and after separation into ∼2 ns beam buckets, they are injected into the accelerator beamline. The electrons then enter the racetrack beamline and travel around the accelerator up to five times, or 'passes', gaining up to 600 MeV in each linac, for a total of 1.2 GeV per pass, before being simultaneously delivered to up to three experimental halls with maximum energy of 6 GeV.

The initial electrons are produced by one of three separate lasers, pulsed at 499 MHz, allowing beams of independent current and polarisation to be produced for, and delivered to, each hall. The simultaneous production of three beams in this way gives rise to CEBAF's characteristic 2.0005 ns beam "bucket" structure. By passing the laser light through a device known as a Pockels cell, polarised light is produced,

leading to the production of polarised electrons from the photocathode [57].

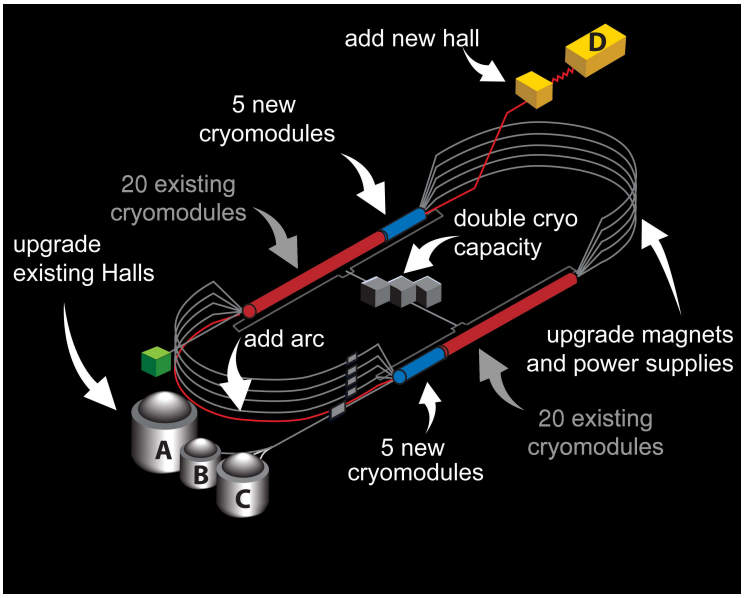

Figure 3.3: Overview of CEBAF, showing the racetrack configuration of the beamline, which consists of two linacs and two recirculation arcs, the three current experimental halls, and the plans for the 12 GeV upgrade, including the construction of a fourth experimental hall.

Each of the two linacs are made up of 20 Superconducting RF cryomodules, consisting of 8 cavities, cooled with liquid helium to 2 K. This technology was chosen during the design stage of CEBAF in the 1980's, when it became clear that realising the design requirements using conventional RF accelerators operating at room temperature would be expensive to construct and operate, limited in performance and difficult to upgrade in energy. Some of these difficulties, particularly those associated with the operating costs of the system were overcome by employing superconducting technology, with CEBAF becoming the largest application of the technology in the world at the time. Each cavity has its own Klystron, which sets up a standing electromagnetic wave inside the cavity, this produces a charge gradient in the cavity which accelerates the electron.

At the ends of the linacs, a series of dipole magnets are positioned along the arcs of the CEBAF beamline, bending the beam emerging from one linac a full 180° and directing it into the next linac, where it is further accelerated. Because the electrons increase in energy with each pass, electrons of differing energies (having passed through the linacs a different number of times) must be bent in the same radius in

order to enter the next linac. This is achieved by splitting the emerging beam into 5 sub-beams, which are directed into individual sets of dipole magnets, tuned to the appropriate electron energy, along the recirculation arcs [56]. By recirculating the beam in this manner, the beam energies required for JLab experiments can be reached with fewer cavities and their associated cryogenics, reducing the costs associated with building and running the accelerator.

3.3.2 Beam Delivery and the Experimental Halls

Following acceleration, the beam is extracted from CEBAF and delivered to the halls by rf separator cavities operating at the same frequency (499 MHz) as the laser pulsing of the injector. These separators can extract the beam after any of the five passes through the accelerator, enabling each hall to be provided with a beam of differing energies to each other, ranging from a few hundred MeV to just over 6 GeV, quantised by *number of passes* $\times$ *energy gained in each pass*.

The experimental halls, designated A, B, and C, are located off the southern linac and have different set-ups optimised for studying different aspects of nucleon structure. Halls A and C receive beam at currents of order $100\mu A$, whilst Hall B receives a lower beam current of the order of tens of nanoamps, due to the limits on luminosity imposed by the operation of the large acceptance detection system in Hall B. This simultaneous production and delivery of beam to three halls with differing energies and such a large range between beam currents is a major achievement of CEBAF. Table 3.1, provides a summary of CEBAF's operating characteristics.

As part of the 12 GeV upgrade of CEBAF [58], a fourth experimental hall, Hall D, is currently being constructed at the end of the northern linac, and features an extra half pass of the accelerator in order to reach the full 12 GeV post-upgrade energy. Halls A and C are the largest of the three existing halls, and perform experiments using the electron beam directly. In the smaller Hall B, this can also be the case, however, the electron beam can also be used to produce a beam of photons via the bremsstrahlung process for performing photonuclear experiments, which is discussed later in this chapter.

Duty Factor	Continuous Wave
Number of Passes	5
Energy gain per pass	1.2 GeV
Electron Beam Energy Range	0.6 GeV to 6 GeV
Number of Cryomodules	40
Electron Polarisation	85%
Typical Beam Current	$\sim 100 \mu A$ (Halls A and C) $\sim 10 nA$ (Hall B)

Table 3.1: Summary of CEBAF operating characteristics

3.4 Hall B

Hall B is the smallest of the three existing experimental halls at Jefferson Lab, and contains several pieces of equipment used in the experiments that make up the Hall B physics program. The configuration of the Hall B equipment varies depending on the requirements of each experiment for beam, target, and detector systems used. Photon beam experiments using CLAS, such as g9a (outlined in section 3.1), share the following common elements to their set up; The electron beam from CEBAF is delivered to the hall, and passes through a radiator, producing a photon beam via bremsstrahlung (or coherent bremsstrahlung for linearly polarised photons, discussed later) [59]. The energy of the photons produced are determined by measuring the energies of the degraded electrons using the tagging spectrometer, and the photon beam is then incident on a target cell, positioned near the centre of CLAS, which detects reaction products with almost full angular coverage. The locations of the CLAS detector and the photon tagger in Hall B are shown in figure 3.4

The remaining sections of this chapter describe the detector systems and apparatus used in Hall B for the g9a run period.

3.5 Coherent Bremsstrahlung Facility

For photon experiments in Hall B, including g9a, the photon beam is a secondary beam produced from the CEBAF electron beam. The g9a experiment utilises both circularly and linearly polarised beams, in order to access a range of single and double polarisation observables [23]. These photon beams are produced in Hall B

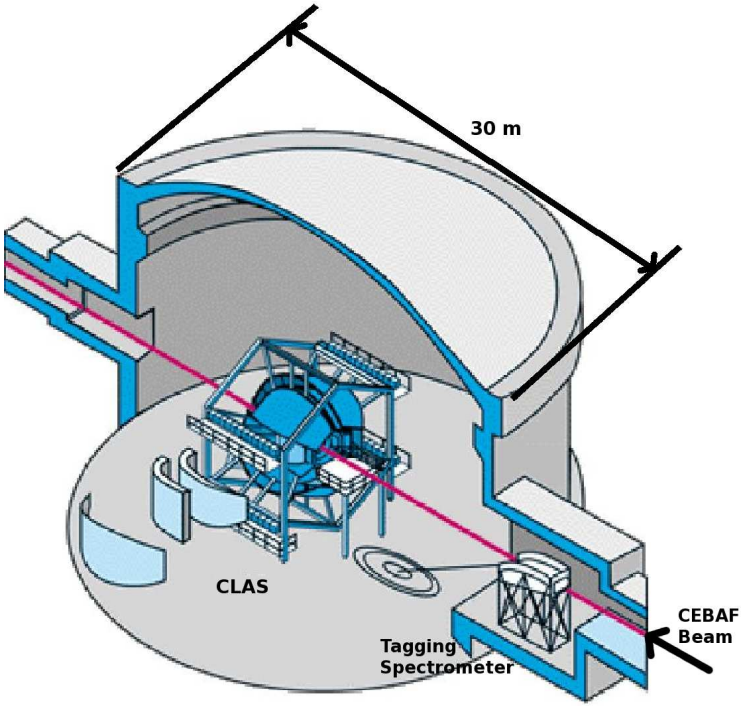

Figure 3.4: The basic setup of Hall B for photonuclear experiments, showing the relative positions of the tagging spectrometer and the CLAS detector, and the direction of the incoming CEBAF electron beam.

via the bremsstrahlung process, in which electrons incident on a suitable radiator are decelerated by the electromagnetic field of the of the nuclei in the radiator, emitting a photon. If an amorphous radiator is used, the photon beam produced will have an energy spectrum that displays a characteristic $\sim \frac{1}{E}$ dependence, as shown in figure 3.6 (top).

The extraction of the G polarisation observable, the primary aim of the work presented in this thesis, required the use of a linearly polarised photon beam, in addition to the longitudinally polarised target discussed later in this chapter. This linearly polarised photon beam was produced via the coherent bremsstrahlung process (CB), where the electron beam is scattered from a diamond radiator, which has a regular lattice structure. If suitably aligned, the bremsstrahlung photons produced will have discrete fractional energies, corresponding to specific momentum transfers from the electrons to the crystal lattice, and the energy spectrum will exhibit a "coherent peak" structure (the middle image in figure 3.6). If the orientation of the diamond is carefully chosen, so as to scatter off a particular reciprocal lattice

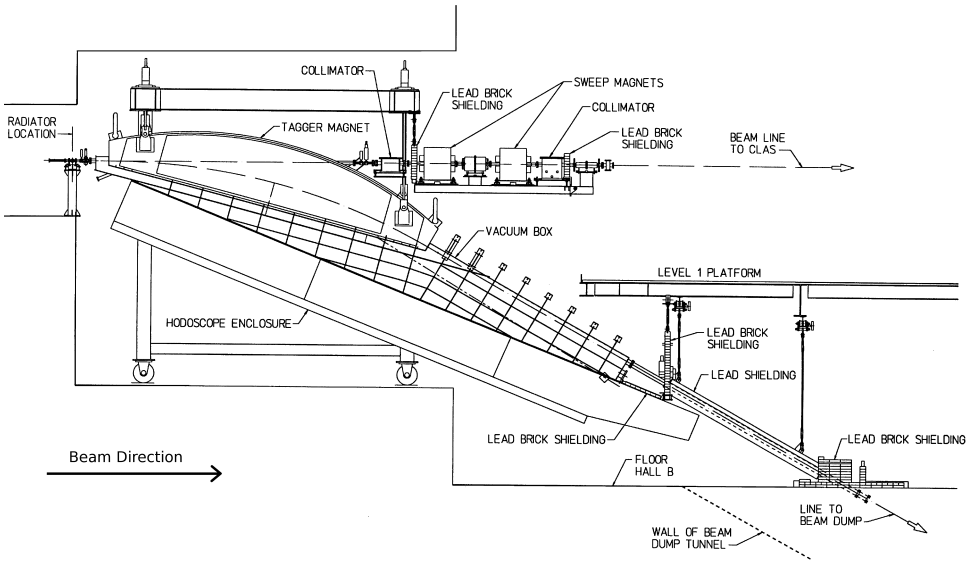

Figure 3.5: Schematic diagram of the coherent bremsstrahlung facility in Hall B [60]. The goniometer, which holds and orientates the diamond radiator, is not shown.

vector, then the photons produced will have a high degree of linear polarisation, particularly in the region of the coherent peak.

The coherent bremsstrahlung facility in Hall B consists of several pieces of equipment used to produce the photon beam for experiments. These include the goniometer, which controls the orientation of the radiator, the radiators used for the production of photons, the photon tagging spectrometer, which determines the photon beam energy, and the collimator. The layout of this facility and the relative locations of the equipment with respect to CLAS can be seen in figures 3.1, 3.4 and 3.5 and its main components are described below.

3.5.1 Radiator

The properties of diamond make it suitable for use as the radiator in coherent Bremsstrahlung, its small lattice constant and high Debye temperature result in small thermal motion of the atoms in the lattice, and a lattice structure that suffers minimal thermal effects.

An important consideration when choosing a radiator is its thickness. The thickness of the radiator affects the angular divergence of the resulting photon beam, due to multiple scattering effects of the electron beam, and crystal defects in the radi-

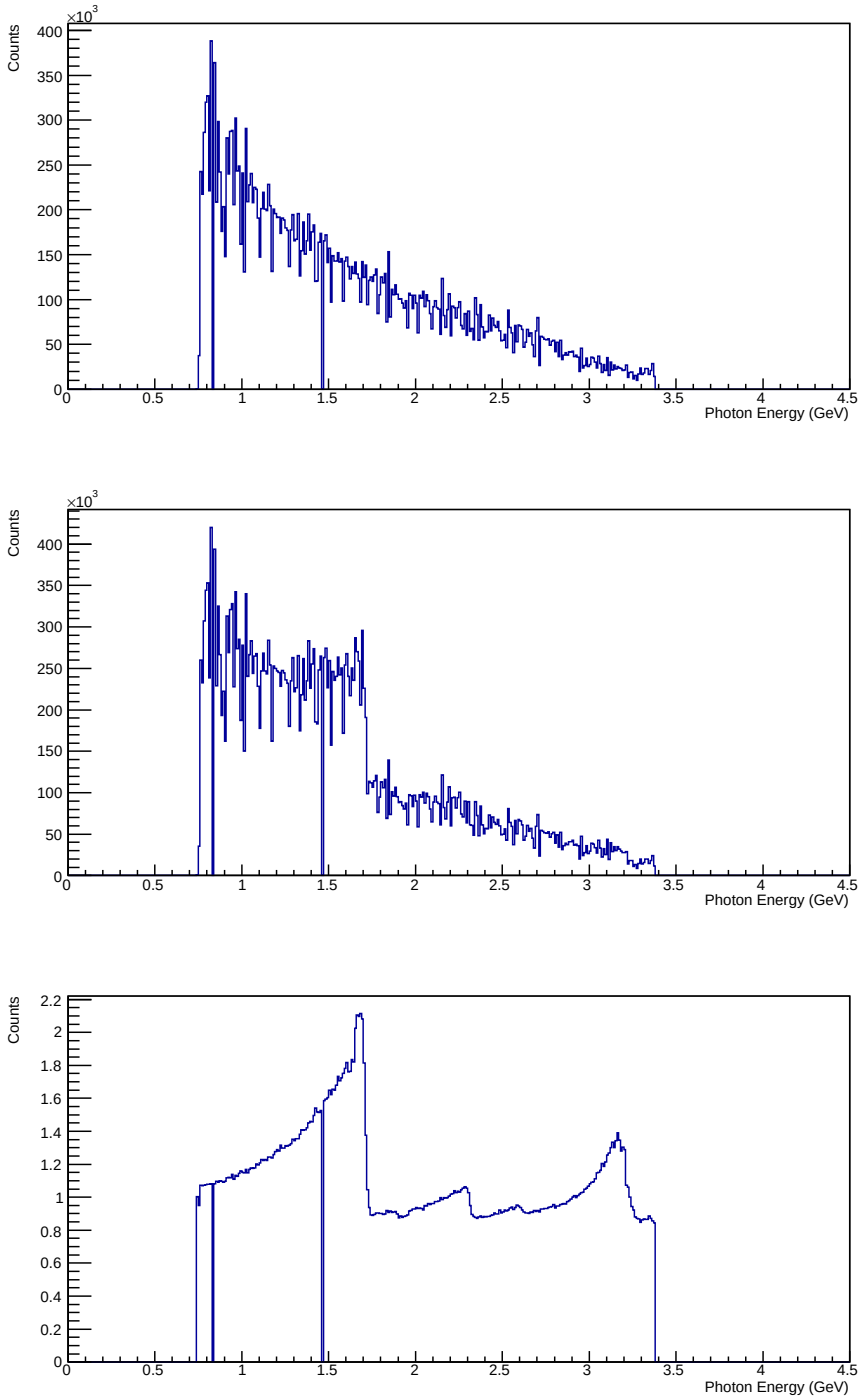

Figure 3.6: (top) incoherent bremsstrahlung spectrum for photons produced by electrons from the CEBAF beam incident on an amorphous radiator, showing a spectrum which falls off with increasing photon energy. (middle) coherent bremsstrahlung spectrum from a diamond radiator demonstrating the characteristic "coherent peak" structure. (bottom) enhancement plot made dividing the coherent and incoherent spectra.

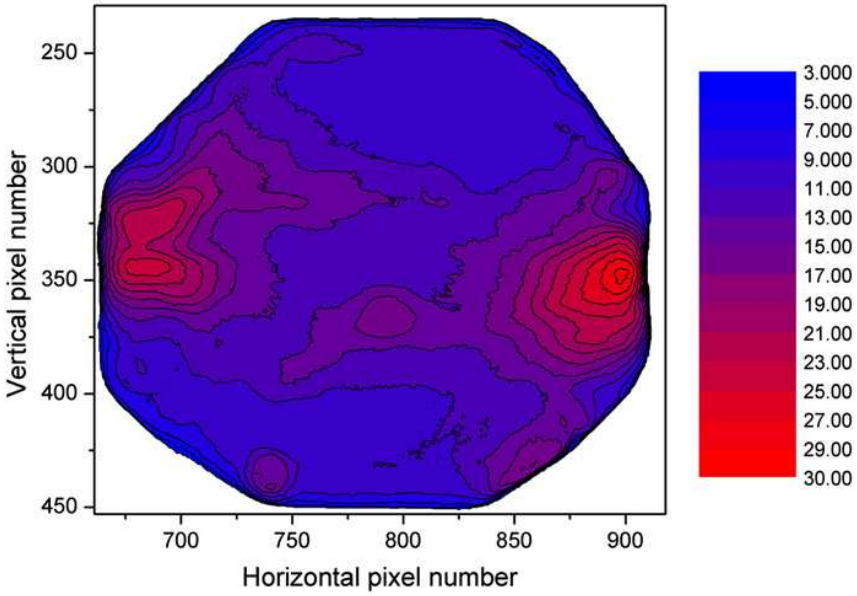

Figure 3.7: Rocking curve width measurements for the [220] plane of a diamond crystal, showing areas of radiation damage, characterised by a wider rocking curve in these regions of the diamond

ator. Minimising this divergence enhances the coherent bremsstrahlung spectrum, so the diamond used should be as thin as the considerations of manufacturing and positioning of the radiator allow.

For the g9a experimental run, a $50\mu m$ diamond was used, cut in the [100] orientation, and photons produced by scattering the electron beam off the [022] reciprocal lattice vector. Several methods can be employed to assess the quality and suitability of individual diamond crystals for producing coherent bremsstrahlung, including optical polaroid analysis, X-ray topography and rocking curve measurements [61], the latter of which is demonstrated in reference [62], and a rocking curve measurement of a diamond used for coherent bremsstrahlung shown in figure 3.7.

3.5.2 Goniometer

Coherent bremsstrahlung requires precise alignment of the diamond, in order to produce a highly polarised beam by scattering off the appropriate crystal planes associated with a particular reciprocal lattice vector. A poorly aligned crystal will produce a photon beam with a lower degree of linear polarisation.

To be able to align the diamond with respect to the electron beam with the

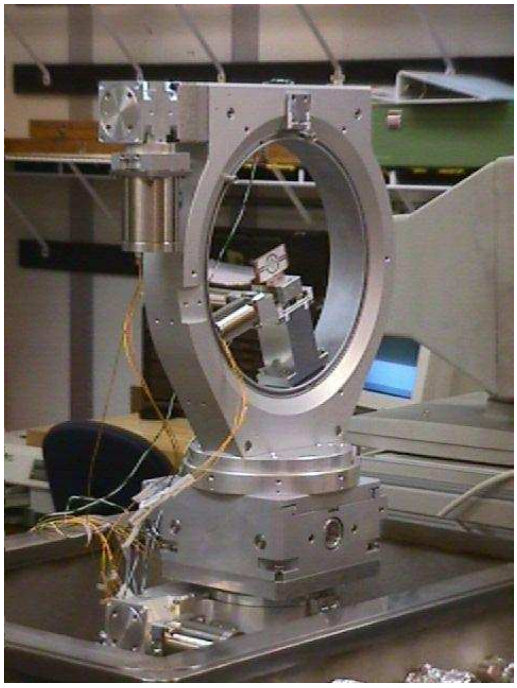

Figure 3.8: The George Washington University Goniometer. The target ladder, which holds the radiators, is visible in the centre of the device.

required level of precision, it is mounted in a goniometer, a device which can move the diamond horizontally, vertically and rotationally about all three axes with a precision greater than 10 μrad. This precision enables the coherent peak to be positioned to a precision of less than 1 MeV

The goniometer was built by George Washington University and is shown in figure 3.8. It is positioned several metres upstream of the tagger, and kept under vacuum. The goniometer holds several radiators on a target ladder, including the diamond and amorphous carbon, which can be moved in and out of the beamline, as required.

3.5.3 Photon Tagging Spectrometer

The Hall B photon tagging spectrometer is used to determine the energy of the photon beam produced via the bremsstrahlung process. The tagger consists of a dipole magnet and a hodoscope, which has two planar arrays of plastic scintillators providing energy and timing information from the detection of the energy-degraded electrons from the bremsstrahlung process. The system is oriented vertically, i.e.

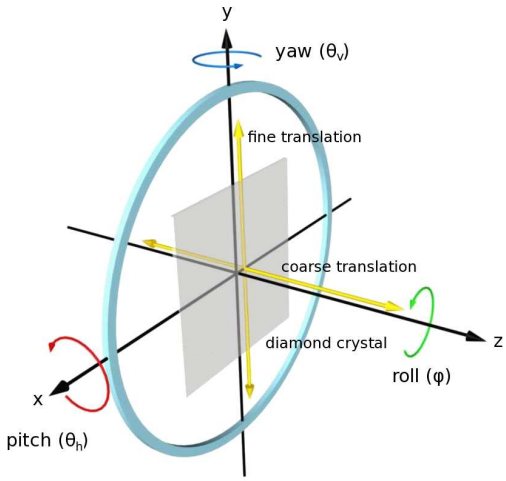

Figure 3.9: Simplified diagram showing the degrees of freedom of the George Washington University Goniometer.

the electron beam is directed downwards.

Photons produced from the radiator proceed straight through the tagger and into CLAS, where they interact with the target. Electrons, however, are deflected out of the beamline by the tagger's dipole magnet and onto the tagger hodoscope. Because the energy transferred from the electron to the scattering nucleus in the bremsstrahlung process is negligible, the energy of the photon beam can be determined via the relation $E_\gamma = E_0 - E_e$, where E_0 is the electron beam energy before interaction with the radiator, determined by the accelerator, and E_e is the energy of the electron detected in the tagger. This relies on making a timing coincidence between the experimental trigger and the tagger focal plane hodoscope.

The position in the hodoscope at which the electron is detected determines its energy, an electron which produced a lower energy photon is deflected less than one which lost more energy producing a higher energy photon. Electrons that did not produce a photon are deflected into the tagger beam dump.

The two planes of scintillators in the tagger hodoscope are referred to as the E-plane and the T-plane, shown in figure 3.10. Each is made up of a series of overlapping scintillator paddles, with surfaces normal to the beam trajectory. The E-plane consists of 384 scintillator paddles, each equipped with its own photomultiplier tube, and divided into 767 E-bins due to overlaps. The E-plane provides

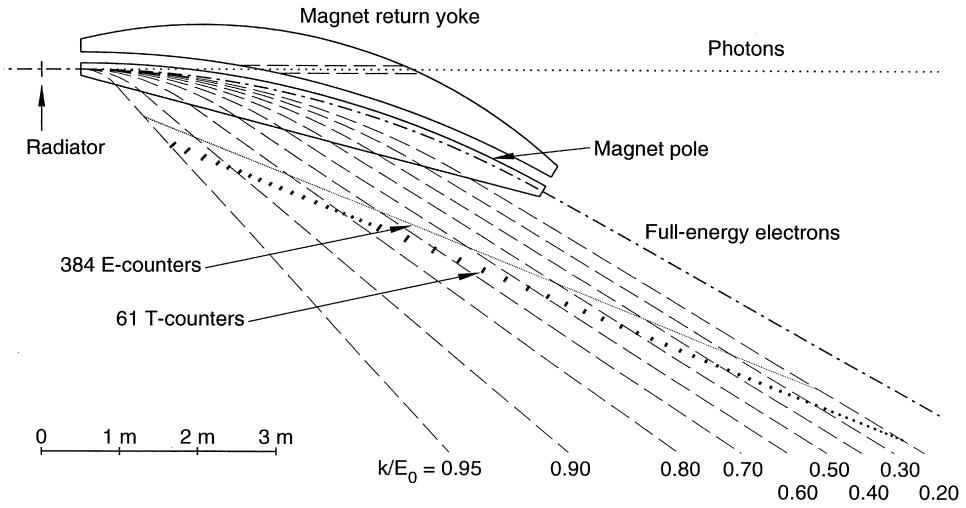

Figure 3.10: Diagram of the tagger layout showing the relative positions of the E and T-counters [60].

the momentum information on the degraded electrons, with an energy resolution of $0.001E_0$. Each scintillator in the E-plane is 20 cm long and 4 mm thick, with width between 6 and 18 mm, spanning approximately equal momentum intervals of around $0.003E_0$.

The purpose of the T-plane is to associate a tagged photon with the correct beam "bucket", it features 61 overlapping scintillators, divided into 121 T-bins due to overlaps between adjacent scintillators, read out via a photomultiplier tube at each end. The T-plane is arranged into groups, with the first 19 scintillators forming the first group and covering the photon energy range of 75% to 95% of incident electron energy, and the remaining scintillators covering the remaining energy range. To achieve the required timing resolution (∼300 ps) for associating a photon with an individual beam bucket, the T-plane scintillators are thicker than those used in the E-plane, at 2 cm.

3.5.4 Collimator

The angular spread of coherent bremsstrahlung photons is less than that of the incoherent bremsstrahlung in the region of the coherent peak. To further increase the degree of linear polarisation in the coherent peak, it is tightly collimated.

The collimator is located immediately downstream of the tagger, and comprises

a series of Nickel diskettes with a small hole in the centre. These are stacked in a cylindrical sheath of stainless steel, with four 4 mm cubic scintillators sandwiched between them. This allows online monitoring of the count rates in the scintillator by measuring the rate of e^+e^- pairs produced by photons outside the aperture of the first Nickel disk, which can be related to shifts in beam position.

3.6 CLAS

The main detector in Hall B, used in a variety of photon and electron beam experiments, is the CEBAF Large Acceptance Spectrometer, known as the CLAS detector [29]. CLAS is a multi-layered and segmented arrangement of different kinds of particle detector, roughly 10 metres in diameter, surrounding a cylindrical target holder, which detects reaction products with large coverage of the 4π solid angle, as can be seen in figure 3.11.

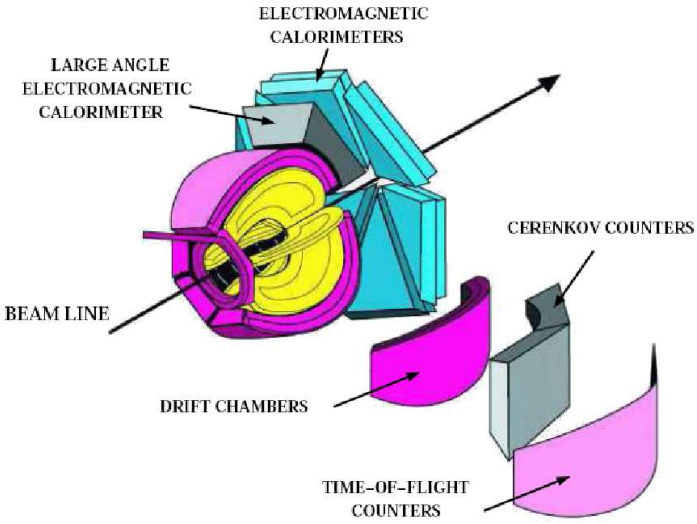

Figure 3.11: Partially exploded schematic of CLAS, showing the component detector systems, and the direction of the incoming photon or electron beam.

The key feature of CLAS is its toroidal magnetic field, produced by six superconducting coils. This design allows large angular coverage for charged particle detection, good momentum resolution, and a field-free central region for the use of polarised targets. The individual detector systems in CLAS are collectively used to obtain information on a particle's mass, momentum and charge as it passes through

CLAS, and this information is used to reconstruct events occurring during an experiment.

When the photon beam interacts with a target in the centre of CLAS, a series of reaction products are produced. These particles first pass through the start counter, providing the interaction start time, before passing through the drift chambers, where charged particles are tracked as they follow curved paths under the influence of the toroidal magnetic field. They then reach the time-of-flight scintillators, allowing flight time of the particle to be determined, and velocity inferred from momentum measurements from drift chamber tracking. Cerenkov counters and electromagnetic calorimeters provide additional information on forward focussed particles, while a triggering and data acquisition system enables events to be read from the CLAS subsystems and stored for later calibration and analysis.

3.6.1 Torus

The detection of charged particles in CLAS and the determination of their momentum is realised by analysing the curved trajectories of these particles under the influence of a magnetic field. This field is generated by the torus magnet, an arrangement of six superconducting coils around the beamline, which produces a toroidal magnetic field. It is this arrangement of the coils that gives rise to the six sectors of CLAS, with the coils themselves creating the low-acceptance boundary regions between the sectors, reducing the acceptance of CLAS to around 70 % of 4π solid angle coverage. The toroidal field geometry also preserves a field-free central region in CLAS, allowing for the operation of polarised targets, as was the case in the g9a experiment.

The coils are approximately 5 m in diameter, and consist of four layers of 54 turns of NbTi/Cu conductor. These are cooled to 4.5 K by forcing super-critical helium through cooling tubes at the edge of the windings, with the heat load reduced through the use of super-insulation and a liquid-nitrogen-cooled heat shield.

The main component of the torus field is in the azimuthal (ϕ) direction, although this can can deviate somewhat from a pure azimuthal field close to the coils. These effects are reduced by the circular inner shape of the coils, meaning that par-

Figure 3.12: The CLAS toroidal magnet coils, pictured during installation.

ticles crossing a coil's inner boundary do not experience any significant azimuthal deflection.

For the g9a experiment, the torus was operated at 1918 A, around 50% of the maximum design current, with a positive polarity field. This results in positively charged particles being curved away from the beamline, while negatively charged particles are curved towards the beamline. The relatively low field setting has the effect of increasing the acceptance for negatively charged particles, as fewer of these will be curved into the beamline hole at forward angles.

When CLAS is configured for electron scattering experiments, a smaller 'mini-torus' surrounds the target, preventing Møller electrons from entering the inner region of the drift chambers.

3.6.2 Start Counter

For photon beam experiments, the start counter [63, 64] is used to signal the start time for time-of-flight measurements of charged particles. The start counter, shown in figure 3.13, is a ring of plastic scintillators which completely surrounds the target and replaces the mini-torus in photon beam experiments. The timing signal provided by the start counter can be used to measure the time of the hadronic interaction by looking for a coincidence between a signal from the start counter and the tagger. This allows identification of the beam bucket which produced the event in question.

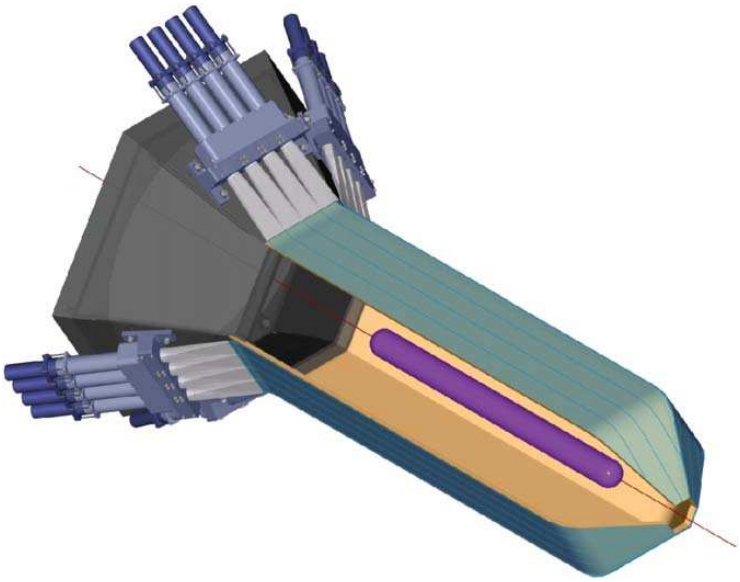

Figure 3.13: Computer generated representation of the start counter in CLAS, with one sector removed to show the position of a 40 cm long target cell.

The start counter is designed to cover the full acceptance of CLAS, and consists of six sectors, each containing four scintillator paddles; continuous pieces of scintillator with a 502 mm long straight "leg" section between two bends, and a tapered end referred to as the "nose". The segmentation of the start counter enables the electromagnetic background to be kept within acceptable limits for final states involving multiple particles by requiring that the hit multiplicity in the paddles is greater than or equal to two.

Readout of signals in the start counter paddles is achieved via a light guide and photomultiplier tube attached at the upstream end, outside the useful acceptance of CLAS. In order to identify the beam bucket that produced an event, and therefore determine the interaction time, sub-nanosecond coincidence of the tagger with the start counter is required. This requires a timing resolution in the start counter of less than 388 picoseconds. The start counter meets this requirement with timing resolution for the "leg" section of the paddles of $\sim$292 ps, and $\sim$324 ps for the "nose".

3.6.3 Drift Chambers

The drift chambers in CLAS are used to determine the momentum of charged particles from the curved trajectories they follow due to the influence of the torus magnetic field. The drift chamber system consists of eighteen separate drift chamber assemblies, arranged as a set of three nested regions for each sector in CLAS, the boundaries of which are defined by the torus magnet coils. Figure 3.14 indicates the location of the three regions of the drift chambers in relation to the torus coils and other detector subsystems of CLAS. The region one drift chambers are contained in a single self-supporting structure, located in an area of low magnetic field close to the target, region two is in an area of high magnetic field, with the drift chambers positioned between the torus coils, and the region three drift chambers are individual structures for each sector, attached to the outer edges of the torus cryostats.

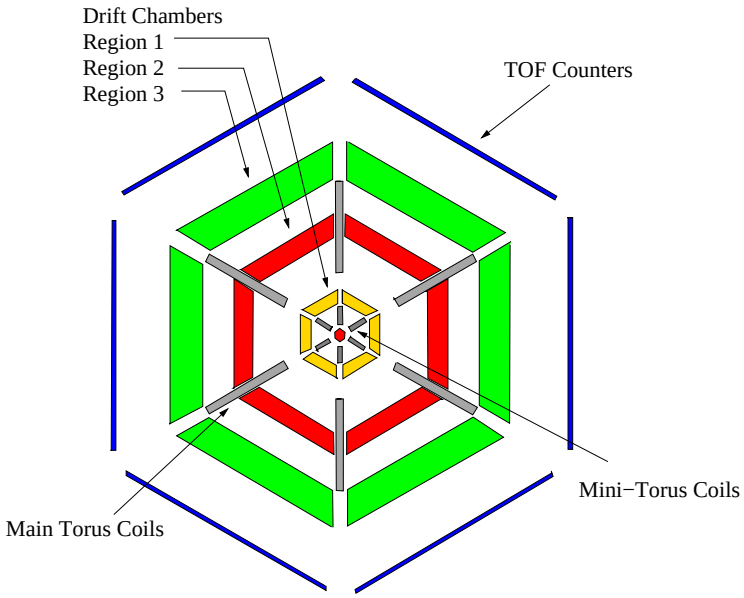

Figure 3.14: Cross-sectional diagram of CLAS, showing the location of the three drift chamber regions relative to the torus magnet coils. The setup shown is for electron beam experiments, with the mini-torus surrounding the target, as opposed to the start counter used in photon experiments, including g9a.

The drift chamber system is designed to enable particle tracking over a polar angle range of 8° to 142°, and provide up to 80% coverage in the azimuthal direction. Each drift chamber assembly consists of two superlayers, comprising six layers of wire

each, referred to as the "axial" and "stereo" superlayers. The axial superlayer is positioned axial to the magnetic field, whereas the stereo superlayer is tilted at a 6° stereo angle in order to provide azimuthal information. For regions 2 and 3, the axial superlayer is the innermost layer, located at a closer radial distance to the centre of CLAS than the stereo layer. This ordering is reversed in region 1, and in addition to this difference, the region 1 stereo superlayer consists of just four layers of wire due to space constraints.

Each of the 18 chamber bodies are designed to support wires between two endplates, with these endplates parallel to their neighbouring coil planes, i.e. the endplates are tilted at 60° with respect to each other. This allows for optimal filling of the wedge-shaped sector volumes defined by the torus coils. This design, with the direction of the wires being approximately perpendicular to the bend plane of charged particles, provides maximum sensitivity to track curvature. The midpoints of the wires are arranged in layers of concentric circles, with the wire positions shifted by half the nominal wire spacing in successive layers.

The sense wires are 20 μm in diameter, and made of Gold-plated Tungsten, this small diameter limits wire tensions and operating voltages, while the choice of material has been made to ensure durability and chemical inertness [65]. The field wires are made of a Gold-plated Aluminium alloy and have a diameter of 140 μm. The long radiation length of Aluminium minimises multiple scattering and its low density allows the field wires to be strung at a lower tension, reducing the forces on the endplates of the drift chamber assemblies. The drift chambers are filled with a gas mixture of 88% Argon - 12% Carbon Dioxide. This mixture is inexpensive, non-flammable, improves the operating lifetime of the drift chambers and minimises multiple scattering and random backgrounds.

3.6.4 Cerenkov Counter

The Cerenkov counter has the dual purpose of contributing to electron triggering and separating electrons from pions. The Cerenkov counters consist of 216 light collection modules, 36 per sector, arranged in 18 segments in θ, covering the polar angles up to 45° for all six sectors [66].

The Cerenkov counter for one segment of CLAS is shown in figure 3.15. Each of these segments is divided into two modules about the symmetry plane bisecting each sector. The segments are filled with perfluorobutane (C_4F_{10}), which was chosen as the radiator gas for its high index of refraction, 1.00153. This results in a high photon yield and a pion momentum threshold of 2.5 GeV/c.

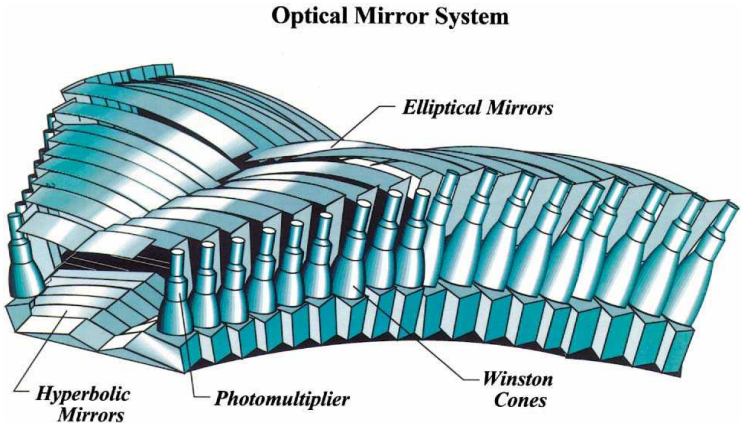

Figure 3.15: The arrangement of the mirrors in the CLAS Cerenkov counter for one sector.

Each module contains several mirrors, which direct Cerenkov light to a light collecting cone and photomultiplier tube (PMT), located at the edges of the segments. The mirrors focus light in the ϕ direction, preserving information on polar angle. As particle trajectories in CLAS lie in planes of roughly constant ϕ, placing the PMTs in the shadow of the torus coils minimises loss of acceptance in the ϕ direction as events from these shadow regions are obscured to the drift chambers.

In tagged photon experiments, such as g9a (FROST), the trigger is derived from the start counter, and there are relatively few electrons. For these reasons, the Cerenkov counter is not used in g9a.

3.6.5 Time of Flight Scintillators

The time-of-flight (TOF) system is a collection of scintillators radially located between the Cerenkov counter and the Electromagnetic Calorimeters [67]. The system has a total scintillator area of 206 m^2, providing polar angle coverage between 8° and 142° and covers the entire azimuthal angular range.

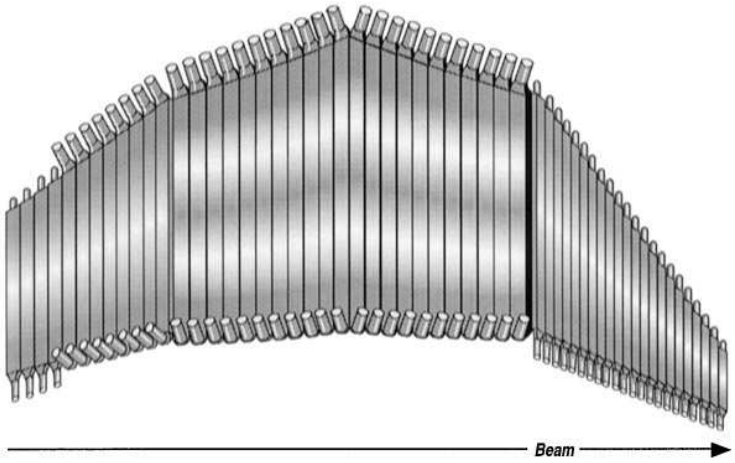

Figure 3.16: The arrangement of scintillators for one sector of the CLAS time of flight system. The four panels comprising the system are shown, with panel 4 on the left through to panel 1 on the right.

The TOF counters are grouped into four panels and each sector contains 57 scintillators, although the last 18 scintillators are coupled into 9 logical pairs, meaning there are 48 logical paddles per sector. This arrangement of scintillators is shown in figure 3.16. The scintillators are positioned perpendicular to the average particle trajectory, i.e. parallel to the drift chamber wires, and subtend around 1.5° of scattering angle. All the scintillators are 5.08 cm thick, and vary in length and width depending on their location. Panel 1, containing scintillators 1-23 are referred to as the forward angle counters and cover scattering angles less than 45°. The scintillators in panel 1 are 15 cm wide, and vary in length from 32 cm to 376 cm. The remaining paddles form the large angle panels 2, 3, and 4, and cover the polar angles greater than 45°. These scintillators are 22 cm wide, with the exception of the final four paired scintillators, which are 15 cm wide, and are between 212 and 445 cm long.

As is the case for the Cerenkov counters, the light guides, photomultiplier tubes and associated cabling and electronics are located in the shadow of the torus coils. The TOF system provides excellent timing resolution for particle identification, and good segmentation for flexible triggering and prescaling. The system is able to separate Kaons and Pions in CLAS up to a momentum of 2 GeV/c, and a typical TOF mass spectrum is shown in figure 3.17.

In conjunction with the reaction start time provided by the start counter, the

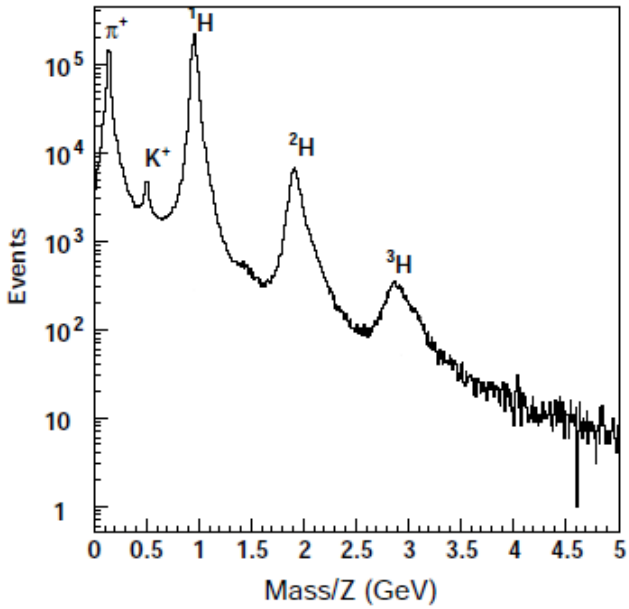

Figure 3.17: Sample TOF mass spectrum showing the ability to identify pions, kaons and protons [29].

TOF system can be used to measure the flight time of particles through CLAS. This can be used to determine a particle's velocity, and when combined with the momentum measurement from the drift chambers, the mass of a particle can be determined via the relation $p = \gamma mv$. This determination of the mass is used in the analysis to perform initial particle identification, as will be discussed in chapter 5.

3.6.6 Electromagnetic Calorimeters

CLAS has two electromagnetic calorimeter systems; the Forward Electromagnetic Calorimeter (EC) [68] and the Large Angle Calorimeter (LAC). These are used for the detection of electrons at energies above 0.5 GeV and neutral particles, such as photons, above 0.2 GeV. The detection of photons is particularly useful for the reconstruction of π^0 and η particles via the measurement of their 2γ decays. A brief discussion of each of these calorimeter systems follows.

3.6.6.1 Forward Electromagnetic Calorimeter

The Forward Electromagnetic Calorimeter covers the θ angle range up to 45° for all six sectors. The EC is made of alternate layers of scintillator strips and lead sheets,

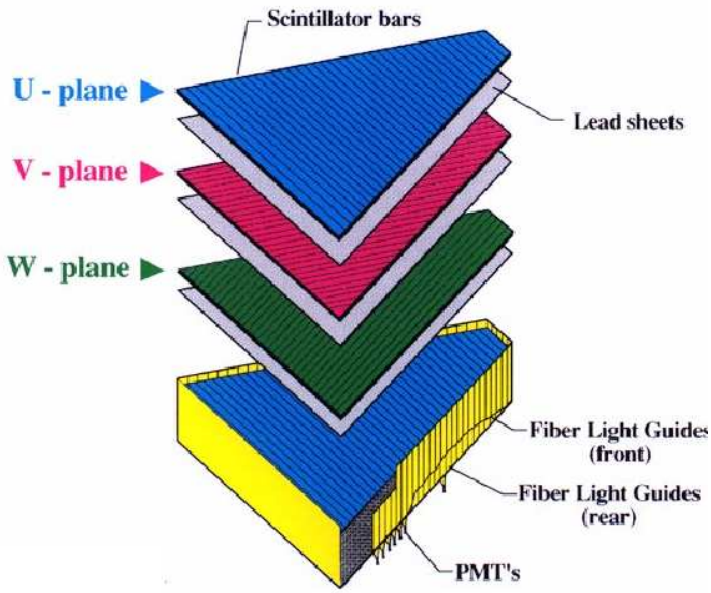

Figure 3.18: Partially exploded view of the CLAS Forward Electromagnetic Calorimeter, showing the three orientations, or views, of the scintillators. Each view consists of 13 layers of scintillator.

16 radiation lengths thick. It consists of six modules, one per sector, resulting in an approximately equilateral triangular shape of each module. The scintillator layers are 10 mm thick, and the lead layers 2.2 mm thick. Each scintillator layer consists of 36 strips, arranged parallel to one side of the triangle. Successive scintillator layers linearly increase in area with distance from the centre of CLAS (a "projective geometry" layout), and are rotated by 120°, giving three orientations, or views, referred to as U, V, and W. Each view has 13 layers, which gives stereo information on the position of the deposited energy in the scintillator.

When a particle enters the EC, it can interact with the scintillator-lead layer, depositing energy. Reconstruction of a valid hit in the EC requires energy deposition in all three views of a module, with intersections between the views corresponding to a hit. By measuring the path lengths from a particle hit position to the readout edge, the energy and time of the hit can then be calculated.

3.6.6.2 Large Angle Calorimeter

The Large Angle Calorimeter consists of two identical modules, which cover only sectors one and two of CLAS, for the polar angle range 45° to 75°. Its main purpose is to extend the detection capabilities of the EC to backward angles. The LAC has a similar layered lead-scintillator construction to the EC, however there are only 33 layers in each module, and successive scintillator layers are rotated by 90°. The LAC relies on the same principles for particle detection as the EC, and the lead and scintillator layers have thicknesses of 2 mm and 15 mm respectively.

3.7 Target

In most configurations, the target cell is positioned near the centre of CLAS, and is typically a cylindrical plastic cell ranging in length from several to a few dozen centimetres, one such cell is shown in figure 3.19. This cell contains the target material, usually liquid Hydrogen, which serves to maximise the density of atomic protons in the target, although other materials such as liquid deuterium or helium have been used in various CLAS photoproduction experiments.

Figure 3.19: A typical target cell used in CLAS photoproduction experiments. The 40 cm long plastic cell is normally filled with liquid hydrogen, which serves to increase the density of atomic protons in the target.

For these previous photon beam experiments, the materials used in the target have been unpolarised, and not suited for use in a polarised target experiment. Such

experiments require a more complicated target material, a means of polarising this target material and of maintaining the polarisation during an experiment. This has led to the development of the Jefferson Lab Frozen Spin Target for the g9/FROST experiments.

3.7.1 Polarised Targets

In a polarised target, the spins of the target nuclei are aligned in the direction of polarisation by some external means. The degree of this polarisation is the proportion of the target nuclei that become aligned. When exposed to a high magnetic field, the spins of the atomic nuclei begin to align, an effect exploited in Nuclear Magnetic Resonance (NMR) applications, referred to as Thermal Equilibrium Polarisation [50]. The time required to de-polarise (and polarise) nuclei in this manner depends on the magnetic field strength and the temperature. A greater degree of polarisation can be attained by maximising the field strength and minimising the temperature.

3.7.2 Dynamic Nuclear Polarisation

Thermal Equilibrium Polarisation has the advantage of working for almost all kinds of nucleus, but requires a large magnet, very low temperatures which limit beam intensity, only provides one mode of polarisation, and can take a very long time to polarise the material. For these reasons, Thermal Equilibrium Polarisation is not suitable for producing polarised targets for nuclear physics experiments such as those performed in CLAS.

One alternative method, used for solid polarised targets, is Dynamic Nuclear Polarisation (DNP). DNP relies on polarising the electrons in a target material first (atomic polarisation), then transferring the polarisation from the electron to the nucleon. This is possible because the electron is much easier to polarise on account of its greater magnetic moment compared to that of the nucleus, and the transfer of polarisation to the nucleus is achieved by exploiting the hyperfine interaction between the atomic spin, J, and the nuclear spin, I [50].

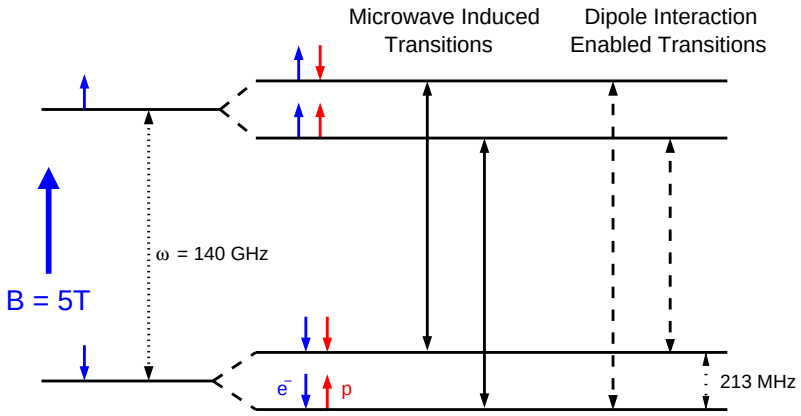

Figure 3.20: Zeeman levels of an electron-nucleon pair in the FROST target. The presence of microwave radiation enables transitions between the spin states of the electron, with the magnetic field allowing the microwaves to induce mutual spin flips of electron and nucleon via the dipole interaction.

The transfer of polarisation occurs under microwave irradiation, which induces spin flips between the electrons and nucleons in the target, with the net result being a build up of nuclei polarised in one particular direction. The simplest mechanism to describe this is known as the resolved solid effect [50, 69].

Figure 3.20 shows the Zeeman levels of an electron-nucleon pair, under the influence of a high magnetic field and microwave radiation at a frequency close to the electron spin resonance. In this simplified system, there are four states, representing the combinations of polarisation states of the electron and proton.

The presence of microwave radiation enables transitions between the polarisation states of the electron, with the dipole interaction enabling the possibility of a mutual spin flip of both the electron and the nucleon. For every nucleon spin flip, multiple electron spin flips occur, and as a consequence of the spin relaxation time of the electron being much shorter than that of the nucleon, the build up of nucleon polarisation is possible if the electron spin flips are sufficiently frequent as to induce enough spin flips in the nucleons to sustain a population of nucleons with a particular spin.

In order to preferentially polarise nucleons in one direction, the microwave frequency is chosen such that the transition between the Zeeman levels resulting in the desired nucleon polarisation state is selected (see figure 3.21).

The resolved solid effect is only a simplified explanation of the DNP process,

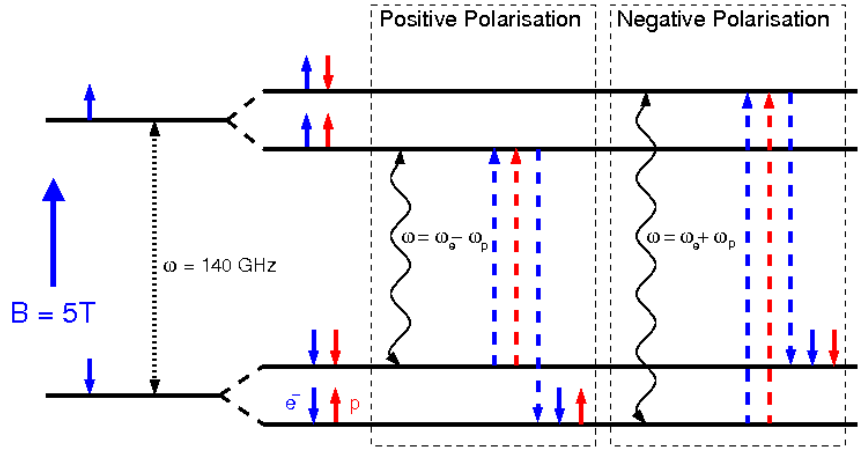

Figure 3.21: Demonstration of the resolved solid effect for an electron-proton pair in the FROST target, showing the selection of positive and negative polarisation states with appropriately tuned microwaves to facilitate a mutual spin flip of a proton and electron. Because the spin relaxation time of the proton is much longer than that of the electron, the electron spin relaxes, leaving the proton in the desired spin state.

as other properties act to complicate this picture. These include the presence of multiple electrons, due to the addition of paramagnetic radicals, which are added to the material to increase the number of free electrons available for spin flipping, impurities in the material, leading to additional paths by which polarisation can relax, and the effects of radiation damage. A fuller consideration of DNP and its underpinning mechanisms can be found in references [50, 70].

3.7.3 The FROST Target

FROST, which stands for FROzen Spin Target, is the name of the polarised proton target designed and built at Jefferson Lab by the lab's Target Group for the g9 experiments [23, 71].

Polarised targets which exploit DNP have been used in Jefferson Lab before [72], however these targets are not suited for use in the FROST experiment. The main reason for this is that these targets operate in continuous polarising mode, where the polarising field and microwaves are continuously applied. The presence of the polarising magnets, and their associated magnetic field, act to reduce the acceptance of CLAS dramatically, obscuring coverage of the backward angles beyond around 55° [30].

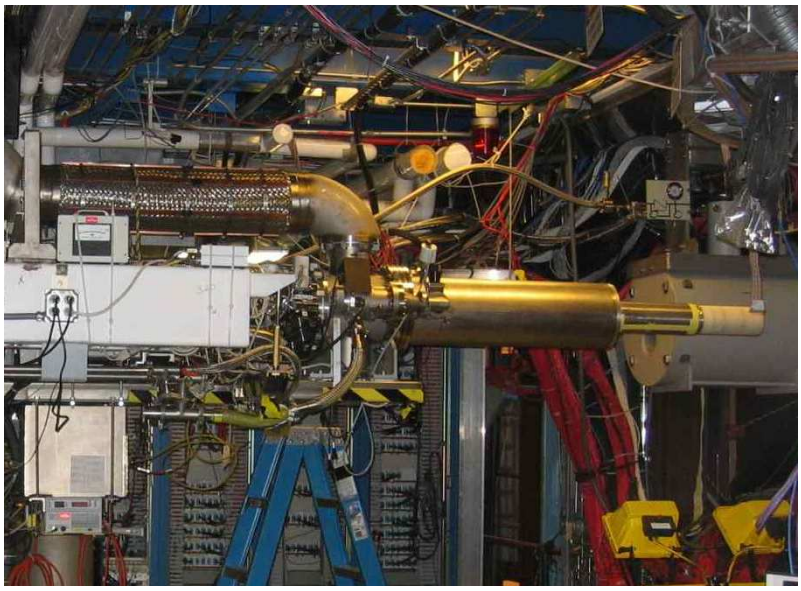

Figure 3.22: The FROST target in Hall B. The target materials are contained in the target holder, at the tip of the target assembly. The polarising magnet can be seen in the background on the right hand side of the image.

In order to exploit the large acceptance of CLAS fully, FROST operates in frozen spin mode. In a frozen spin target, the target is polarised via DNP in the same way as for a continuously polarised target, but at times when data is being taken, the polarising field and microwave radiation are not applied. Because the magnetic field and microwaves are switched off, the polarisation of the target material begins to decay. In order to preserve this polarisation for as long as possible, the target is kept extremely cold, and a weaker holding magnetic field, with smaller coils than the polarising magnet so as not to obscure reaction products from CLAS, is applied.

Figures 3.22, 3.23 and 3.24 show the FROST target. The bulk of the target assembly consists of the cooling and refrigeration systems required to keep the target material cold and preserve the polarisation. This includes a custom built horizontal dilution refrigerator (briefly discussed in the next subsection), magnetic coils to provide the holding field, the microwave generator and its associated waveguide components, precooling cryogenics, various components for monitoring and controlling these systems, and a superconducting magnet to polarise the material.

To polarise FROST, it is removed from CLAS and the end containing the target material is placed inside the polarising magnet, stored near CLAS and away from the Hall B beamline when not in use, where it is exposed to a 5 Tesla magnetic field

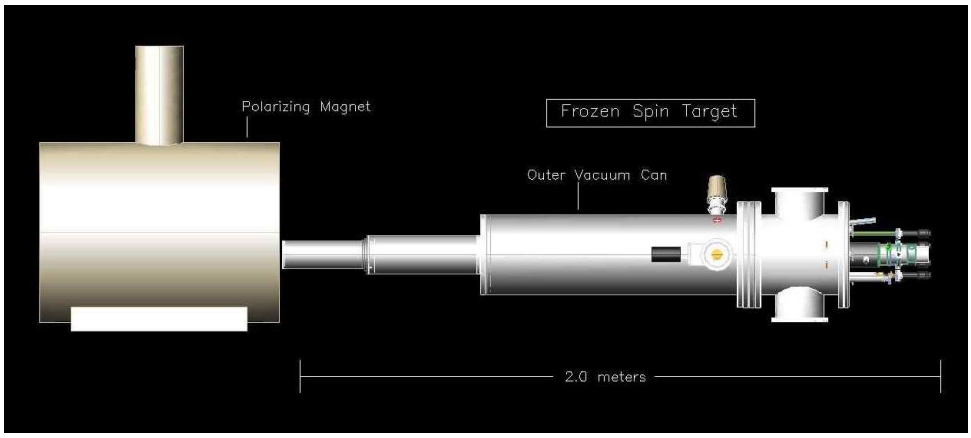

Figure 3.23: Computer generated image of the FROST target and 5 Tesla polarising magnet. Five grams of butanol pellets are contained in the target cell, located at the tip of the target assembly, where a 0.5 Tesla magnetic field acts to maintain target polarisation in conjunction with millikelvin cooling provided by a bespoke horizontal dilution refrigerator.

and 140 GHz microwaves, causing the nuclei in the target to polarise. During this process, the target temperature is maintained at around 300 mK. Once the polarisation reaches its maximum level, around 80%, the magnetic field and microwaves are switched off and the target is cooled further via dilution refrigeration, eventually reaching around 30 mK. During this cooling process, a second holding magnet surrounding the target cell with a lower field, around 0.5 T, is then switched on. This holding field and millikelvin cooling "freezes" the polarisation, which slowly decays over several days, and during this time the target is repositioned inside CLAS and data taken using the tagged photon beam until it needs to be repolarised, a period of 5-7 days during the g9a run. Monitoring of the degree of polarisation of the target is achieved via NMR coils within the target assembly.

The target cell is around 50 mm long and 15 mm in diameter and contains 5 grams of frozen butanol (C_4H_9OH) pellets. Pure molecular hydrogen (H_2) would be the ideal material to use as a proton target, however at the low operating temperatures required, it forms a state with spin zero, and is unpolarisable [50]. In making an alternative choice of material, consideration is taken of the radiation resistance of the material and how much hydrogen it contains. These considerations led to the choice of butanol, doped with paramagnetic radicals by the addition of 0.5% TEMPO (2,2,6,6-Tetramethylpiperidin-1-oxyl) [73], which provides $\sim 10^{19}$ electrons

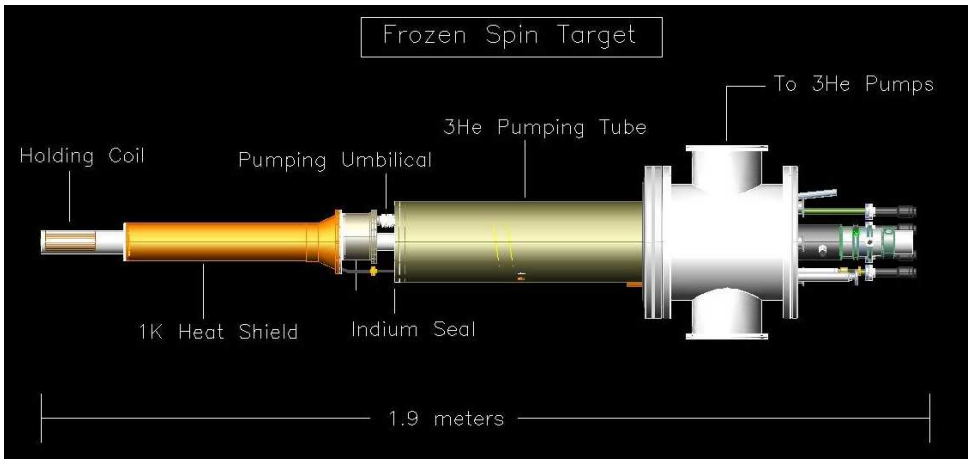

Figure 3.24: Computer generated image of the FROST target, with the outer vacuum can removed to show the 1 K heat shield and the holding coil which surrounds the target material.

per cubic centimetre [71].

Figure 3.25: Longitudinal holding magnetic coil for the FROST target, used in the g9a experiment.

In the g9a experiment, FROST operated in longitudinally polarised mode, i.e. the direction of polarisation was parallel or anti-parallel to the direction of the photon beam. A summary of the target run conditions are given in table 3.2. During the g9a run, the FROST target exceeded many of its design specifications, achieving a target temperature around 30 mK, 20 mK lower than the specification, polarisations

in excess of the expected 80%, the dilution refrigerator delivering far greater cooling power than designed, and polarisation relaxation time between 3 and 5 times longer than expected, depending on polarisation direction.

Target Polarisation Mode	Longitudinal (+/-Z)
Maximum Polarisation Achieved	82% (Positive) 85% (Negative)
Relaxation Time	2700 hours (Positive) 1600 hours (Negative)
Target Temperature (Frozen Spin Mode)	28 mK (no beam) 30 mK (with beam)
Cooling Power	1 mW (Frozen Spin Mode, 50 mK) 80 mW (Polarising, 300 mK)
Field Strength (Polarising Magnet)	5 Tesla
Field Strength (Holding Magnet)	0.5 Tesla
Polarisation Loss (Per Day)	1-2%

Table 3.2: Summary of operating conditions of the FROST target for the g9a experiment

Also included on the FROST target assembly are two unpolarised target foils, carbon and polythene. These are used for studies of the nuclear contribution to the butanol data, quantifying the amount of unpolarised material in the butanol, and verification of previous measurements on unpolarised targets, which will be discussed in chapter 6.

3.7.4 Dilution Refrigeration

Below temperatures of 0.88 K, a ^{3}He/^{4}He liquid helium mixture separates into two separate phases; one rich in ^{3}He (the 'concentrated' phase) and one poor in ^{3}He (the 'diluted' phase) [74] (see figure 3.26). When ^{3}He is removed from the diluted phase, ^{3}He from the concentrated phase crosses the phase separation boundary in order to maintain equilibrium. This absorbs heat from the surroundings and can be exploited for cooling at very low temperatures.

In a dilution refrigerator, this property of a ^{3}He/^{4}He mixture is exploited in order to realise the millikelvin cooling required to help maintain polarisation in the FROST target during data collection. Figure 3.27 shows the basic layout of a dilution refrigerator, and its key components, the mixing chamber, where the lowest

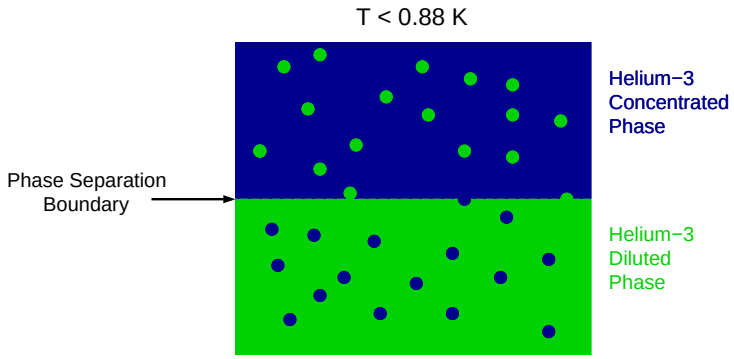

Figure 3.26: Below temperatures of around 0.88 K, a mixture of ^{3}He and ^{4}He separates into two phases, one rich in ^{3}He and one poor in ^{3}He, respectively referred to as the concentrated and diluted phases. When ^{3}He is removed from the diluted phase, ^{3}He from the concentrated phase crosses the phase separation boundary in order to maintain equilibrium. This absorbs heat from the surroundings and can be exploited for cooling at very low temperatures.

temperatures are reached, the distillation chamber, where ^{3}He is removed from the mixture, and the condenser, where the removed ^{3}He is condensed before being reintroduced to the mixing chamber to maintain a continuous cooling cycle.

At the low temperatures required in the mixing chamber, ^{3}He cannot be directly pumped away as the vapour pressure is too low, and so the helium mixture from the dilute phase is pumped to a distillation chamber, which is maintained at a higher temperature. The vapour pressure of ^{3}He here is high enough for it to be pumped out. Following its removal, the ^{3}He is recondensed so it can be reintroduced to the mixing chamber in order to maintain a continuous cooling cycle.

Dilution refrigerators are commercially available, but are oriented vertically (as seen in figure 3.27) and are unsuitable for the FROST target as it would not be able to fit inside CLAS. For this reason, a bespoke horizontal dilution refrigerator was designed and constructed in-house at JLab for use in the FROST target. This refrigerator can be seen in figure 3.28.

3.8 Beamline

The Hall B beamline contains several other pieces of equipment, used to ensure beam quality. Of particular importance for running with the linearly polarised photon beam is the position of the electron beam when it hits the diamond. If the beam

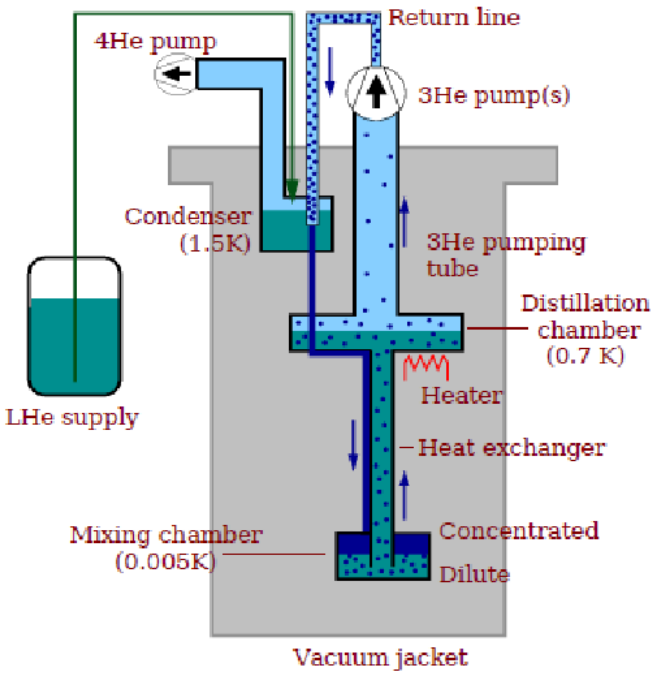

Figure 3.27: Diagram of a vertically-oriented dilution refrigerator, showing the key components [71]. Commercially available dilution refrigerators are oriented in this manner and therefore cannot fit inside CLAS, leading to the development at JLab of a horizontal dilution refrigerator for the FROST target.

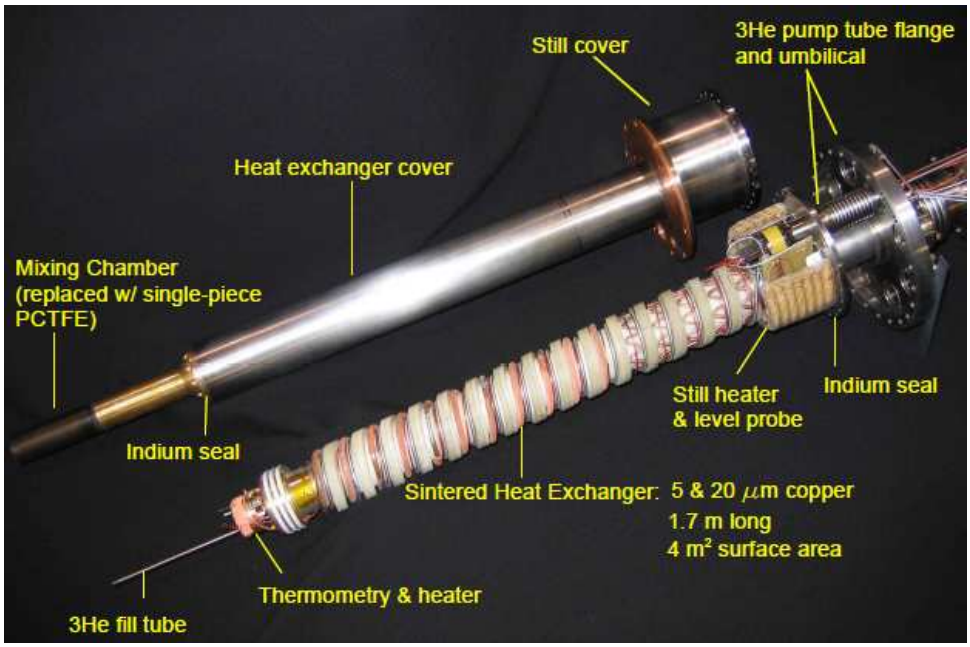

Figure 3.28: The horizontal dilution refrigerator developed at JLab for the FROST target.

is not positioned correctly, or its position is unstable, then this can have a dramatic effect on the degree of polarisation of the resulting photon beam. Monitoring of the electron beam position is realised via the Beam Position Monitors (BPMs). There are three BPMs in the Hall B beamline, located 36, 24.6 and 8.2 m upstream of the CLAS target, designated 2C21A, 2C24A and 2H01A, respectively. The electron beam induces a current in wires adjacent to the beamline, which varies with position, allowing the x and y positions of the beam to be determined. For photon beam running, only the 2C21A and 2C24A BPMs are used, as the 2H01A BPM is located downstream of the photon tagging spectrometer. A representative set of BPM measurements from g9a as shown in figure 3.29.

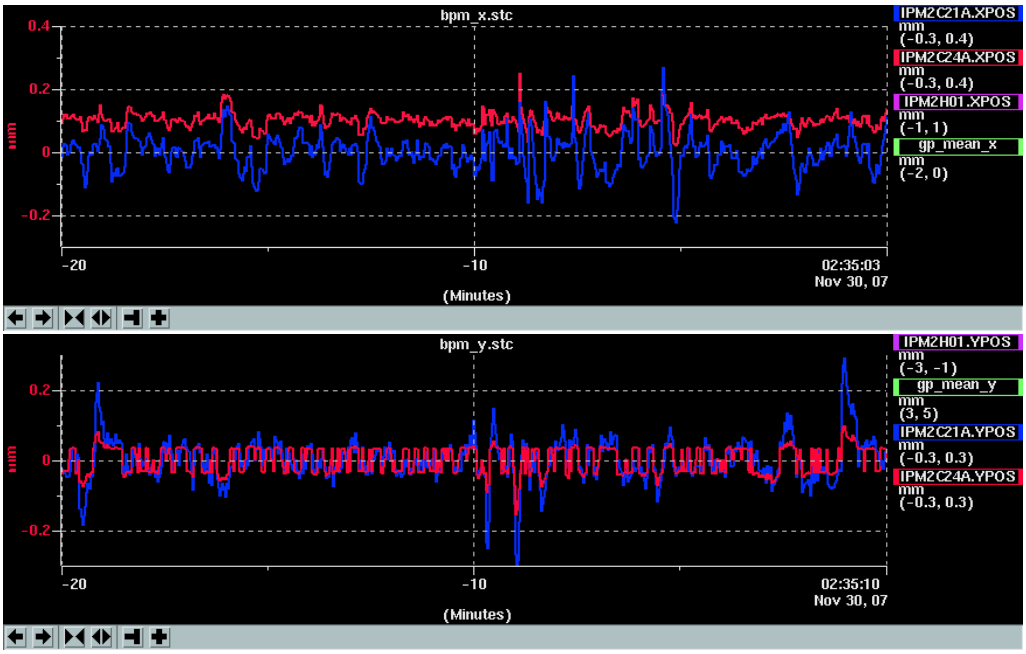

Figure 3.29: Typical beam stripcharts showing x (top) and y (bottom) beam positions, as seen during the g9a run period. 2C21A (blue) and 2C24A (red) are shown, 2H01A is not shown as its location downstream of the tagger mean it is not used in photon experiments.

The total absorption shower counter (TASC) is located downstream of CLAS, and uses four lead glass blocks to determine beamline efficiency. This information allows the measurement of the number of bremsstrahlung photons hitting the target. The TASC can only operate at beam currents up to 100 pA and must be removed from the beamline under normal run conditions, therefore secondary monitors must be cross-calibrated against the TASC at these low currents and used to monitor

photon fluxes at higher currents.

The Pair Spectrometer (PS) is one of these secondary monitoring devices, able to measure photon fluxes at high rates. The operation of the PS is based on the use of a thin conversion foil to produce e^+e^- pairs from the photon beam. These pairs are then swept out of the beamline by a dipole magnet and detected by a set of scintillator paddles.

3.9 Trigger and DAQ

In order to select and read out signals corresponding to events of interest from the various subsystems comprising CLAS, a trigger system is employed. In general, analogue signals for each detector element are split into two branches; one leads to a Charge to Digital Converter (QDC) and the other to a discriminator to produce a logic signal which can be fed to a Time to Digital Converter (TDC) and used as input to the logic circuit which triggers the event readout. In an experiment with many hundreds of detector elements each subsystem (eg. Drift Chambers, TOF) delivers a single logic signal derived from the OR of the logic signals of its constituent elements.

These subsystem pulses provide the inputs to the trigger which makes a decision on whether to accept or reject the event. If an event is rejected, a fast clear is issued, which clears all QDCs and resets all TDCs ready for the next event. For accepted events a TDC common stop (or start, depending on the mode) is issued, and the readout of all TDCs and QDCs by the data acquisition (DAQ) system is initiated.

The system is latched until the readout is complete, and then reset ready to accept another event. Additionally, logic signals from individual elements (or the ORs of groups of elements) are fed to scalers to provide information on raw count rates. These can be displayed in the experimental control room for monitoring and read into the data stream at regular intervals by the DAQ computer (online event reconstruction in CLAS is shown in figure 3.30).

The CLAS trigger comprises two hierarchical levels, 1 and 2, and a trigger supervisor, which can be configured for individual experiments in order to increase the

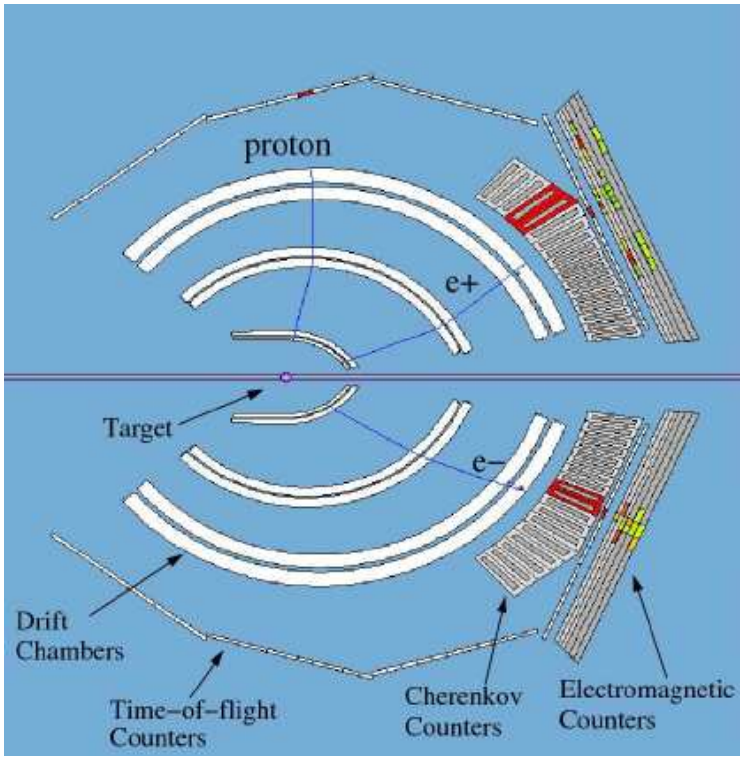

Figure 3.30: Online event reconstruction in CLAS, displayed via the CLAS Event Display system.

proportion of triggers corresponding to events of interest relative to other processes, such as electronic noise or cosmic rays passing through CLAS, which can produce signals that do not correspond to physics events.

The level 1 trigger is intended to rapidly process (within 90 ns) prompt PMT signals through a pipelined memory lookup, in order to determine if an event of interest has occurred. The trigger does this by comparing bit patterns from various detector systems, including the TOF and Cerenkov Counter, with patterns stored in memory tables, looking for potential physics events. Figure 3.31 shows a schematic of the electronics for memory lookup by the level 1 trigger, which combines information from each subsystem for each sector into the level 1 trigger signal.

Depending on the trigger configuration, if an event satisfies the level 1 trigger, the level 2 trigger attempts to find suitable tracks in the drift chambers before declaring the event valid. If the level 2 trigger is not satisfied, a fast clear signal is issued, which clears all the TDCs. Following a level 1 trigger, the level 2 trigger has a period of time known as the fast clear window, around 4 μs, to determine if the

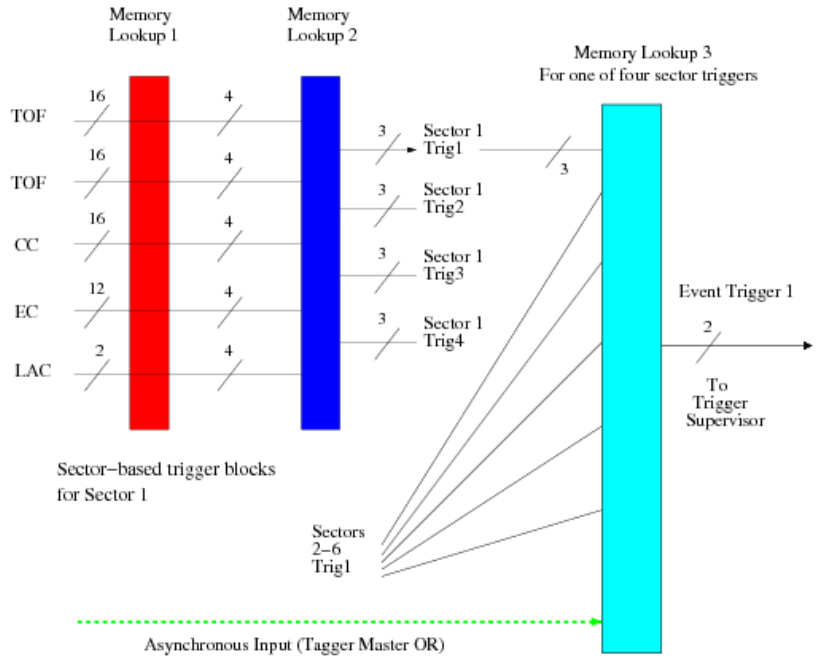

Figure 3.31: Schematic of the memory lookup employed by the level 1 trigger in CLAS. The numbers on the lines to and from each stage of memory lookup indicate the number of bits of trigger data at each stage.

event satisfies the level 2 trigger conditions. The fast clear window is equal to the longest possible drift time in the DC, plus the time required for level 2 processing.

The trigger supervisor produces all common start and stop signals, busy gates, and resets required by the detector electronics. It can be configured to require only a level 1 input, or both level 1 and level 2 signals.

Once the trigger has been satisfied, the readout of the event and conversion into an analysable format can take place. This is achieved by the data acquisition system (DAQ), which uses the CEBAF Online Data Acquisition (CODA) framework.

Data from the various detector systems are digitised, then collected by 24 readout controllers (ROCs). These digitised events are then converted into tables and associated with a unique identity number. The resulting data fragments are then buffered and transferred to the CLAS online acquisition computer (CLON10), located in the Hall B control room. Three main processes occur on the acquisition computer, Event Builder (EB), Event Transport (ET) and Event Recorder (ER). The Event Builder process collates fragments and converts the data into the Bank

Operating System (BOS) format, Event Transport passes the completed events into shared memory on the acquisition computer, where it can be used for online monitoring, reconstruction, or analysis. Finally, the event recorder writes the data to a RAID array, where it is transferred to the JLab tape silo for offline analysis.

3.10 Summary

In the g9a experiment, the high quality electron beam delivered to Hall B from CEBAF is used to produce a polarised photon beam via bremsstrahlung radiation. This photon beam is incident on a longitudinally polarised target positioned in the CLAS detector, and the detector's high acceptance for charged particles is exploited to measure reaction products of various photoproduction reactions, including strangeness channels.

Before analysis can be carried out on the collected data, the detector subsystems must be calibrated to allow the raw data to be converted into meaningful physical values. These processes will be described in the next chapter.

Chapter 4

Data Handling and Calibration

In this chapter, the details of the conditions for the g9a run and the collection of data are described, as well as the processes required to convert the raw data gathered into a format upon which the analysis can be carried out. Over 10 billion events were recorded during the four months of the g9a run period, and are initially stored as the raw signals from the various detector systems comprising CLAS.

Data are reconstructed into a meaningful physical format of values such as particle energy, momentum and timing in a process referred to within the CLAS collaboration as 'cooking', which takes place after the iterative process of calibration of the individual detector systems. In addition to this process, measurements of the photon beam and target polarisations are made so that the effect of these properties on the analysis can be accounted for.

4.1 Run Conditions and Data Collection

Forming one half of the g9 frozen spin target (FROST) experiment at JLab, the g9a run period took data from October 2007 until February 2008, using a longitudinally polarised target, and linearly and circularly polarised photon beams. The g9 experiment aims to use a polarised target in conjunction with polarised photon beams to study several photoproduction reaction channels, including the strangeness channels $K^+\Lambda$, $K^+\Sigma^0$, and $K^0\Sigma^+$ [23], in addition to π and η meson production reactions [25, 24]. The running conditions during the g9a experiment are summarised

in table 4.1.

Running Conditions	Linear and circular photon beam polarisation, longitudinally polarised target
Torus Current	1918 A
Trigger	At least one charged particle in CLAS
Beam Current	10 - 20 nA
Photon Energy Range	0.7 to 2.3 GeV (Linear Polarisation)
Radiator	50 μm Diamond (Linear Polarisation) 10^{-4} radiation length Au (Circular Polarisation)
Targets	Longitudinally Polarised Butanol (C_4H_9OH), Unpolarised Carbon (^{12}C), Unpolarised Polythene (CH_2)
Target Length	52.7 mm (Butanol), 1.49 mm (Carbon), 3.45 mm (Polythene)
Target Diameter	15 mm
Target Magnetic Field	5 T (Polarising) 0.5 T (Holding)
Base Target Temperature	28 mK (no beam) 32 mK (10 nA beam)
Target Polarisation	+82% -85%
Target Relaxation Time	2700 hours (positive polarisation) 1400 hours (negative polarisation)

Table 4.1: Summary of running conditions for the g9a experiment.

CEBAF ran at several electron beam energy settings during g9a, and the beam provided was used to produce linearly and circularly polarised photons of various energies. For the linearly polarised photon beam, nine photon beam energy settings were produced, ranging from 700 MeV to 2.3 GeV, in steps of 200 MeV. These energy settings are shown in figure 4.1. The two lowest energy settings, 0.73 GeV and 0.93 GeV, are not used in this analysis as they are below the energy threshold for hyperon production.

Because of the multiple electron beam energies used, some coherent peak settings contain data from more than one electron energy setting. This results in differing levels of photon polarisation contributing to the overall degree of beam polarisation for each peak setting. Through careful planning and management of the experiment, the data for most peak settings were taken with just one electron energy, only the 1.1 GeV setting contained multiple energies, and this was limited to only two electron

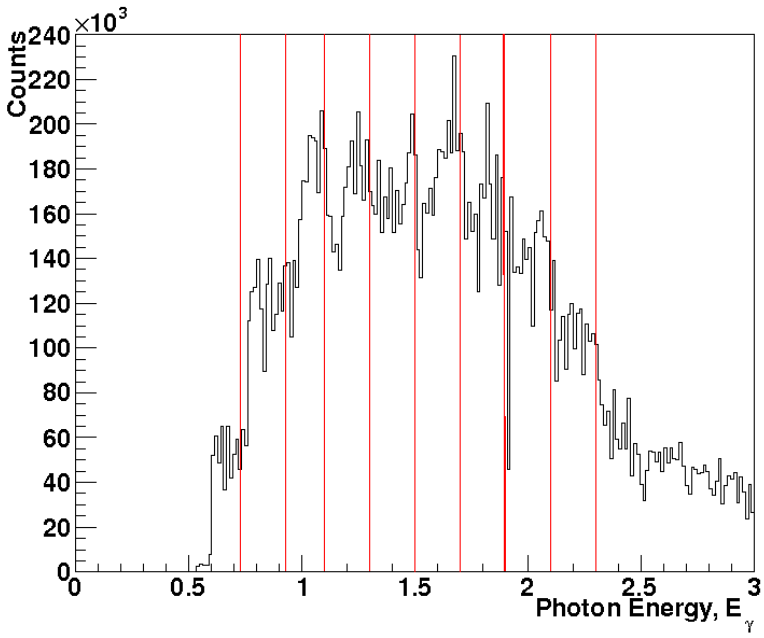

Figure 4.1: Photon energies achieved in the g9a experiment. The red lines indicate the coherent peak settings selected. Due to drift of the coherent peak caused by instability in the CEBAF electron beam, the photon energies produced drift from the desired energy.

energy settings. This can be seen in table 4.2, which summarises the energy settings used in the run, and the number of triggers recorded for each polarisation setting.

The energy bin selection employed for the analysis, which will be discussed in chapter 6, is consistent with the peak settings seen in figure 4.1. However, under this scheme, data from the adjacent peak setting in increasing photon energy will also contribute to the bin, resulting in differing levels of photon polarisation contributing to the energy bin. For most bins, this will only result in two contributing levels of polarisation, with three levels contributing to the bin corresponding to the 1.1 GeV peak setting. The determination of the degree of photon polarisation is described in section 4.5.

The polarisation plane is defined as the orientation of the photon's electric field vector with respect to the horizontal plane of the CLAS co-ordinate system. Two orthogonal settings are required for asymmetry measurements, parallel (PARA), and perpendicular (PERP), which are selected by adjusting the azimuthal orientation of the diamond in the goniometer. When the amorphous radiator is used, the po-

		Positive Target Setting		Negative Target Setting	
$E_e(GeV)$	$E_\gamma(GeV)$	PARA	PERP	PARA	PERP
2.775	0.7	1.21×10^8	1.19×10^8	4.03×10^7	4.01×10^7
2.775	0.9	8.18×10^8	8.10×10^8	1.12×10^8	1.23×10^8
2.775 and 3.539	1.1	7.97×10^7	2.37×10^8	7.95×10^7	1.05×10^8
3.539	1.3	1.21×10^8	1.20×10^8	2.17×10^8	1.63×10^8
3.539	1.5	1.27×10^8	1.62×10^8	1.60×10^8	1.68×10^8
3.539	1.7	8.06×10^7	5.08×10^7	3.65×10^8	3.65×10^8
4.591	1.9	1.27×10^8	1.35×10^8	2.85×10^8	2.21×10^8
4.591	2.1	2.58×10^8	2.53×10^8	2.01×10^8	2.04×10^8
4.591	2.3	2.70×10^8	1.21×10^8	4.10×10^8	1.10×10^8

Table 4.2: Electron and photon beam energy settings for the linearly polarised portion of the g9a experiment, with total triggers for each beam polarisation plane and target polarisation setting. Note that two electron beam settings contribute to the 1.1 GeV photon beam setting.

larisation plane is defined as amorphous (AMO), and the polarisation settings were alternated in the approximate ratio 2:2:1 of PARA, PERP and AMO. In addition to altering the plane of photon polarisation, the direction of polarisation of the target is also altered. With respect to the direction of the incoming beam, the target polarisation is altered between parallel and anti-parallel, referred to as the positive and negative target settings, respectively. The target polarisation direction was changed roughly once per week, and was done when repolarising the target, with the intention of allowing approximately equal amounts of PARA and PERP data to be collected for each target polarisation setting. There are four combinations of beam and target polarisation, and their mean values for each photon beam energy setting are shown in table 4.3.

$E_\gamma(GeV)$	PARA	PERP	Positive Target Setting	Negative Target Setting
1.1	0.45	0.52	0.89	0.78
1.3	0.53	0.55	0.87	0.78
1.5	0.49	0.52	0.86	0.78
1.7	0.46	0.49	0.84	0.79
1.9	0.41	0.39	0.84	0.80
2.1	0.50	0.47	0.85	0.77
2.3	0.59	0.64	0.89	0.80

Table 4.3: Mean polarisations of beam and target for the linearly polarised photon portion of the g9a experiment.

4.2 Data Reconstruction

Like most experiments, raw data from CLAS experimental runs are collected in the form of files containing channel ID and values for the QDCs and TDCs of the various detector systems. These must be converted into physical quantities in a process referred to as 'cooking', a time-consuming process in which particle tracks and momenta are reconstructed from the raw data. The detector subsystems must also be calibrated, before analysis of the data can be carried out.

The raw data from the CLAS subsystems are stored on an event-by-event basis within a dynamic memory structure known as Bank Operating System (BOS). In this structure, each CLAS subsystem has at least one associated 'bank', which contains the raw output of the detector. These banks can be accessed individually as required by functions developed for the cooking or calibration processes. The raw BOS files are named according to run number, and split into a number of 2 GB files depending on the length of the run. A typical run in g9a would collect roughly 20 million events, which corresponds to around 30 data files per run. In total, the g9a experimental run period took data for around 650 runs, including several dozen calibration and commissioning runs, taken while the experimental equipment in Hall B was set up and adjusted at the start of the run period, and a number of "junk" runs, which cannot be used for a variety of reasons, such as failure of the data acquisition system during the run, resulting in no data being written to file, or the run was taken during repairs or changes to equipment, and served only as a test of the work carried out.

4.3 Subsystem Calibrations

Calibrations are performed in an iterative manner of the subsystems of CLAS, at first on a small subset of the data, with improvements to the calibration of one system allowing further improvements to be made to the others. Once an adequate set of calibrations has been performed, they are applied to the whole dataset and the cooking process can take place, converting raw BOS data for each detector system into physical quantities, such as particle ID, position, angles, energy, time, etc.,

which are output in the form of cooked BOS files. The calibrations performed on the data are summarised below.

4.3.1 Start Counter

As discussed in the previous chapter, the start counter is of great importance to photonuclear experiments in Hall B, initiating the level 1 trigger and providing timing information on the hadronic interaction which enables the appropriate beam bucket for an event to be identified. In order to do this, the start counter must be suitably calibrated. This is done in two main stages, first the timings of the paddles in the start counter (24 in total) are aligned with respect to each other, then the start counter time (the time of a hit in the start counter) is adjusted relative to the tagger time (the time of a hit in a tagger T-counter, itself separately calibrated as described in the next subsection). Figure 4.2 shows various calibration plots for the start counter, before and after calibration.

The final stage of the start counter calibration involves alignment with the time-of-flight (TOF) system by subtraction of the vertex time from the TOF from the start counter vertex time. The distribution of these times is then aligned to zero.

4.3.2 Tagger

Calibrating the tagger involves converting the E-counter and T-counter TDC values from the PMTs into times by computing calibration constants for each TDC. This allows geometrical matching between hits in the E-counter and overlapping T-counters. Final timing is taken from the T-counters, corrected individually for offsets, to identify the correct beam bucket. Fine corrections to this timing come from the machine RF time.

Each T-counter has two TDCs, left and right, for which times are calculated and compared. These are then corrected relative to each other and the RF time on a counter-by-counter basis. Because the TDCs operate in a so-called common-start self-triggered mode, a T-counter hit can start a time measurement. In such a case, either the left or right TDC will register the first time and become the trigger, so

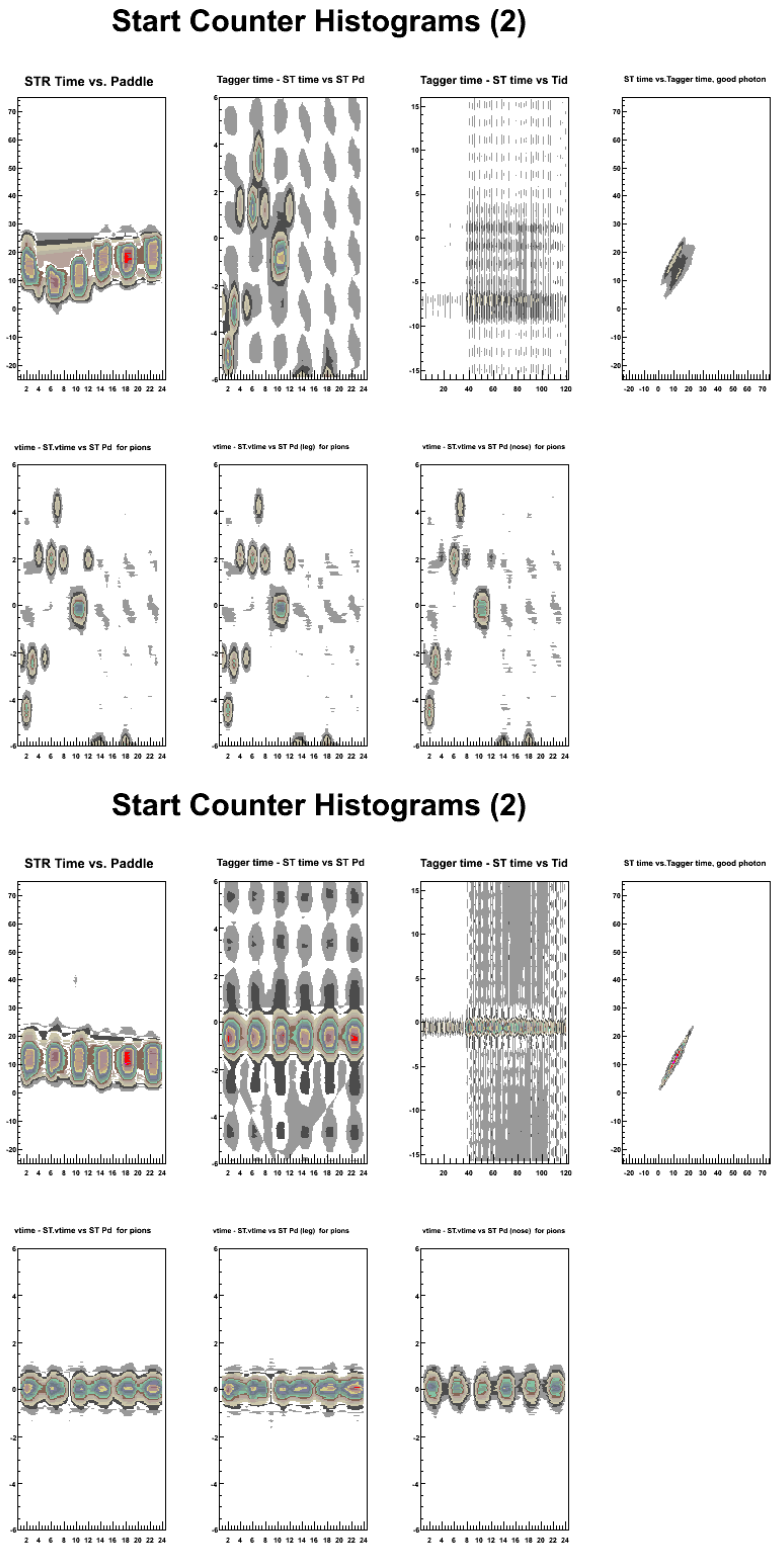

Figure 4.2: Start counter plots, before and after calibration. The top row shows (L-R) start counter time vs paddle number, difference between tagger and start counter times vs paddle number, the difference between tagger and start counter times vs T-counter, and start counter time vs tagger time. The bottom row shows start counter time vs paddle number for pion events, normalised to the vertex time for the whole length of the paddle, the "leg" section, and the "nose" section. Calibrated plots show several distributions aligned around zero, indicating a well calibrated run.

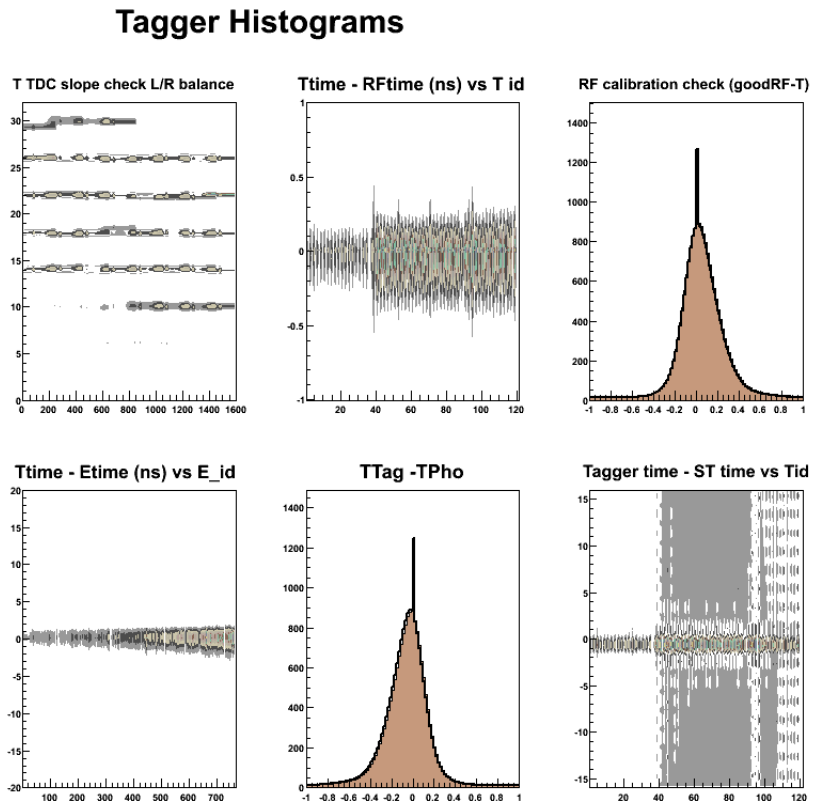

Figure 4.3: Tagger calibration plots. Note the alignment of several of the plots on zero, indicating a well calibrated run.

further corrections are performed to account for signal delay between the left and right TDCs.

The correct RF beam bucket is then identified from the RF time, which is given relative to the trigger time. This requires the determination of calibration constants for each T-counter, first using the start counter as a reference time, then accounting for the RF phase shift in the T-counter, enabling the beam bucket offset to be determined on an event-by-event basis. This procedure results in the calculation of two times which can be used in analysis, the tagger time reconstructed on an event-by-event basis, and the RF bucket real time, which is considered to be the actual photon time.

The time it takes a photon to reach the centre of the CLAS target should be the time associated with a tagged photon. This is relative to the CLAS detector subsystems and, since the RF timing and T-counter signals are independent of each other, this tagger to TOF offset can be be defined in a similar manner as the start

counter to TOF offset.

4.3.3 Drift Chambers

Calibration of the drift chamber is necessary in order to reconstruct particle tracks in CLAS. These paths are reconstructed from measurements of particle positions within the drift chamber cells. Track reconstruction is performed in two stages, Hit Based Tracking (HBT) and Time Based Tracking (TBT).

Hit Based Tracking is based upon a least squares fit of a track to hit wire position, and is performed when three superlayers register a hit. The resulting track segments are then linked across all the superlayers and regions in order to reconstruct a track.

Time Based Tracking requires the measurement of the drift time, using information on the particle flight time from target to the time of flight scintillators. These drift times can then be converted into distances within the drift chamber cells and fitted within the cells to determine the track.

4.3.4 TOF

At this point, the start counter, tagger and time of flight timings are aligned relative to each other. This timing alignment underpins the identification of particles in CLAS and their association with events. The TOF also plays an important role in the particle identification process by determining the quality of the charged particle identification and the mass resolution.

First the status of each scintillator paddle is flagged for any reconstruction problems, such as no ADC or TDC, and pulser runs used to measure the ADC pedestals; these runs are also used to calibrate the TDCs. Laser runs are used to calibrate for the dependence of the trigger time on the signal peak height of the triggering signal.

By aligning the left and right PMTs and determining left-right time offsets, the hit position within a scintillator can be determined and the hit positions from each TDC can be plotted for each scintillator on a sector by sector basis. These sector based distributions should be symmetric around zero.

To account for attenuation length of the scintillator the relation between the

amount of light arriving at each PMT and the hit position along the scintillator is determined. To do this, the geometric mean of the left and right ADC values for a minimum ionising particle is measured and normalised so that the pulse heights for a minimum ionising particle normally incident at the centre of the scintillator is equivalent to 10 MeV.

The effective velocity of light in the scintillator must then be calibrated for each counter using hit position information and the difference between the left and right timings. Finally, the paddle to paddle delay alignment sees the timing for each scintillator aligned with the start counter and photon tagger.

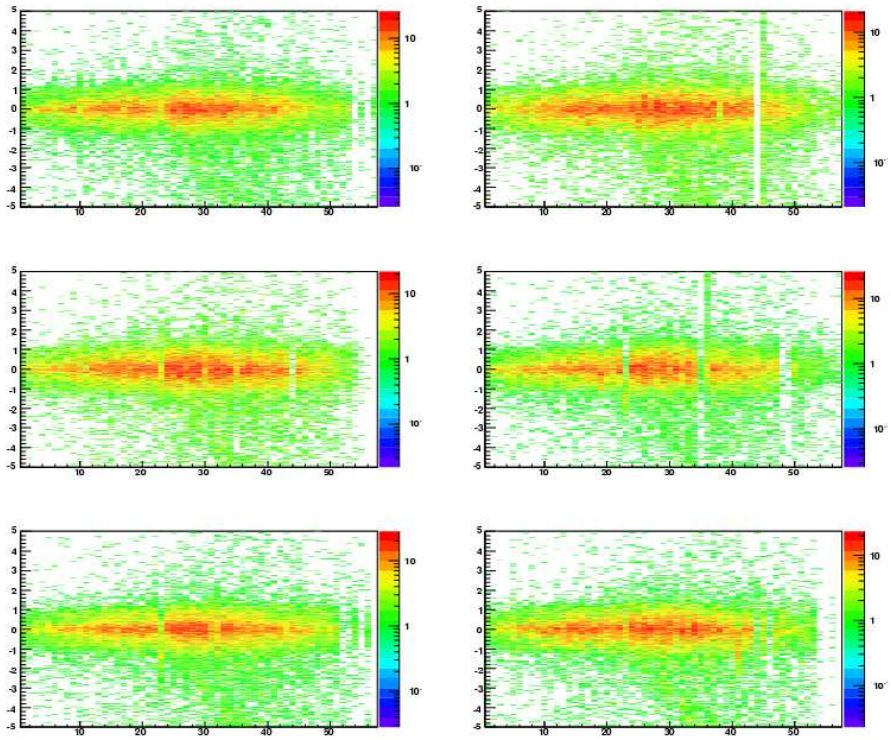

Figure 4.4: Paddle-to-paddle delay between the timing from the TOF scintillators and the start counter/photon tagger, shown for each sector in CLAS. The plots show timing difference between the time of flight and vertex times, plotted against TOF paddle number. The gaps in the distributions indicate faulty TOF paddles, and are not used to reconstruct data. Offsets are calculated such that the peak of each scintillator's timing distribution is centred on zero.

4.3.5 Electromagnetic Calorimeters

The principle behind the calibration of the electromagnetic calorimeters (the forward electromagnetic calorimeter and the large angle calorimeter) is to find an agreement between the vertex time as measured by the EC and that measured by the TOF. A distribution of the differences between these two times should be centred on zero. The EC time is required for neutron/photon discrimination in CLAS as it is the measurement of the particle velocity that enables identification, although this calibration is less important for the analysis presented in this thesis as the detection of photons or neutrons is not required.

4.4 Data Skimming

The entire cooked g9a data comprises several thousand files, and is several terabytes in size, requiring not insignificant resources for storage. This data was accumulated for the analysis of various reaction channels [23, 24, 25], and as a result of the loose trigger conditions employed to accept events for all these channels, the resulting data is dominated by events corresponding to other channels. This leads to longer runtime of analysis code, as events of interest must be selected from thousands of events which correspond to other channels.

In order to manage the data better, and shorten the runtime of analysis code, the data is reduced in size by a process called skimming. Two skims were performed to produce the files used in the final analysis, the first skim takes the cooked BOS files and selects events containing a candidate kaon, which would allow reconstruction of the reactions of interest, and outputs a DST (Data Summary Tape) file. The resulting DST files are much smaller than the cooked BOS files they were created from, having discarded events which do not correspond to potential $K^+\Lambda$ or $K^+\Sigma$ reactions. A second skim was performed only on the skimmed linearly polarised data, as the circularly polarised data was not used in this analysis. This skim realises further data reduction by removing banks not used in the analysis, and reduces the number of files by combining the much smaller skimmed data files into a single file for each run. After these skims have been performed, the data comprises

419 files, and requires a total of 255 Gigabytes of storage.

4.5 Photon Polarisation

In order to measure the degree of photon polarisation, the position of the coherent edge and the relationship between photon energy and polarisation for the edge positions must be known. The position of the coherent edge is found by taking an enhancement plot of the tagger scaler spectrum, formed by dividing the polarised photon spectrum by the amorphous distribution, as shown in figure 4.5. The coherent edge is defined to be the steepest negative gradient of the trailing edge of the peak on the enhancement.

When the coherent edge has been found from the enhancement, it is compared to an analytic bremsstrahlung (ANB) calculation [75]. This enables properties such as beam diversion and beam spot size to be accounted for, and the adjustment of several parameters relevant to the degree of photon polarisation. Once a good agreement is reached between the data and the calculation, a set of polarisation lookup tables are generated. This is performed for each coherent peak setting and polarisation plane, and in the case of the 1.1 GeV peak setting, for each electron energy setting for that peak setting.

With the values of photon polarisation now known, the weighted mean values for each plane setting for each energy bin can be found. This requires the mean photon polarisations for the planes to be calculated for each contributing polarisation table, with the final value for the bin calculated from the weighted mean of these values.

Systematic uncertainty in the measurement of photon polarisation with the ANB method arises from several sources. These include a combination of the curvature and quality of the diamond radiator and small drifts in the angle of the incident electron beam. These drifts in beam angle cause the coherent peak to drift away from its nominal position.

The polarisation tables used in this analysis are based on an average position of the coherent peak, resulting in a systematic error of 10%. A more sophisticated, event-by-event analysis of the beam polarisation is currently underway, and is ex-

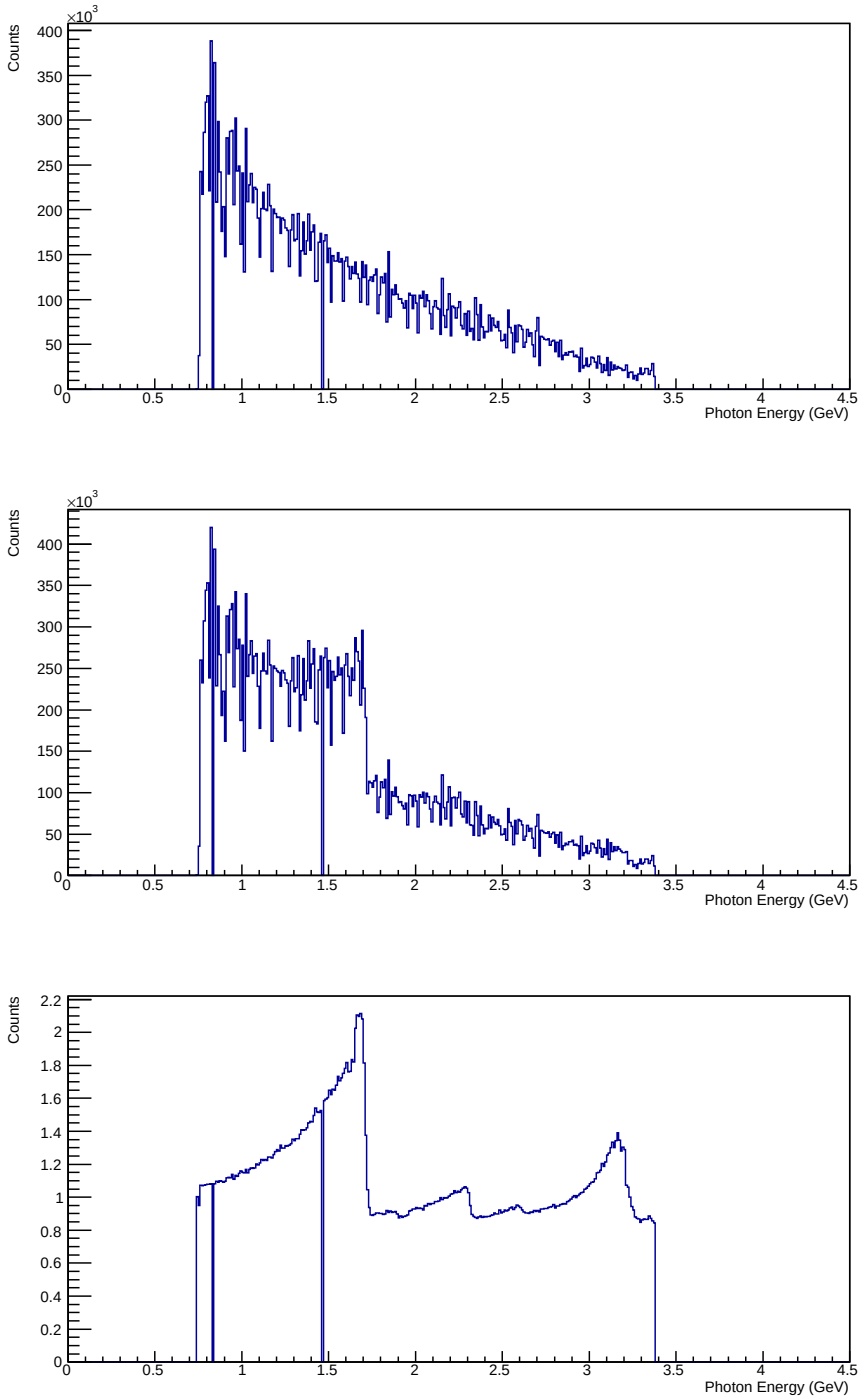

Figure 4.5: (top) incoherent bremsstrahlung spectrum for photons produced by electrons from the CEBAF beam incident on an amorphous radiator, showing a spectrum which falls off with increasing photon energy. (middle) coherent bremsstrahlung spectrum from a diamond radiator demonstrating the characteristic "coherent peak" structure. (bottom) enhancement plot made dividing the coherent and incoherent spectra.

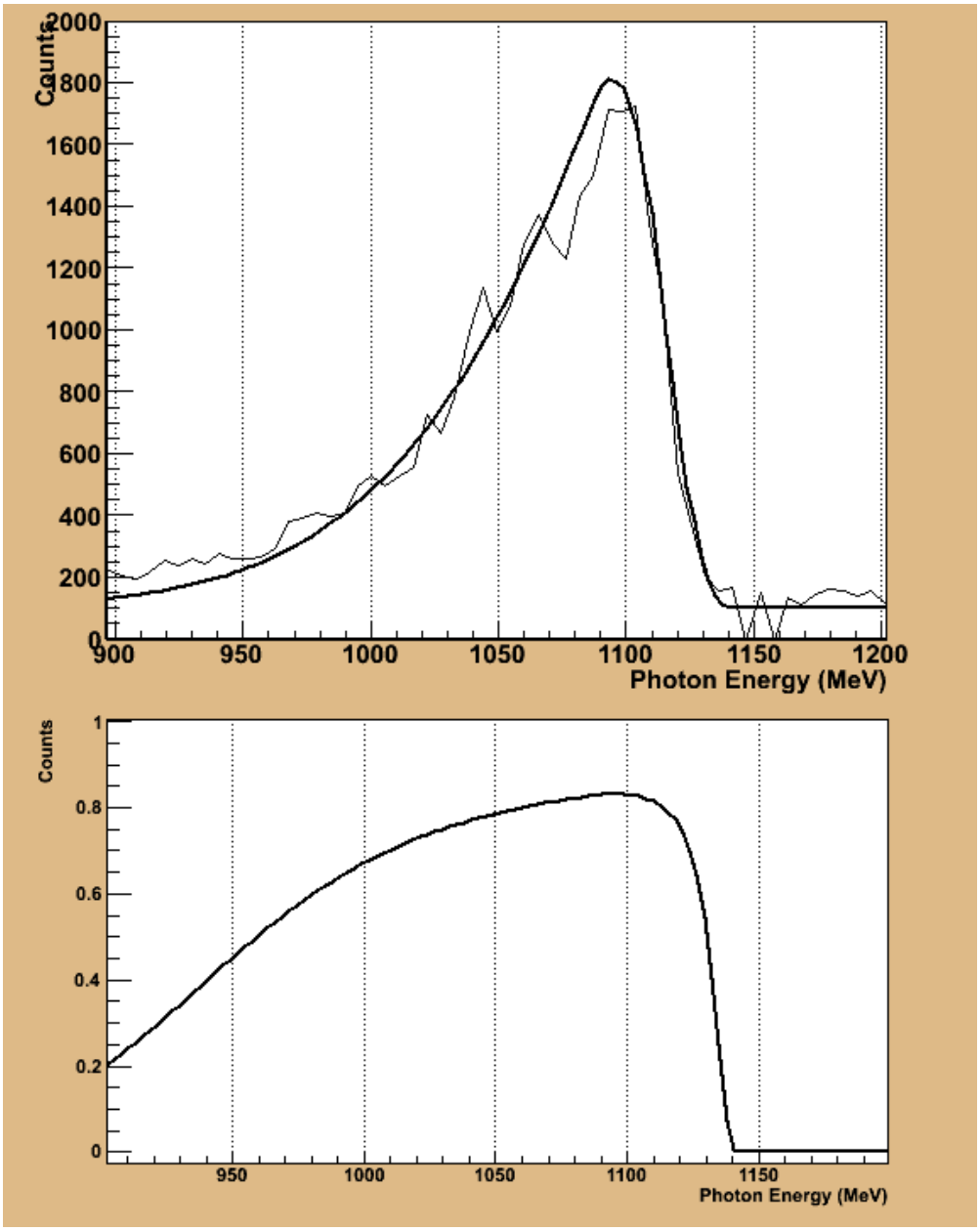

Figure 4.6: (Top) Collimated tagger spectrum compared with the Analytic bremsstrahlung (ANB) calculation for a sample run from g9a (photon energy = 1.1 GeV). (Bottom) Calculated photon polarisation versus photon energy.

pected to bring the systematic uncertainty down to ∼3% [76].

Due to the limitations of this technique, the polarisation measurements for g9a are considered unreliable outwith the range $peak\ energy - 200MeV < photon\ energy < peak\ energy + 100MeV$ [76]. This restriction forms the justification for the photon energy cut applied in the analysis and discussed in the next chapter.

4.6 Target Polarisation

In addition to measurements of photon beam polarisation, knowledge of the degree of target polarisation is required to extract the G polarisation observable from asymmetry measurements on the polarised target data.

This is achieved via the NMR coils integrated into the FROST target, described in the previous chapter. While the target is being polarised, the high-field coils are used to perform an NMR measurement every few minutes, with the low-field coils used for NMR measurements in frozen spin mode, made every 30 minutes. These measurements are of the voltage induced in the coil by the absorption and re-emission of RF radiation at a range of frequencies around the Larmor frequency of the protons in the target.

To convert these NMR measurements into a value of target polarisation, the coils must be calibrated. First, the high-field coils are calibrated for the polarising mode of target operation, where the conditions of thermal equilibrium between target material and the target cryogenics mean that polarisation can be calculated from Boltzmann statistics. This allows measurements from the high-field coils to be calibrated against the known values of polarisation.

The low-field coils are then calibrated by using polarisation measurements from the calibrated high-field coils taken just before and after operation of the target in frozen spin mode. The target polarisation at this changeover from polarising mode to frozen spin mode will be roughly the same, so the polarisation measurement with the high-field coils can be used to calibrate the low-field coils in a similar manner to the initial calibration of the high-field coils to the calculated polarisation from Boltzmann statistics.

The calibrated NMR measurements are then used to define a value of target polarisation for each run, and weighted mean target polarisation values can be determined for each bin just as they were for beam polarisation. As the rate of depolarisation is low (less than 2% per day), this value can be assumed to be constant for the duration of a run (typically 2 hours to collect 20 million triggers).

Key sources of uncertainty in this measurement of target polarisation include contamination of the target material with other materials containing molecular protons, changes in the properties of the circuitry associated with the NMR coils as temperature changes between polarising and frozen spin modes, systematic uncertainties in the measurement of target temperature, and varying sensitivity of the NMR coils along the length of the target. These effects were considered during the determination of target polarisation and an error in the target polarisation for each run has been calculated [77].

4.7 Summary

Once the calibration process is finished, the data can be used for physics analysis, with the option of skimming the data in order to pre-select candidate $K^+\Lambda$ and $K^+\Sigma$ events by preliminary identification of events containing a Kaon in the final state. This enables the size and number of data files to be greatly reduced, allowing more efficient use of computing resources in the analysis. The analysis presented in this thesis was carried out using the ROOTBEER analysis package [78], a ROOT-based [79] software framework designed for ease of handling of the BOS and DST file formats used for cooked and skimmed CLAS data files.

The data are used to construct particle 4-vectors from initial particle identification, and these 4-vectors are used for the selection and analysis of events of interest. These processes are described in the next chapter.

Chapter 5

Analysis: Event Selection

This chapter describes the details of the process followed to identify the $\gamma p \rightarrow K^+\Lambda^0 \rightarrow K^+p\pi^-$, and $\gamma p \rightarrow K^+\Sigma^0 \rightarrow K^+\Lambda^0\gamma \rightarrow K^+p\pi^-\gamma$ reactions from the g9a data. This process has been split two parts; particle identification, where candidate particles for the reactions of interest are selected from the skimmed data, and channel identification, where these events are separated according to their corresponding reaction channel.

The chapter follows this process for the centre of mass energy range, W = 1.87 - 1.97 GeV, roughly corresponding to the 1.5 GeV coherent peak setting on photon energy, but the same procedures are carried out for each of the energy settings settings and the cuts applied are tabulated at the end of the particle and channel identification sections.

5.1 Particle Identification

The first stage of the analysis process involves the identification of particles detected in CLAS which may have been produced by an event of interest. The two reactions studied, $\gamma p \rightarrow K^+\Lambda^0$ and $\gamma p \rightarrow K^+\Sigma^0$, have similar final states detected in CLAS, with the Sigma decaying to a Lambda plus a photon, and the Lambda further decaying to $p\pi^-$, as it would for the $K^+\Lambda$ channel.

5.1.1 Hit Multiplicity Cut

The first cut to be applied is on hit multiplicity, or the number of particles detected in CLAS for a given event. Events are retained which have 2, 3 or 4 particles in the final state, in addition to a valid hit in the tagger. As discussed above, the channels of interest have well-defined final states, of three and four particles for the Lambda and Sigma channels respectively, which defined the upper limit on particle multiplicity. The lower limit is determined by the requirement to be able to reliably reconstruct events of interest from non-exclusive detection of the final state particles.

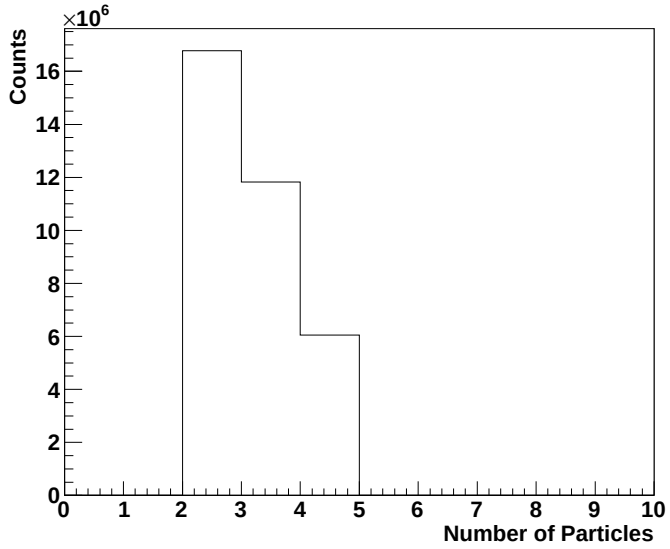

Figure 5.1: Hit multiplicity of events in CLAS. Events with 2, 3, or 4 particles in the final state are retained.

Non-exclusive particle detection was used in this analysis, because of the low probability of detecting a photon in CLAS, the lower acceptance for the negatively charged pion (as a result of the torus field setting used), and the limited amount of data for g9a compared to other CLAS photon beam experiments. The reconstruction of the reactions of interest from these non-exclusive events is discussed later in this chapter.

5.1.2 TOF Mass Cut

Following the hit multiplicity cut, identification of candidate particles is carried out. This was achieved via a combination of the information on charge and mass

provided by the drift chambers and time of flight system. By defining a series of TOF mass windows for positive and negative charged particles, candidate particles can be identified. The selection criteria for particle identification were as follows;

- All particles with non-zero mass and zero charge were removed
- Charged particles with charge greater than one unit were removed
- All particles of non-zero charge must have a valid hit in the drift chamber and either TOF or Electromagnetic Calorimeter
- For positive charged particles the TOF mass windows used were;
  $0.1 < M^2 < 0.49 GeV^2/c^4$ was a K^+
  $0.49 < M^2 < 1.44 GeV^2/c^4$ was a proton
- For negative charged particles the following TOF mass window was used;
  $0.0 < M^2 < 0.1 GeV^2/c^4$ was a π^-

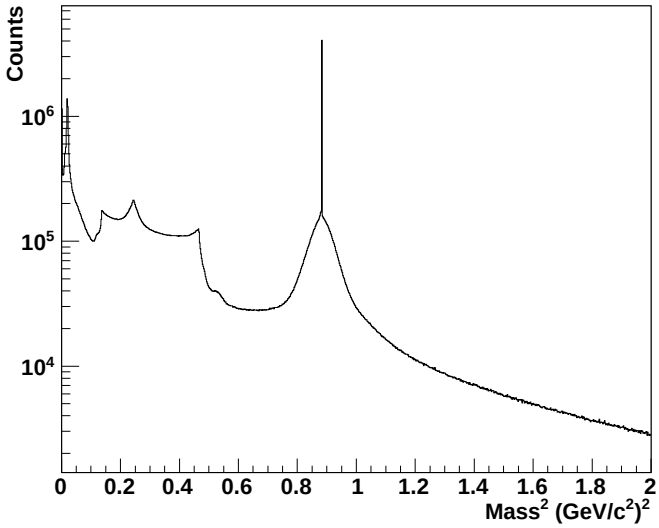

Figure 5.2: Time of flight mass for events in CLAS after the hit multiplicity cut to select events with 2, 3 or 4 particles in the final state. Candidate particles are selected by a combination of charge and a cut on the TOF mass. The spike on top of the peak at mass squared $\sim$0.9 GeV^2 is the mass assigned to neutral particles in CLAS.

Following this initial particle identification, event selection is carried out for the channels of interest. Events must contain a proton and kaon, in addition to zero

or one pions and zero or one neutral particle (to allow the possibility of detecting the photon, although its energy is below the photon detection threshold in CLAS). The possibility of detecting the pion is retained, although it is not required for reconstruction of the Λ or Σ hyperons.

As can be seen in figure 5.2, particle identification from the TOF mass windows is only a first step, as significant backgrounds from mis-identified particles are present. Of particular concern is the identification of the kaon, as kaon-pion separation is a known difficulty in CLAS analyses. Due to the initial skim to select candidate kaon events described in chapter 4, the kaon TOF mass window seen in figure 5.2 shows an enhancement over the other regions, as well as large contributions under the kaon peak from the neighbouring pion and proton peaks. This issue will be considered and addressed by the channel identification cuts described in section 5.3.

5.1.3 Vertex Cuts

As described in chapter 3, the FROST target contains unpolarised carbon and polythene targets, in addition to the polarised butanol, used for studies of the nuclear contribution to the butanol data, quantifying the amount of unpolarised material in the butanol, and verifying previous measurements on unpolarised targets.

The proton is the particle best identified by CLAS, and its vertex position is normally used to cut on the target geometry, but for the reactions of interest in this analysis, the proton originates from a decaying Λ and is not a good indicator of the true position of an event. This is because its vertex will be displaced by the distance travelled by the Λ before it decays. The kaon is instead used for target selection as its vertex position is a more accurate indicator of the origin of an event. The kaon is also used because the event selection criteria do not require the detection of a pion, which could be used with the proton to reconstruct the Λ vertex.

Figure 5.3 shows the z-vertex position of the kaon, which will be used to select events from each of the targets after further particle and channel identification cuts, discussed in the following sections, to improve the separation of the targets, particularly the butanol and carbon targets, which at this stage are difficult to resolve. Initially, a loose cut on the region of the entire FROST target is applied, from -20

to 30 cm, since most of the candidate kaons at this stage are misidentified pions.

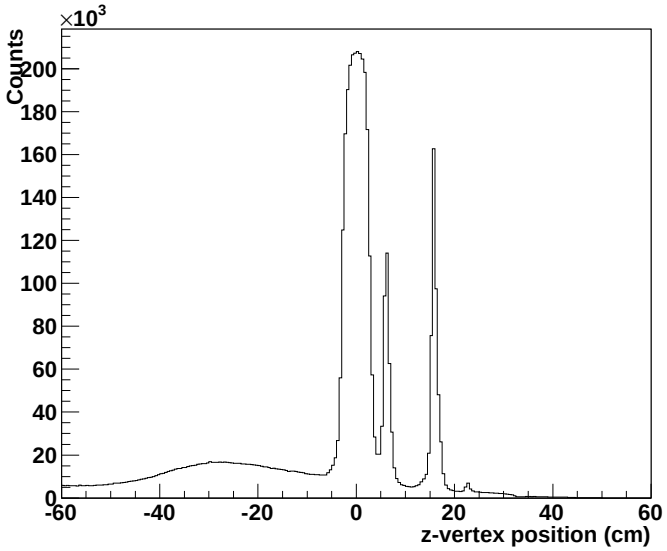

Figure 5.3: Z vertex distribution for candidate kaon events, showing the rough target geometry, consisting of the three target materials in the FROST target (from left to right); butanol, carbon and polythene. Note the poor separation of the butanol and carbon targets and the large background outwith the target. Subsequent cuts will act to improve the separation of the targets and reduce background.

5.1.4 Minimum Momentum Cut

At this stage, a cut was made on the minimum momentum of candidate protons, corresponding to the minimum momentum for detection of particles in CLAS of 300 MeV.

For pions, this minimum detection momentum is 100 MeV, although no cut is applied as the detected pion is not used in the non-exclusive analysis presented in this thesis for the $K^+\Lambda$ and $K^+\Sigma$ reactions.

5.1.5 Photon Energy Cut

As discussed in the previous chapter, the calculated values of the photon polarisation are unreliable beyond the range of $\textit{peak energy} - 200MeV < \textit{photon energy} < \textit{peak energy} + 100MeV$. For this reason, a cut is performed on the photon energy in this range surrounding the coherent peak energy.

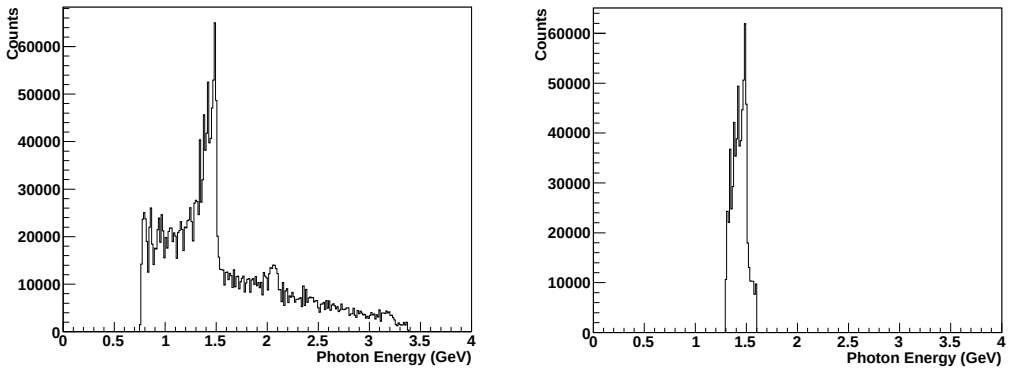

Figure 5.4: Photon energy for the 1.5 GeV coherent peak setting before (left) and after (right) the photon energy cut.

5.1.6 Photon Selection

In order to determine the time at which an event took place, photons are matched to the particle vertex times provided by the TOF. First of all, the timing information provided by the TOF for charged particles is extrapolated backwards to determine when the event occurred, by subtracting the estimated time of flight of a particle (its path length to the TOF divided by its velocity) from the time measured at the TOF. This time is compared with the time provided by the photon tagger; if the TOF and tagger are well calibrated, these times will be the same.

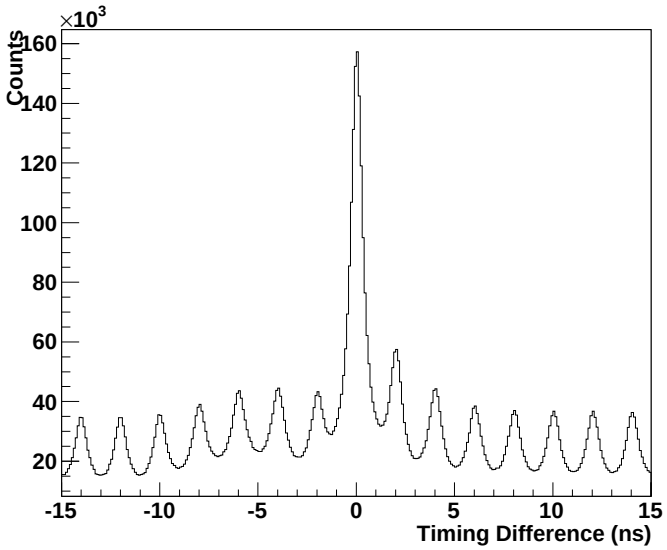

Figure 5.5: Proton timing difference between reverse-extrapolated time-of-flight vertex time and photon time measured by the tagger. The characteristic 2 ns beam "bucket" structure can be seen.

Figure 5.5 shows the timing difference between proton vertex time and the time measured by the tagger, with the peak centred on zero confirming that the TOF and tagger times are largely the same. The figure also shows the characteristic 2 ns beam bucket structure arising from the manner in which CEBAF delivers beam to the hall (see chapter 3). Photons in these other beam buckets occur because of miscorrelation between a detected particle and a random photon. A slight asymmetry can also be seen in the timing distribution, arising from the dependence of the proton vertex time on momentum.

For many events, there will be more than one photon recorded by the tagger. To find the photon corresponding to the event, the time difference between the photon and vertex times is minimised, to determine the "best" photon. This is done for both the proton and the kaon.

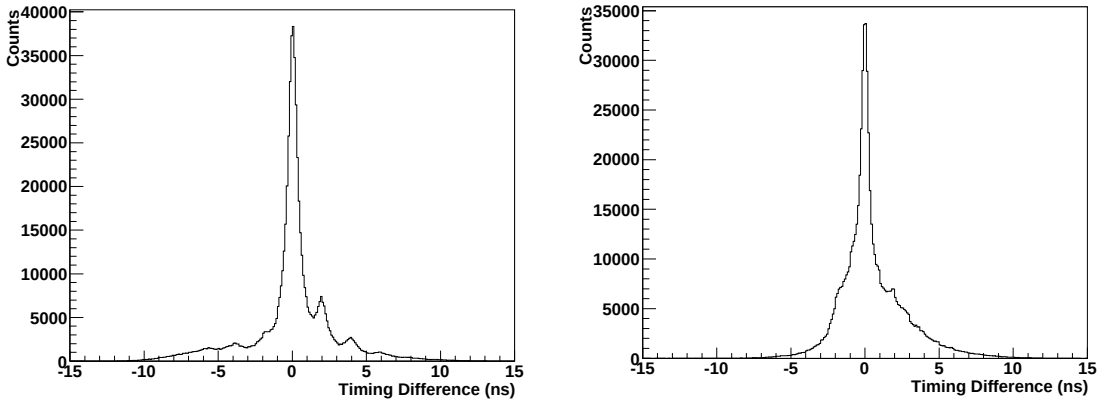

Figure 5.6: (left) Proton vertex time after photon selection. (right) Kaon vertex time after photon selection. The asymmetric structures in these peaks will be dealt with by the momentum dependent timing cuts described in section 5.1.7.

Both the proton and kaon should have the same best photon, and events where this is not the case are removed from the analysis. Figure 5.6, shows the timing difference for the best photon associated with protons and kaons. The asymmetric natures of these distributions arise from particle misidentification and a momentum dependence in the timing difference between TOF and tagger. In the case of the proton, an additional effect comes from the detected proton originating from a hyperon decay. The hyperon produced at the target will have time to move before decaying, meaning that the reverse-extrapolated path of the proton will not originate in the

target, causing a different time to the tagger time to be estimated by the TOF.

5.1.7 Momentum Dependent Timing Cuts

To remove events with poor timing; i.e. those where the timing difference between the TOF and tagger for a proton or kaon is significantly non-zero, a series of timing cuts are applied. Because the timing difference has a slight momentum dependence, cuts are defined for a series of bins in both proton and kaon momentum.

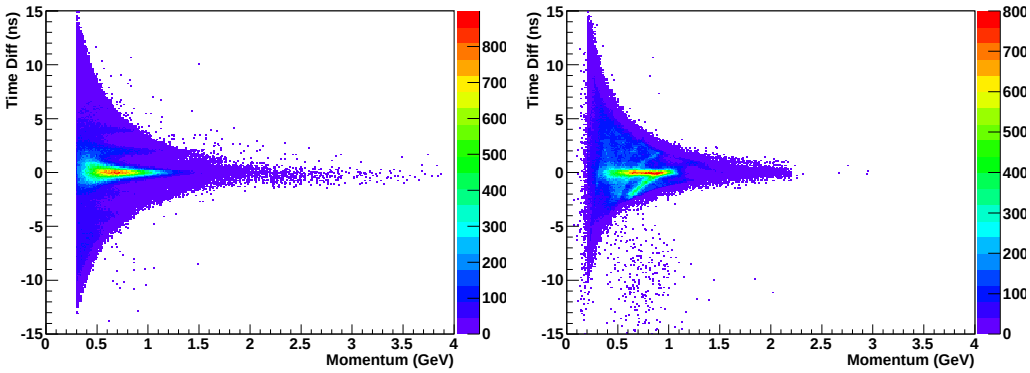

Figure 5.7: Timing vs momentum distributions for the proton (left) and kaon (right), after photon selection and before timing cuts. Several bands corresponding to misidentification of particles as kaons can be seen crossing the central peak of the kaon distribution, requiring tighter cuts than are applied to the proton.

Three momentum bins were defined for both the proton and kaon. These bins are slightly different for the two particles, due to the different reasons for applying cuts to the timing distributions for each particle, chief amongst these the pion contamination in kaon events, and the displaced vertex of the proton owing to it originating from a hyperon decay.

Timing difference vs momentum for both the proton and kaon are shown in figure 5.7. The momentum bins were defined by examining projections of momentum slices of these figures, finding regions where the width of the timing peak is similar across the bin. In the case of the proton, 3σ cuts on the central timing peak are applied in each momentum bin. Due to the contamination from misidentification of particles as kaons, the cuts for the kaon momentum slices were much narrower, σ on the peak in each bin.

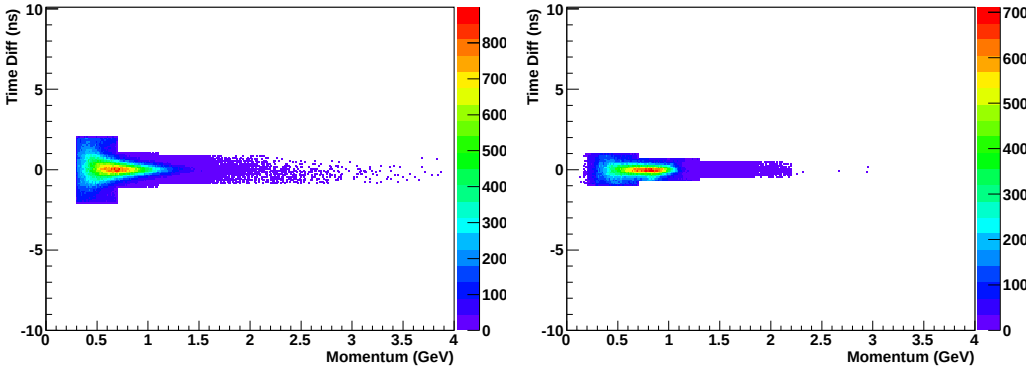

Figure 5.8: Timing vs momentum distributions for proton and kaon after the application of momentum-dependent timing cuts.

Although the tighter cuts on the kaon timing peak remove a significant number of events corresponding to misidentification of pions as kaons, some of these events will remain. It can be seen in figure 5.8 that the misidentified events form bands which cross the central timing peak, and no matter how tight the timing cuts, some events will remain under the peak. The will be removed later, at the stage of channel identification.

5.1.8 $\Delta\beta$ vs Momentum Cut

Another cut applied to remove mis-identified particles, is on the difference between the measured and calculated velocities of a particle, expressed as β; velocity as a fraction of the speed of light.

The measured value of β arises from time-of-flight measurement and using tracking information to determine the path length of a particle, which is recorded in the CLAS data structure. To calculate β, the measured momentum in CLAS is used in conjunction with the PDG mass of the particle, assuming correct particle identification, as shown in equation 5.1.

$$\beta_{calc} = \frac{p^2}{\sqrt{m^2 + p^2}} \tag{5.1}$$

Because the measured value of β is taken directly from the data, and the calculated value determined from momentum measurements assuming correct particle

identification, the difference between the two values of β will be small for correctly identified particles.

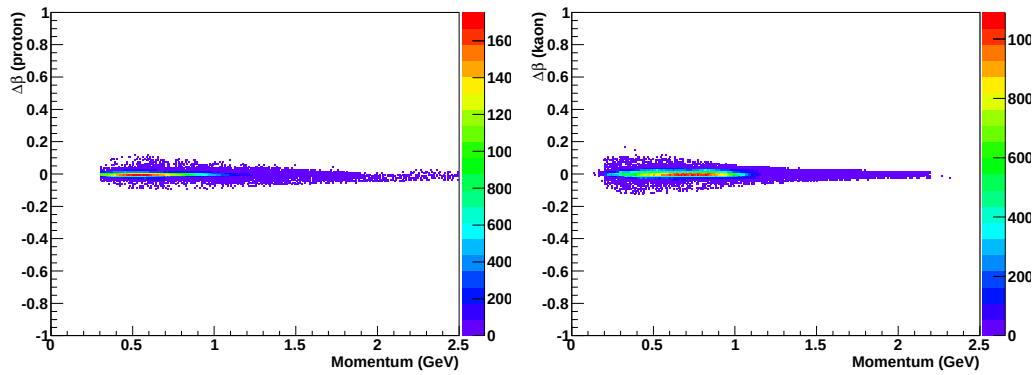

Figure 5.9: $\Delta\beta$ vs momentum distributions for the proton (left) and kaon (right).

Figure 5.9 shows the difference between the measured and calculated values of β, plotted against momentum. Most events with a significant difference in measured and calculated β occur at lower momenta. 3σ cuts were applied to the $\Delta\beta$ distributions, integrated over all momenta, corresponding to $\Delta\beta_{Proton} = 0.000 \pm 0.03$, and $\Delta\beta_{Kaon} = 0.000 \pm 0.045$.

5.1.9 Fiducial Cut

The design of CLAS, centred upon a toroidal magnetic field generated by the six superconducting coils of the torus magnet (see section 3.6.1), leads to the existence of low (and zero) acceptance regions on and around the sector boundaries. These regions are exploited by placing PMTs, lightguides, cabling and electronics, etc for various detector systems in these regions. The acceptance of these regions is non-uniform, and hard to model, and a fiducial cut is employed to remove hits in these regions from the analysis. The cut itself is $\pm 5^\circ$ around the sector boundaries, and its effect is shown in figure 5.10.

5.1.10 Summary

After the cuts described above, summarised in table 5.1, the particle identification process is considered complete, and candidate events for the reactions of interest

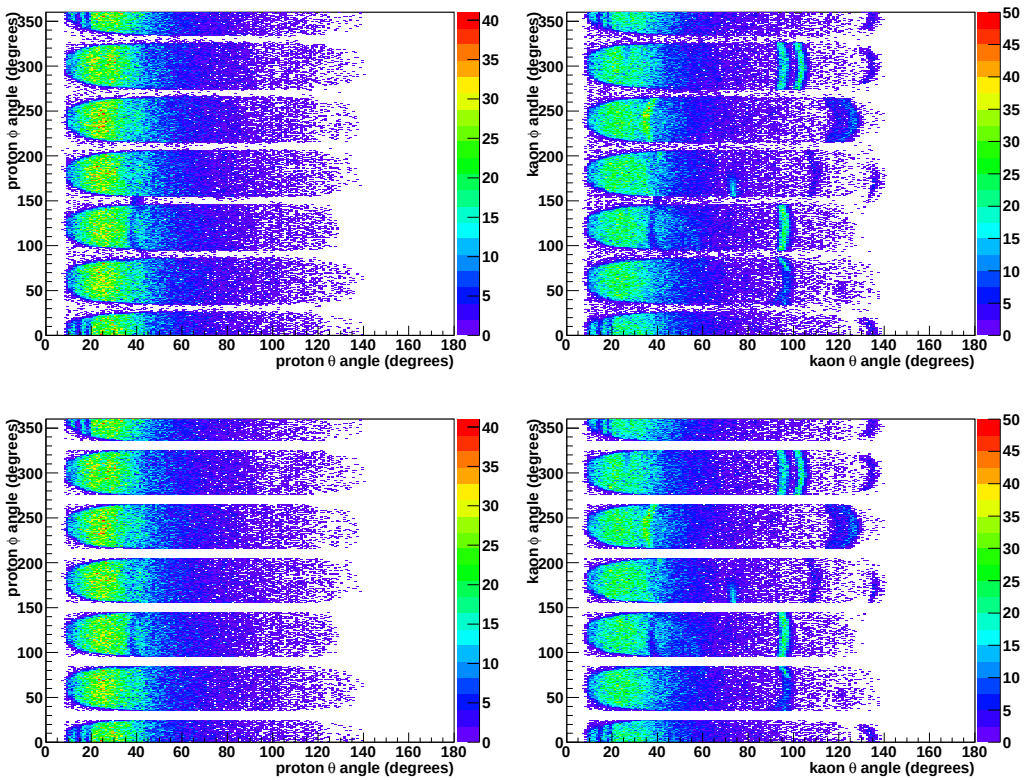

Figure 5.10: Distributions of the polar versus azimuthal angles for the proton (left) and kaon (right), before (top), and after (bottom) fiducial cuts. The bands particularly visible for the kaon distributions at angles around 100° come from badly calibrated TOF scintillators, subsequent cuts will remove these events from the analysis.

selected. These candidate events are not a definitive selection of events of interest, but are designed to reduce background without discarding good events. Subsequent cuts, described in section 5.3, will identify, and distinguish between, the $K^+\Lambda^0$ and $K^+\Sigma^0$ reactions.

5.2 Corrections to Data

Although the data has been calibrated as part of the cooking process described in the previous chapter, some post-cooking corrections are required to correct the particle four-vectors for effects not accounted for in this process. These include energy loss in the target and start counter, systematic effects arising from the design of the photon tagger, and corrections used to ensure accurate reconstruction of particle

Cut Name	Cut Value
Hit Multiplicity Cut	2, 3 or 4 particles in final state
TOF Mass (Proton)	TOF Mass between 0.49 and 1.44 GeV^2
TOF Mass (Kaon)	TOF Mass between 0.1 and 0.49 GeV^2
TOF Mass (π^-)	TOF Mass between 0.0 and 0.1 GeV^2
Initial Z Vertex Cut	-20 to 30 cm
Minimum Momentum Cut	300 MeV (Proton)
Photon Energy Cut	Peak Energy - 200 MeV (Lower) Peak Energy + 100 MeV (Upper)
Proton Timing Cut	± 2.03 ns (0.0 GeV < Proton Momentum < 0.7 GeV) ± 1.02 ns (0.7 GeV < Proton Momentum < 1.1 GeV) ± 0.89 ns (Proton Momentum > 1.1 GeV)
Kaon Timing Cut	± 0.96 ns (0.0 GeV < Kaon Momentum < 0.7 GeV) ± 0.7 ns (0.7 GeV < Kaon Momentum < 1.3 GeV) ± 0.49 ns (Kaon Momentum > 1.3 GeV)
$\Delta\beta$ Cut	0.000 ±0.030 (Proton) 0.000 ±0.045 (Kaon)
Fiducial Cut	±5° around sector boundaries

Table 5.1: Summary of particle identification cuts

four-vectors from tracks in the CLAS drift chambers.

5.2.1 Energy Loss Corrections

The measured momentum of charged particles from the drift chambers will be less than the initial momentum gained by the particle at the point of production. Before entering the drift chambers, the particle must first pass through the target material, the target wall and support structures, the beam pipe, the start counter, and the air gap immediately inside the region one drift chamber. The particle will lose energy as it passes through these materials, and this will reduce the value of momentum determined from the drift chamber tracks.

To account for this loss of energy, the ELOSS software package [80] is used, which corrects for this lost momentum by finding the pathlength of a particle through each of the intervening materials between production of the particle and it entering the drift chambers. From this, the momentum of the particle at its point of production is determined and the particle four-vector corrected.

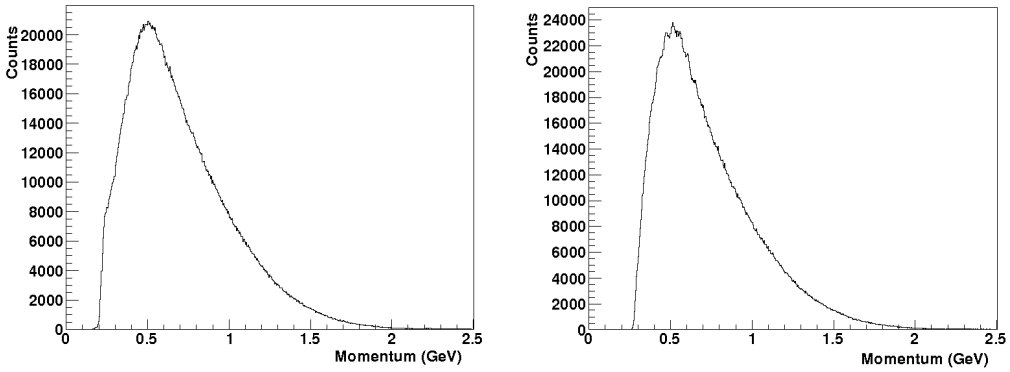

Figure 5.11: Proton momentum distribution before (left) and after (right) the application of energy loss corrections using the ELOSS package.

5.3 Channel Identification

Once particle identification has been completed and potential $K^+\Lambda^0$ and $K^+\Sigma^0$ events have been selected, further analysis is required to confirm these events are from the channels of interest and remove remaining background events, as well as separate the two reaction channels. These steps are described below.

5.3.1 Kaon Mis-Identification

One of the most common problems leading to erroneous channel identification is the mis-identification of pions in CLAS as kaons. This effect is due to the limitations imposed on particle identification from time of flight by the timing resolution of CLAS, and is demonstrated in figure 5.2, where the TOF mass region selected to identify kaons contains signifiicant contamination from both pions (the peak at the left edge of the window) and protons (the right hand edge).

The momentum-dependent proton and kaon timing cuts employed at the particle identification stage of the analysis (see section 5.1.7) remove most of the pion background for kaon detection, but some mis-identified events remain under the kaon timing peak. Figure 5.12 shows the TOF mass selection window for kaons (positive charged particles with mass between 0.1 and 0.49 GeV^2), before and after the application of the timing cuts.

As can be seen in the figure, the proton and pion backgrounds are greatly reduced

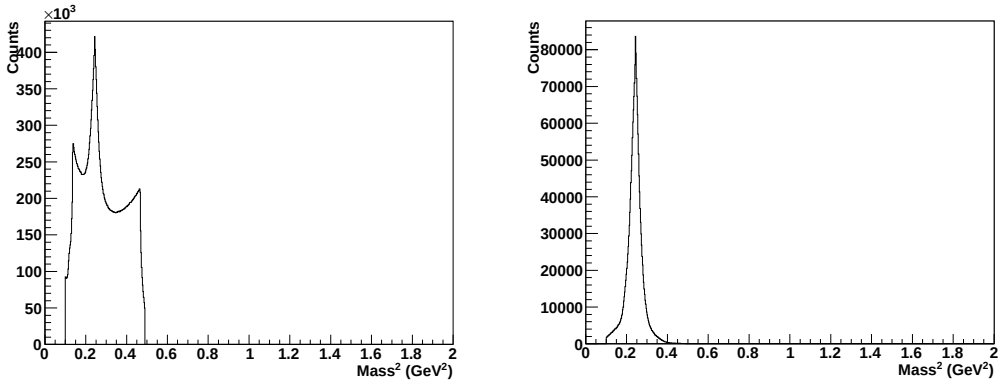

Figure 5.12: Time-of-flight mass of kaons before (left) and after (right) momentum dependent timing cuts.

by the timing cuts, although some noticable pion contamination remains, which will be reduced further by the cuts made to the data in the following sections. These cuts are on the mass of the pion, reconstructed from the proton and kaon via the missing mass technique, where the proton and kaon 4-vectors are subtracted from the sum of the 4-vectors of the beam photon and target proton. Cuts are also applied to the z-vertex on the individual target materials in the FROST target assembly, and further channel identification cuts are made on the kaon missing mass and the invariant mass of the proton and reconstructed pion.

5.3.2 Pion Reconstruction

Due to the non-exclusive particle identification scheme employed, only the detection of a proton and kaon in the final state are required, with the possibility of detecting the pion from the Λ decay and the final state photon and pion for $K^+\Sigma$ events retained as an option only. As figure 5.1 shows, a large number of potential events have only two detected particles in the final state, due to the low acceptance of photons and the positive torus field setting acting to reduce the acceptance of the negatively charged pion by bending negatively charged particles into the beamline hole of CLAS.

In order to identify events that produced a Λ or Σ hyperon, the pion is reconstructed via the missing mass of the detected proton and kaon. This is done for all events, regardless of whether or not the pion (and/or photon) was detected. For

events where a Λ or Σ hyperon was produced, the missing mass will correspond to that of the undetected pion (0.0185 GeV^2), or the undetected pion and photon combination.

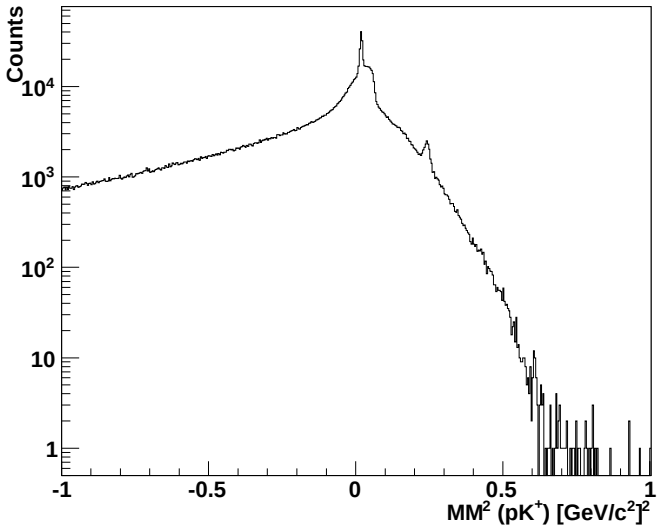

Figure 5.13: Squared missing mass of detected proton and kaon events. A peak corresponding to the pion missing mass is clearly visible at 0.0185 GeV^2. This sits on top of a less clear peak corresponding to $K^+\Sigma$ events. The peak at 0.240 GeV^2 corresponds to a K^- from $\gamma p \rightarrow \phi p \rightarrow K^+K^-p$ events.

The missing mass distribution for detected protons and kaons is shown in figure 5.13. The distribution shows a clear peak corresponding to the pion missing mass, sitting on top of a less clear peak at a slightly higher missing mass, which corresponds to $K^+\Sigma$ events. Also visible is a peak corresponding to a missing K^-, from $\gamma p \rightarrow \phi p \rightarrow K^+K^-p$ events. At this stage a cut is applied on the proton-kaon missing mass squared from -0.2 GeV^2 to 0.3 GeV^2. This is a fairly loose cut, which still allows the K^- events to survive, but subsequent cuts will remove these and other background events which remain after this cut.

5.3.3 Target Selection

At this stage, the events are separated according to which material in the FROST target they originated in. As discussed in section 5.1.3, and chapter 3, the FROST target contains three target materials; polarised butanol, and unpolarised carbon

and polythene.

As explained in section 5.1.3, the detected proton originates from the decay of the hyperon, as does the pion, which is not always detected, and the z vertex information from these particles is not suitable for target separation (see figure 5.14). For this reason, the kaon z vertex is used for target selection as the only detected particle originating in the target.

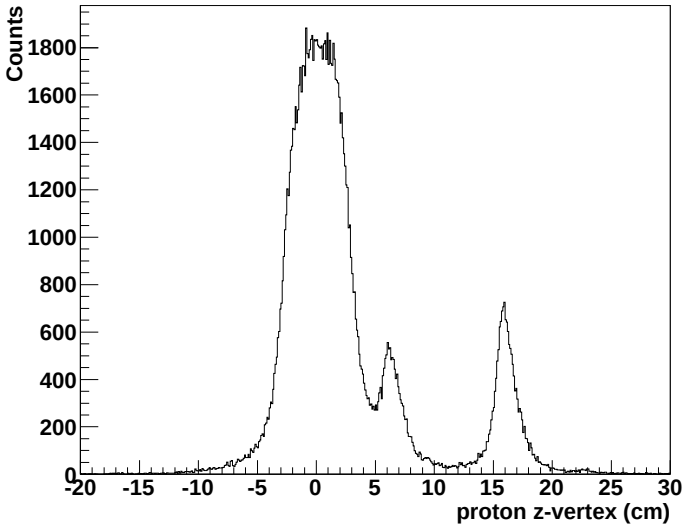

Figure 5.14: Proton z vertex showing the three target materials in the FROST target. Even after the particle identification cuts it is difficult to separate the carbon and polythene targets.

Butanol events are selected by a kaon z-vertex cut from -3 to 3 cm, carbon events with a cut from 5 to 7 cm, and polythene events with a cut from 15 to 17 cm. These are indicated on figure 5.15, which shows the z-vertex distribution after all cuts described to this point.

The separation of the butanol and carbon targets is not particularly good at this point, as several sources of background remain. Following the selection of the reaction channels, described in the next section, these background processes are greatly reduced and the target selection cuts are re-examined following channel selection in section 5.3.5.

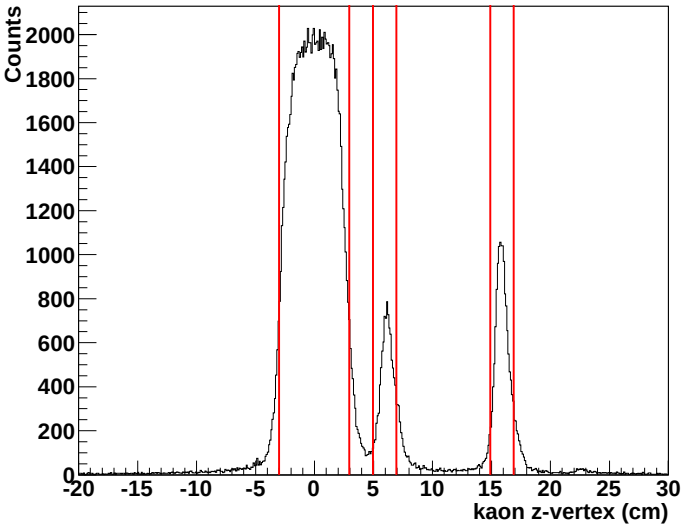

Figure 5.15: Kaon Z vertex distribution for target election. Unlike the proton, the detected kaon originates in the target material, making its z-vertex more reliable for the selection of events from each target material in FROST. The target selection cuts employed in the analysis are indicated by the red lines.

5.3.4 Hyperon Selection

At this stage, the $K^+\Lambda^0$ and $K^+\Sigma^0$ reactions are identified. This is achieved by two cuts; the first a cut on the invariant mass of the proton and reconstructed π^-, and the second on the Kaon missing mass. These two quantities are shown in a two-dimensional plot in figure 5.16.

Because the pion is not always detected in this analysis, its 4-vector is reconstructed by subtracting the the detected proton and kaon 4-vectors from the sum of the photon and target 4-vectors. The resulting 4-vector is assigned the PDG mass of the π^-, which assumes correct particle identification.

A cut to remove events where the invariant mass of the proton and reconstructed pion is not consistent with a decaying hyperon is performed, from 1.0 to 1.2 GeV in Invariant Mass ($p\pi^-$). This will remove many of the events where misidentification of particles has occurred.

Next, the hyperon channel is selected by a cut on the missing mass of the Kaon. $K^+\Lambda$ events are identified as having a kaon missing mass between 1.0 and 1.15 GeV, and $K^+\Sigma$ events having a kaon missing mass between 1.15 and 1.25 GeV.

These values for the hyperon selection cuts are preliminary, with the final channel selection cuts decided after consideration of the background in the Kaon missing mass, which can be seen in figure 5.17, and of which the carbon in the butanol and polythene targets forms a significant source. This will be done in the next chapter.

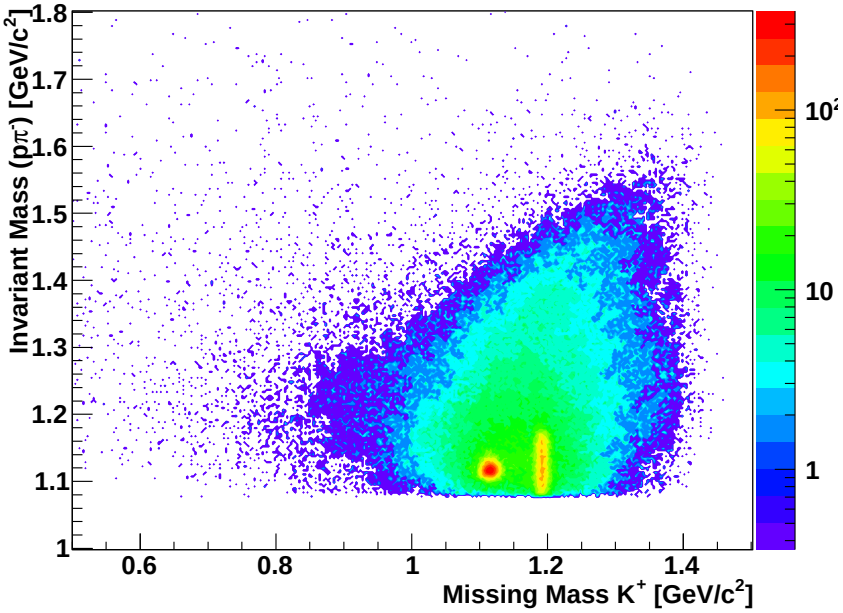

Figure 5.16: Kaon missing mass vs proton-pion invariant mass for the butanol target. Two clear peaks are visible corresponding to Λ and Σ^0 events.

5.3.5 Final Target Selection

As discussed in section 5.1.3, a plot of the Kaon z-vertex is able to identify the three target materials, and preliminary selection of these targets is described in section 5.3.3.

Now that the reaction channels have been identified, the kaon z-vertex is re-examined to verify these target selection cuts. It is important that the events are separated by the target they originated in, as events from the carbon target are used in the calculation of scaling factors and the dilution of measured observables on the polythene and butanol targets. If the targets are not adequately separated in the analysis, the events will be contaminated by those from other target materials and the calculated scaling factors, and resulting dilution of observables, will be

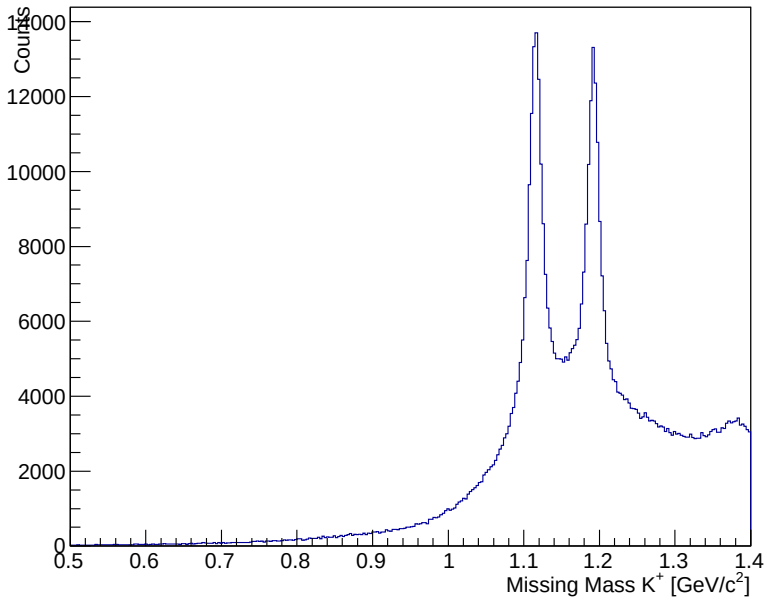

Figure 5.17: Kaon missing mass spectrum for the butanol target in FROST, showing the Λ and Σ^0 peaks. These peaks sit on a significant background, arising primarily from the carbon nuclei in the butanol.

unreliable.

Following the channel identification cuts described in the previous section, removing events not corresponding to reactions of interest, the target separation has been greatly improved and the butanol and carbon targets are now much easier to resolve. The kaon z vertex for $K^+\Lambda$ channel selection is shown in figure 5.18, verifying the target selection cuts employed in section 5.3.3.

5.3.6 Summary

The additional cuts applied to identify the $\gamma p \rightarrow K^+\Lambda$ and $\gamma p \rightarrow K^+\Sigma^0$ reactions from the candidate events selected by the previously described particle identification cuts are summarised in table 5.2.

In the next chapter, the methods used to measure polarisation observables using these extracted $K^+\Lambda$ and $K^+\Sigma^0$ events will be described, as will the techniques employed to identify and account for the nuclear and molecular properties of the target materials used.

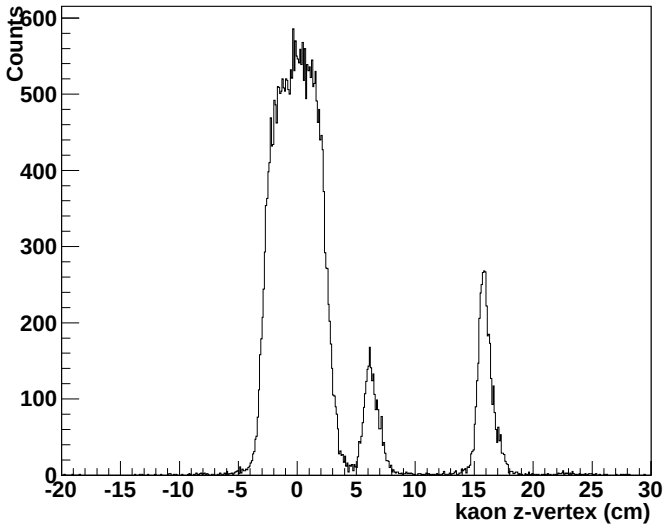

Figure 5.18: Kaon z vertex for final $K^+\Lambda$ selection. Events corresponding to the carbon and butanol targets can easily be separated by the target selection cuts employed.

Cut Name	Cut Value
Proton-Kaon Missing Mass Cut	-0.2 to 0.3 GeV^2
Final Target Selection Cuts	-3 to 3 cm (Butanol) 5 to 7 cm (Carbon) 15 to 17 cm (Polythene)
Invariant mass (Proton + Reconstructed Pion) Cut	1.0 to 1.2 GeV^2
Hyperon Selection Cuts (MMPK)	1.0 to 1.15 GeV (Λ) 1.15 to 1.25 GeV (Σ)

Table 5.2: Summary of channel identification cuts

Chapter 6

Extraction of Polarisation Observables

In this chapter, the methods by which the Σ and G polarisation observables were extracted for the reactions of interest will be discussed, along with the techniques employed to account for effects of the nuclear and molecular properties of the target materials in FROST.

Aside from accounting for these target effects, the Σ extraction is relatively straightforward, having been carried out on several reaction channels in previous analyses of CLAS data [39, 41, 42, 81]. For the G observable, techniques have been developed based on the methods used for the extraction of Σ, extending it to the beam-target double polarisation observables.

6.1 Overview

Now the reactions have been identified and reconstructed from their final state particles in CLAS, the extraction of polarisation observables can take place. This analysis is concerned with the measurement of two observables for two reaction channels; the Σ and G polarisation observables for the reactions $\gamma p \rightarrow K^+\Lambda^0$ and $\gamma p \rightarrow K^+\Sigma^0$.

As discussed in chapter 2, several measurements of the Σ observable for these channels have been made in previous experiments at several experimental facilities

[39,43,47], and its measurement in this work serves as a cross-check of the previous data and model predictions. By repeating these previous measurements, carried out on simpler targets, it is intended to show that the methods employed to account for the more complicated nature of the FROST target are suitable, and can be applied to measurements of the G observable.

This will be achieved by first demonstrating that a Σ measurement on the proton is possible with data from an unpolarised hydrocarbon target (the polythene built into the FROST target assembly), where there is no chance of interference in the measurement from beam-target polarisation observables. The Σ observable will then be measured for the polarised butanol data, to show that such a measurement is unaffected by the presence of target polarisation and that proper account can be taken of the presence of bound nucleons in the target material when measuring G.

6.2 Bin Selection

The choice of bin widths for each kinematic variable used for the measurement of the Σ and G polarisation observables was made by balancing the desire to maximise the information extracted as a function of the variables, W and $\theta^{K^+}_{CM}$, with the limitations imposed by the amount of available data. The two kinematic variables are shown plotted against each other for the butanol data in figure 6.1.

These considerations are further complicated by the nature of the photon beam, which was produced at nine discrete coherent peak energy settings, seven of which were at energies suitable for hyperon production. Photon polarisation and luminosity decrease away from the coherent edge energy, an effect which is reduced by the photon beam energy cut discussed in section 5.1.5 of chapter 5. The resulting photon energy distribution, which directly correlates to W, has several peaks, each corresponding to a coherent peak setting in photon energy. It was decided to select W bins which roughly correspond to these coherent peak settings, around 200 MeV wide in photon energy, centred on the coherent peak.

For $\theta^{K^+}_{CM}$, four bins of variable width, spanning the full angular range of $\theta^{K^+}_{CM}$ ($\cos(\theta^{K^+}_{CM}) = \pm 1$) were chosen, such that each bin contains a roughly equal number

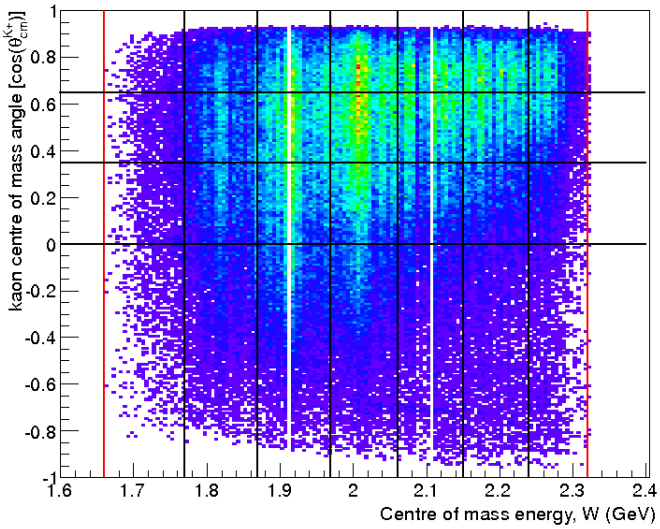

Figure 6.1: Centre of mass energy, W, versus $cos(\theta_{cm}^{K+})$ for $K^+\Lambda$ events originating from the butanol target. The kinematic bins used in the analysis are indicated by the black lines, with the W range studied bounded by the red lines.

of events. These widths remain fixed for all W bins for simplicity, even though this will cause some disparity in the number of events in the bins at the upper and lower energies. This is mitigated somewhat by the fact that requiring the bins to contain an equal number of events would cause the bin centres to change.

6.3 Carbon Scaling Factors

In order to make a measurement of the Σ observable from the hydrogen present in the polythene and butanol targets in FROST, consideration must be taken of the non-hydrogen contribution to any measurement of the Σ observable. This non-hydrogen background is also important in the resolution of the Λ and Σ hyperons from kaon missing mass, in order to verify the channel selection cuts on the kaon missing mass discussed in the previous chapter.

Because the butanol is not a 100% polarised hydrogen target, the amount of unpolarised material in the butanol target must be estimated when measuring the G observable, in order to account for the dilution effect this will have on the values of G extracted.

Key to all these considerations is the Carbon Scaling Factor (CSF), the amount

by which data from the carbon target should be scaled such it can be used to characterise the amount of carbon present in the polythene and butanol targets. These scaling factors will be used when extracting observables, as discussed in section 6.5.

Two methods have been developed to estimate CSFs; a direct scaling method, where the kaon missing mass for the polythene or butanol is divided by that for the carbon, and phase space dependent scaling, which relies on selection of events that can only come from bound nucleons (i.e. those from carbon or oxygen in the targets).

These methods assume that all bound nucleon events from the targets manifest in a similar manner to carbon. For polythene, which consists only of hydrogen and carbon, this assumption is not necessary, but butanol is complicated by the presence of an oxygen atom. Like carbon, the oxygen atom in butanol has spin zero (and is unpolarisable), and has equal numbers of protons and neutrons. For these reasons, and the previous manner bound nuclei from different atoms have been handled in analyses of similar target materials at JLab [82], the bound nucleons in oxygen are assumed to have identical effects to the carbon, and will be characterised as part of the determination of carbon scaling factors.

6.3.1 Direct Scaling

The direct scaling method defines a Carbon Scaling Factor from the ratio of events on the hydrogen-containing targets (polythene and butanol) to those on the pure carbon target. The additional momentum provided by Fermi motion in the bound nucleons present in the polythene and butanol targets means that when compared to the free proton, more background events are found in the mass and missing mass spectra of interest. By examining the ratio of events between a hydrogen-containing target and a pure carbon target, the fraction of bound nucleons present in these materials can be characterised.

For the Kaon channels in g9a, the kaon missing mass spectra are used to define carbon scaling factors. Figures 6.2 to 6.4 show the kaon missing mass spectra for the butanol, polythene and carbon targets. Peaks corresponding to the Λ and Σ

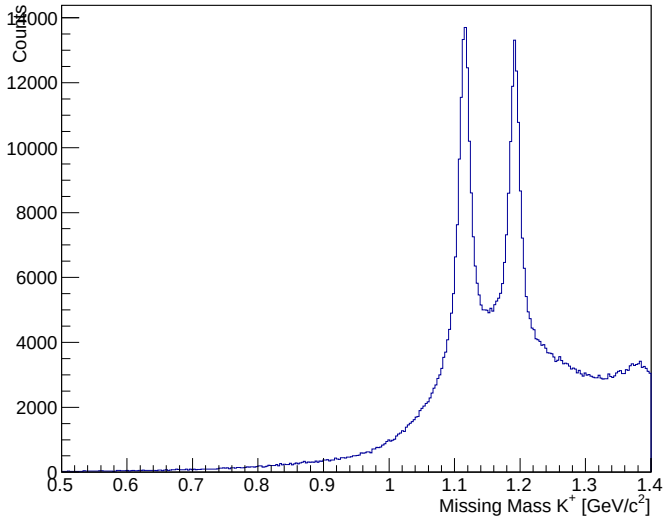

Figure 6.2: Kaon missing mass spectrum for the butanol target in FROST. Peaks corresponding to Λ and Σ hyperons can be seen on top of a large background arising from bound nucleons in the butanol.

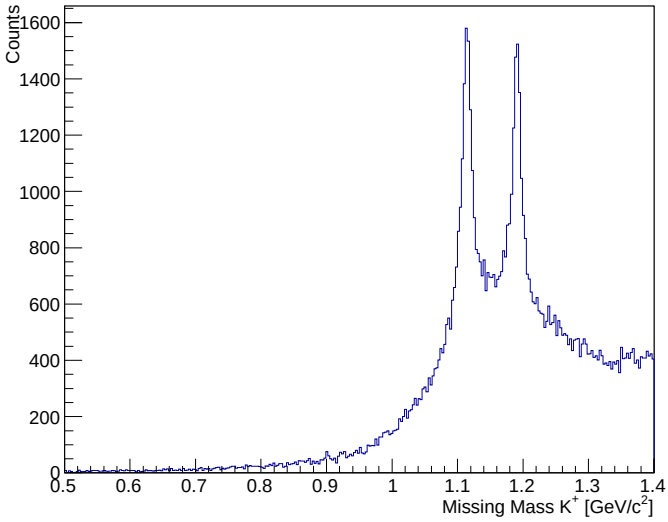

Figure 6.3: Kaon missing mass spectrum for the polythene target in FROST. Peaks corresponding to Λ and Σ hyperons can be seen on top of a large background arising from bound nucleons in the target.

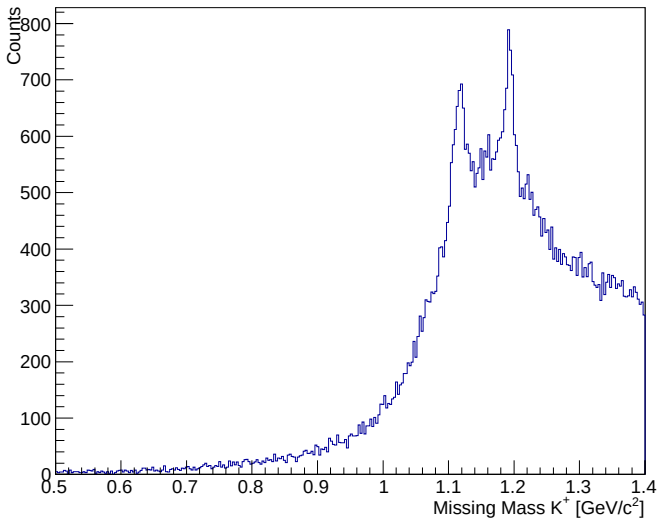

Figure 6.4: Kaon missing mass spectrum for the carbon target in FROST. This target has larger bound nucleon background underneath the hyperon peaks than for the polythene or butanol targets due to the absence of molecular hydrogen in the target.

hyperons are visible on all three plots at the appropriate masses, with varying degrees of background due to bound nucleon events. The carbon data, consisting solely of bound nucleons, has the largest amount of such background.

To define carbon scaling factors, the missing mass spectrum for the Kaon on the target of interest was divided by the corresponding spectrum for carbon, and the result of this on the butanol target is shown in figure 6.5.

As figure 6.5 shows, the butanol to carbon ratio still has two peaks corresponding to the Λ and Σ hyperons, and a relatively flat distribution at lower kaon missing mass. The carbon scaling factors are defined for each energy bin for both the polythene and butanol targets by measuring the ratio of hydrogen-containing target to carbon data for kaon missing mass below 1.0 GeV, in order to avoid contamination from the hyperon peaks. The resulting polythene and butanol scaling factors are shown in table 6.1.

The carbon scaling factors defined by this method will be used for verification of the hyperon selection cuts in kaon missing mass, by subtracting a scaled carbon spectrum from the butanol in order to approximate the proton spectrum. These scaling factors will also be used when accounting for dilution of the hydrogen-containing

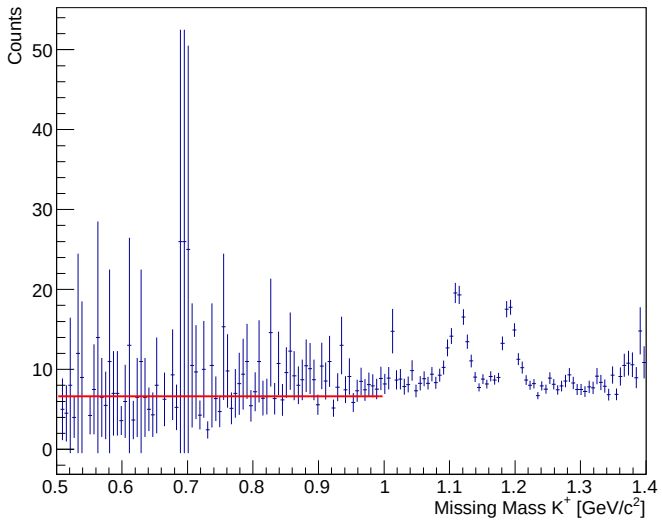

Figure 6.5: Kaon missing mass spectrum for butanol divided by carbon. A carbon scaling factor is defined from the ratio of these spectra below the hyperon peaks.

W Range (GeV)	Scaling Factor (butanol)	Scaling Factor (polythene)
1.66 - 1.77	5.31±0.22	0.78±0.04
1.77 - 1.87	5.71±0.25	0.70±0.05
1.87 - 1.97	5.00±0.23	0.75±0.05
1.97 - 2.06	5.64±0.19	0.75±0.04
2.06 - 2.15	5.84±0.25	0.79±0.05
2.15 - 2.24	6.20±0.26	0.73±0.05
2.24 - 2.32	5.31±0.28	0.77±0.08

Table 6.1: Carbon scaling factors for butanol and polythene, determined by the direct scaling method.

targets on the values extracted from the data for the polarisation observables of interest. The use of carbon scaling factors for these aspects of the analysis will be discussed in sections 6.4 and 6.5.

6.3.2 Phase Space Dependent Scaling

The phase space dependent scaling method [83], developed by Arizona State University, is an alternative means of determining the scaling factor for carbon. Like the direct scaling method, phase space dependent scaling exploits the differences between free proton and bound nucleon events caused by the additional momentum provided by fermi motion in the bound nucleus.

Phase space scaling relies upon the fact that for a free proton, there are forbidden kinematical regions due to energy and momentum conservation laws, and involves examining these kinematic regions forbidden to the free proton, but accessible from the bound nucleon.

Overlapping regions of phase space for free and bound nucleon reactions are identified and the polythene and butanol target data are divided by the carbon data for the bound nucleon regions for a series of phase space bins, allowing the determination of a phase space dependent scaling factor.

This technique was developed for pion channels, and its application to the strangeness channels is described here. For the pion channels, the phase space scaling method uses the recoil proton, detected in the final state ($\gamma p \rightarrow pX$). However, the final state proton for the kaon channels originated from a decaying Λ, and therefore has a displaced vertex. The associated difficulties in resolving and separating the target materials in FROST using particles with displaced vertices means the proton is not suitable for identifying phase space regions associated with bound nucleons for these channels. The hyperon is instead used as an analogous particle for the kaon channels, $\gamma p \rightarrow YX$, where 'Y' denotes a hyperon. The hyperon is not directly detected, instead it is reconstructed from the detected proton and pion 4-vectors, and the reaction used is actually $\gamma p \rightarrow p\pi^- X$.

Because the hyperon is exclusively identified from its decay products, a more relaxed particle and channel identification scheme can be used than was described in the previous chapter. The proton-kaon missing mass cut (see section 5.3.2) is not applied, as the pion is explicitly detected here, neither is the kaon missing mass cut used to identify the KΛ and KΣ reactions described in section 5.3.4. These relaxed cuts also maximise the number of events available for the determination of scaling factors from the limited hyperon events in the g9a data for which three final state particles were detected.

The squared missing mass of the reconstructed hyperon is examined for the butanol target, and is divided into two regions; "low" missing mass where events are from bound nucleons only, and "high" missing mass where both free and bound nucleon events occur. In order to define where the exclusively bound nucleon events

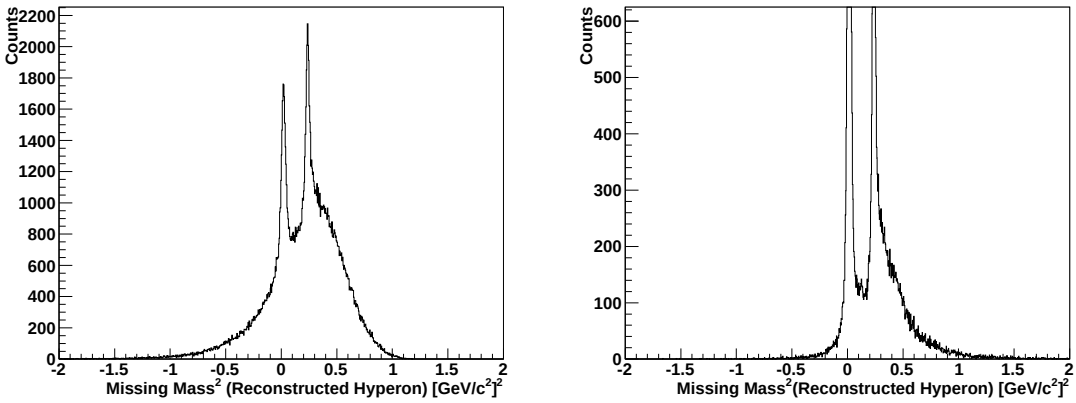

Figure 6.6: Squared missing mass distribution of reconstructed hyperon events for butanol (left) and hydrogen (right), where g8b data has been used for its hydrogen target. For ease of comparison, the scale on the hydrogen plot has been adjusted to match that for the butanol, weighted for the number of events in each plot.

are in hyperon missing mass and define the low and high missing mass regions, free proton data from the g8b experimental run [39,84] was subjected to the same relaxed particle and channel identification scheme, with some cuts adjusted to suit the g8b run conditions (such as the z-vertex cuts). The high missing mass region containing a mixture of free and bound nucleon events was defined as having missing mass greater than -0.2 GeV, and the exclusively bound nucleon region as having missing mass less than -0.35 GeV, the point where the number of events on the liquid hydrogen data begins to increase significantly from zero.

The hyperon momentum phase space of these two regions in missing mass is then examined (see figure 6.7). These regions do not overlap well, requiring a different topology to be used to identify bound nucleon events.

The alternative topology $\gamma p \rightarrow K^+YX$ was used (actually $\gamma p \rightarrow K^+p\pi^-X$ as the hyperon must be reconstructed), requiring the detection of proton, kaon and pion to reconstruct the hyperon, and the same low missing mass squared cut is used to define the bound nucleon events.

The phase space for bound nucleons in $\gamma p \rightarrow K^+p\pi^-X$ better matches that of the free-and-bound nucleon phase space of the hyperon (see figure 6.8) and is used to determine scaling factors by taking the ratio of butanol to carbon events for a series of phase space bins in the bound nucleon missing mass region of $\gamma p \rightarrow K^+p\pi^-X$.

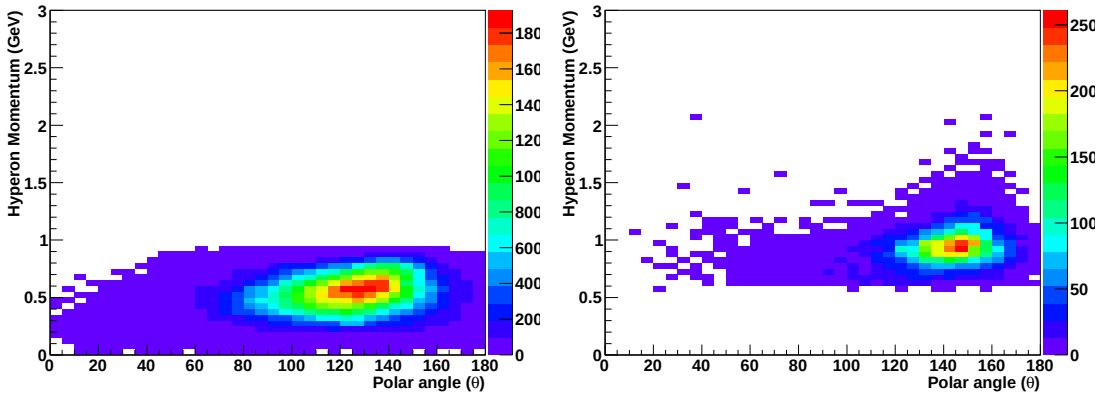

Figure 6.7: Phase space regions of reconstructed hyperon events ($\gamma p \rightarrow YX$) for the high (left) and low (right) missing mass regions. The low missing mass region contains bound nucleon events only. These regions of phase space do not overlap well, requiring an alternative topology to be used to define a bound nucleon phase space region from which to determine scaling factors.

Hyperon Momentum (GeV)	Scaling Factor
0.0 - 0.4	2.30±0.46
0.4 - 0.8	3.89±0.53
0.8 - 1.2	4.48±0.61
$\geq$ 1.2	2.19±0.57

Table 6.2: Carbon scaling factors for butanol on KΛ, determined by the phase space scaling method.

Because of the limited data available for determining phase space scaling factors for the strangeness channels, the values obtained are subject to larger statistical errors on the butanol target than for direct scaling, and it was not possible to obtain polythene scaling factors. For these reasons, the direct scaling method was used in the analysis when accounting for the presence of carbon in the polythene and butanol targets, although a brief comparison of the two methods will be made on the butanol data in the next section.

6.4 Final Hyperon Selection

Now that the amount of carbon present in the polythene and butanol targets can be determined from the carbon scaling factors, the bound nucleon background in the kaon missing mass, used to identify hyperons, can be accounted for and the cuts

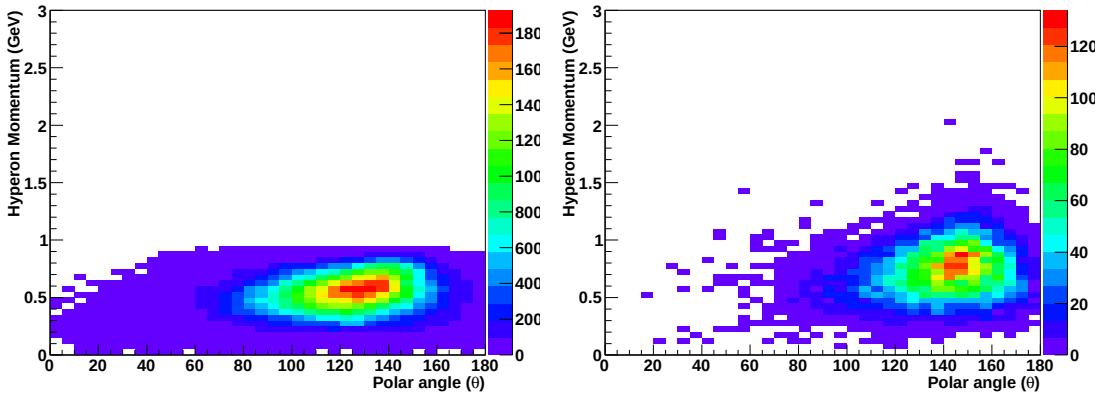

Figure 6.8: Phase space regions of reconstructed hyperon events for the high missing mass region of $\gamma p \rightarrow YX$ (left) and the low missing mass region of $\gamma p \rightarrow K^+YX$ (right). The low missing mass region contains bound nucleon events only. These regions of phase space overlap better than those in figure 6.7, allowing scaling factors to be determined by dividing the bound nucleon phase space for butanol by carbon.

used to select the $K^+\Lambda$ and $K^+\Sigma$ channels first described in section 5.3.4 can be verified.

This is achieved by first multiplying the kaon missing mass plot for carbon by the scaling factor for the target of interest, and subtracting it from the corresponding plot for the target of interest. The results of this process are shown in figure 6.9 for the polythene data and figure 6.10 for butanol.

After this subtraction has been carried out, and the large backgrounds due to bound nucleon effects removed, the Λ and Σ hyperons are easily resolvable. To define the final hyperon selection cuts, Gaussian fits are performed on the Λ and Σ peaks, and the cuts defined as the mass range within 2σ of each peak. Although a 3σ cut would be preferred, the range around each hyperon would have a significant overlap in the mass range between them, so a narrower cut is used where this overlap is smaller. The final hyperon selection cuts are shown in table 6.3.

Hyperon Channel	Selection Cut in Kaon Missing Mass (GeV)
$\gamma p \rightarrow K^+\Lambda$	1.068 - 1.152
$\gamma p \rightarrow K^+\Sigma$	1.152 - 1.232

Table 6.3: Final hyperon selection cuts on kaon missing mass, after subtraction of appropriately scaled carbon data.

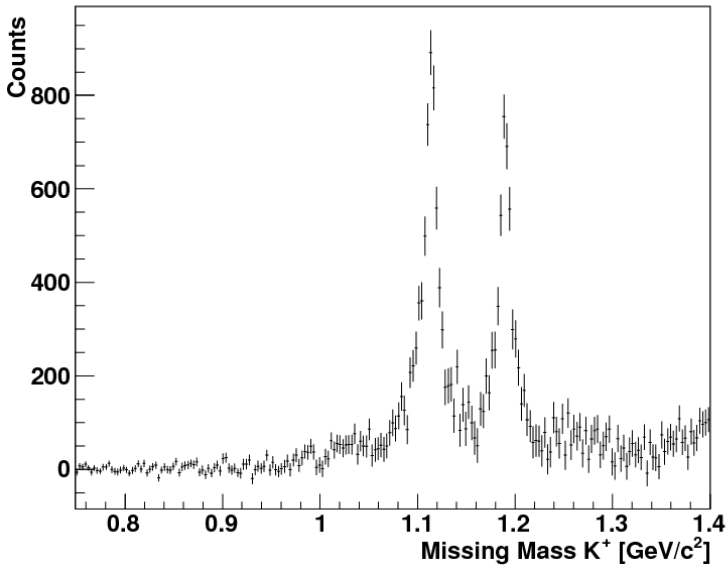

Figure 6.9: Kaon missing mass on polythene after subtraction of scaled carbon. The bound nucleon background has been removed, and the hyperons can be easily separated.

6.4.1 Comparison of Carbon Scaling Techniques

As a cross check of the validity of the direct scaling method for characterising the amount of carbon present in the polythene and butanol targets, the same carbon subtraction procedure was performed using the phase space scaling factors.

Figure 6.12 shows the result of the phase space based carbon subtraction on butanol data, showing significant background events remaining. Although similar mass ranges can be defined via Gaussian fits to the hyperon peaks, the remaining background makes these ranges, and separation of the hyperons, less reliable.

6.5 Extracting Observables

For the g9a experiment, the FROST target contained both unpolarised and longitudinally polarised target materials from which polarisation observables can be extracted. The unpolarised polythene target has been built into FROST with the intention of demonstrating that polarisation observables can be measured on molecular protons in a target, and that such a measurement is consistent with that on the free proton.

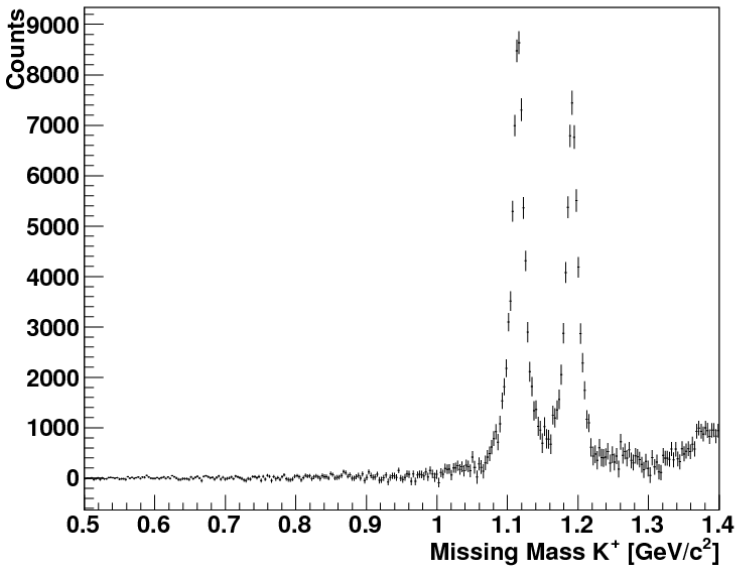

Figure 6.10: Kaon missing mass on butanol after subtraction of scaled carbon. The bound nucleon background has been removed, and the hyperons can be easily separated.

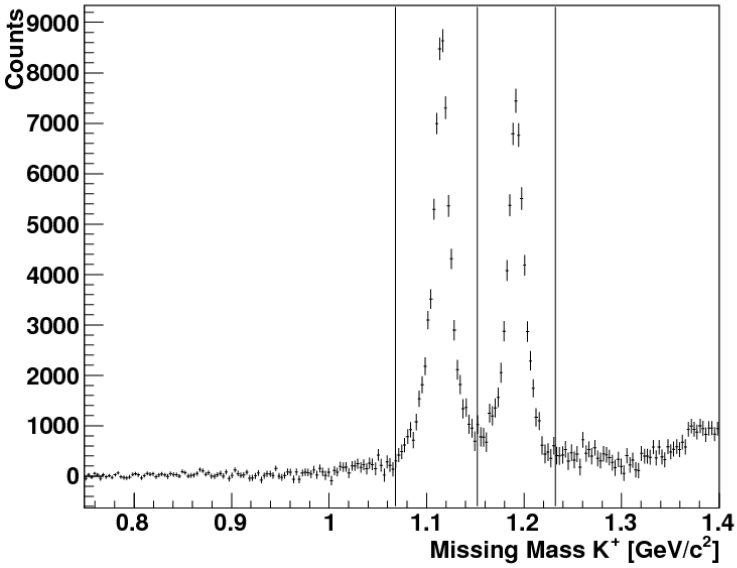

Figure 6.11: Kaon missing mass on butanol after carbon subtraction, showing the final hyperon selection cuts.

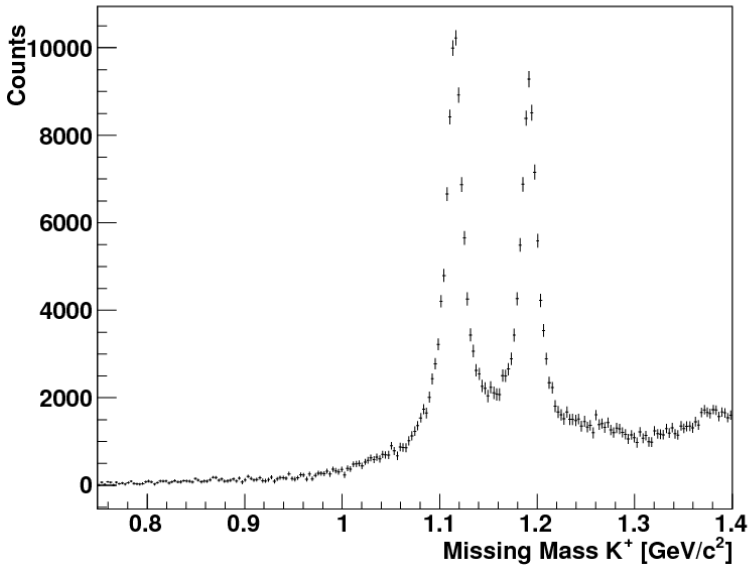

Figure 6.12: Kaon missing mass on butanol after subtraction of scaled carbon using the phase space based scaling factors. Not all of the bound nucleon background has been removed, and the separation of the hyperons is more difficult.

The beam polarisation observable, Σ was chosen for this verification, due to the wealth of experimental data available for comparison, and the straightforward, well understood method for making such a measurement from asymmetries of data for the two states of linear beam polarisation. As a result of the non-Hydrogen components of the target, and the contribution of bound nucleon events to the measured observables, the values of polarisation observables measured from asymmetries are diluted. This dilution effect is characterised through the use of carbon scaling factors and asymmetry measurements on the carbon target.

Because polythene and carbon are unpolarised, the possibility of any potential systematic effects due to target polarisation is excluded. The same principles can then be applied to the polarised butanol data in order to measure the Σ and G observables. Bound nucleon events will not contribute to the G observable as the carbon in butanol is unpolarisable, making the dilution effect much simpler to calculate for G.

6.5.1 Observable Extraction from Beam Asymmetries

As discussed in chapter 1, for the situation of a linearly polarised photon beam incident on a longitudinally polarised target, the overall differential cross section can be expressed in terms of the Σ and G polarisation observables;

$$\frac{d\sigma}{d\Omega} = \sigma_0\{1 - P_{lin}\Sigma cos(2\phi) + P_z(P_{lin}Gsin(2\phi))\} \tag{6.1}$$

Where P_{lin} denotes the degree of polarisation of the photon beam, and P_z denotes the degree of polarisation of the target. Additionally, for the unpolarised carbon and polythene targets in FROST, $P_z = 0$ and equation 6.1 reduces to;

$$\frac{d\sigma}{d\Omega} = \sigma_0\{1 - P_{lin}\Sigma cos(2\phi)\} \tag{6.2}$$

As there are two orthogonal polarisation settings for the linearly polarised photon beam (PARA and PERP), observables can be extracted from the asymmetry of the distributions of kaon azimuthal angle (ϕ) for the two states. This method has the advantage of cancelling out acceptance effects in the detector system, removing the need to perform detailed acceptance calculations, which could result in the introduction of large systematic uncertainties in the extraction of observables. The asymmetry is equated with the reduced cross-section expression to extract observables. In the simple case of an unpolarised target;

$$A(\phi) = \frac{N(PARA) - N(PERP)}{N(PARA) + N(PERP)} = P_{lin}\Sigma cos(2\phi) \tag{6.3}$$

By applying a fit of the form of equation 6.3, the Σ observable can be extracted on unpolarised target data for each kinematic bin. This method of Σ extraction is well understood and has been used in many previous analyses [39, 41, 42, 81].

This picture is slightly complicated by the PARA and PERP data sets not having the same number of events or mean value of polarisation. To deal with this, the two sets of data are scaled, modifying the asymmetry expression as follows;

$$A(\phi) = \frac{N(PARA) - N(PERP)}{N(PARA) + N(PERP)} = \frac{2P^{\parallel}P^{\perp}}{P^{\parallel} + P^{\perp}}\Sigma cos(2\phi) \tag{6.4}$$

Where $P^{\parallel}$ and $P^{\perp}$ are the mean polarisations of the PARA and PERP data, respectively.

Figure 6.13 shows a sample asymmetry, constructed from PARA and PERP data from the unpolarised polythene target. A fit of the form of equation 6.3 is performed on the resulting distribution, and the parameter extracted is a measurement of $P_{gamma}\Sigma$ for polythene.

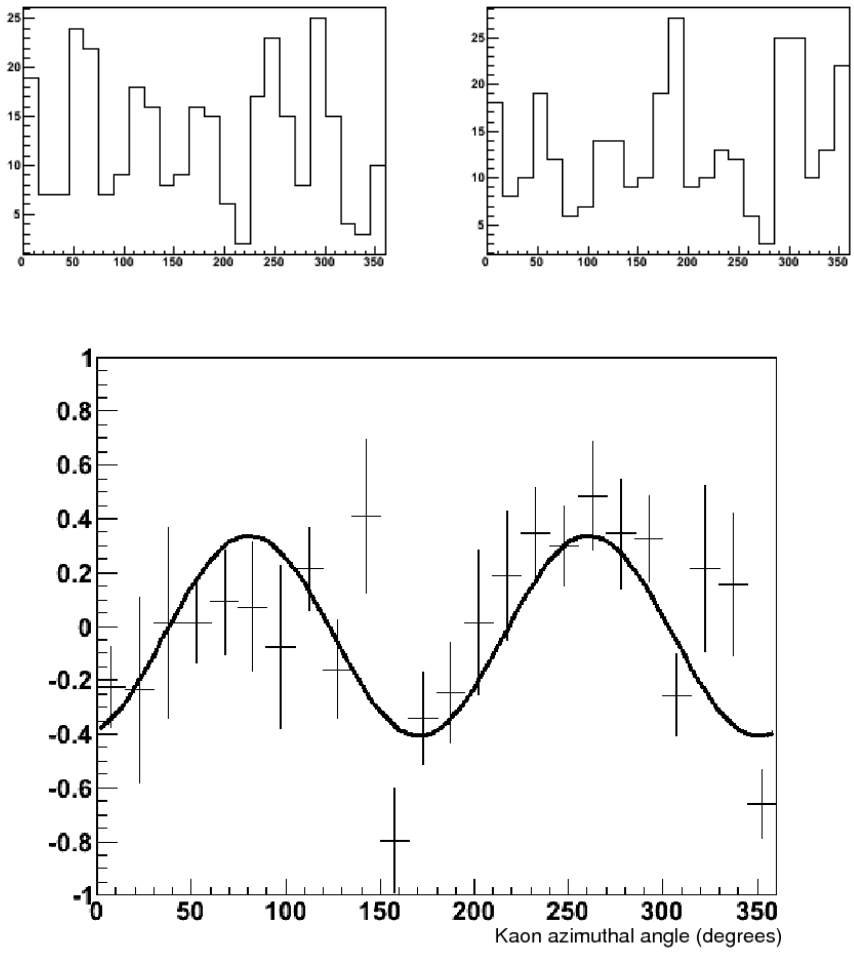

Figure 6.13: A sample PARA/PERP asymmetry, constructed from FROST polythene data at the 1.5 GeV photon energy setting. A $\cos(2\phi)$ fit is performed on the asymmetry distribution to extract the Σ observable.

For a longitudinally polarised target, the same principle can be applied, however, the fit function must take account of the effect of the G observable, which is

associated with the $\sin(2\phi)$ term in equation 6.1.

$$A(\phi) = \frac{N(PARA) - N(PERP)}{N(PARA) + N(PERP)} = P_{lin}\Sigma cos(2\phi) + P_z(P_{lin}Gsin(2\phi)) \qquad (6.5)$$

As there are two polarisation settings for the target, this method will yield two asymmetry distributions per kinematic bin, one for each polarisation state of the target. The effect of the G observable can be seen as a phase shift between the asymmetries for each state of target polarisation, shown in figure 6.14. Again, the data must be scaled to account for the differences in photon polarisation and number of events between PARA and PERP.

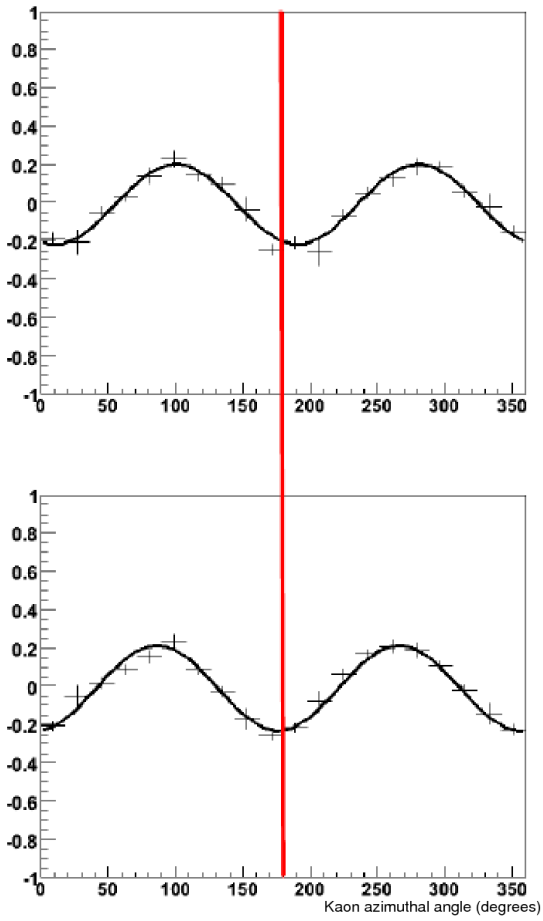

Figure 6.14: Sample PARA/PERP asymmetries for positive (top) and negative (bottom) polarised butanol data. A $\cos(2\phi) + \sin(2\phi)$ fit has been performed on the asymmetries and a phase shift due to the presence of the 'G' observable (associated with the $\sin(2\phi)$ term) can be seen between the two states of target polarisation.

Measurements of $P_\gamma\Sigma$ can be extracted from each asymmetry, from the parameter associated with the $\cos(2\phi)$ term of the fit. These can be combined into one measurement either by producing a weighted mean of the measurement in each target state, or by summing the kaon ϕ distributions for PARA and PERP over the two states of target polarisation, appropriately scaled to account for differences in target polarisation between the target polarisation states. This has the effect of cancelling the G term, as shown in equations 6.6 and 6.7, allowing Σ to be extracted as it would be for an unpolarised target. These methods of extracting Σ on polarised target data are demonstrated in section 6.5.6.

$$\begin{aligned} N(PARA,+z) &= 1 + P_{lin}\Sigma cos(2\phi) - P_z(P_{lin}Gsin(2\phi)) \\ N(PARA,-z) &= 1 + P_{lin}\Sigma cos(2\phi) + P_z(P_{lin}Gsin(2\phi)) \\ N(PARA,sum) &= 1 + P_{lin}\Sigma cos(2\phi) \end{aligned} \tag{6.6}$$

$$\begin{aligned} N(PERP,+z) &= 1 - P_{lin}\Sigma cos(2\phi) + P_z(P_{lin}Gsin(2\phi)) \\ N(PERP,-z) &= 1 - P_{lin}\Sigma cos(2\phi) - P_z(P_{lin}Gsin(2\phi)) \\ N(PERP,sum) &= 1 - P_{lin}\Sigma cos(2\phi) \end{aligned} \tag{6.7}$$

The G observable can also be extracted from each asymmetry distribution using the fit defined by equation 6.5. This extension of the asymmetry technique used for measuring Σ makes the assumption that detector acceptance is unaffected between target polarisation states.

This leaves the problem of having two measurements of G for each kinematic bin, and the issue of measuring G, a beam target observable, on an asymmetry of beam states only. To extract G from a single measurement, a double asymmetry technique was developed, and is discussed below.

6.5.2 The Double Asymmetry Technique

The FROST data has four combinations of polarisation states of beam and target, as opposed to just two beam polarisation states for analyses on an unpolarised target. Their associated kaon ϕ angle distributions are described by equations 6.8. Considering that G is a double polarisation observable of beam and target polarisations, it was decided to attempt to combine all the polarisation combinations into a single measurement of G, by extending the asymmetry technique to reflect the beam-target nature of the G observable.

$$\begin{aligned} N(PARA,+z) &= 1 + P_{lin}\Sigma cos(2\phi) - P_z(P_{lin}Gsin(2\phi)) \\ N(PARA,-z) &= 1 + P_{lin}\Sigma cos(2\phi) + P_z(P_{lin}Gsin(2\phi)) \\ N(PERP,+z) &= 1 - P_{lin}\Sigma cos(2\phi) + P_z(P_{lin}Gsin(2\phi)) \\ N(PERP,-z) &= 1 - P_{lin}\Sigma cos(2\phi) - P_z(P_{lin}Gsin(2\phi)) \end{aligned} \tag{6.8}$$

A fitting technique to a two dimensional distribution of kaon azimuthal angle versus target polarisation was first considered, but quickly rejected due to a lack of bins in target polarisation from the slowly decaying and regularly repolarised target (target polarisations in each direction only vary between 75 and 85%).

A simpler method, measuring G from an asymmetry of kaon azimuthal angle distributions for the two target polarisation states, was also rejected as the cancellation of acceptance from an asymmetry of beam states would be lost, and the issue of having two asymmetries per kinematic bin, this time one for each beam polarisation state, would remain.

This need to retain the acceptance cancellation from an asymmetry of beam polarisation states, as well as the possible effects of target polarisation direction on acceptance, and the desire to use all the data in a single measurement, has led to the development of a double asymmetry technique for the extraction of G.

The double asymmetry constructs the asymmetry of beam polarisation states for each state of target polarisation, then takes an asymmetry of these two asymmetry distributions. For the positive target polarisation setting, the asymmetry fit function

has the following form (compare with equation 6.5);

$$A(\phi, +z) = P_{lin}\Sigma cos(2\phi) + P_z(P_{lin}Gsin(2\phi)) \tag{6.9}$$

And for the negative target polarisation setting;

$$A(\phi, -z) = P_{lin}\Sigma cos(2\phi) - P_z(P_{lin}Gsin(2\phi)) \tag{6.10}$$

The double asymmetry is constructed as follows;

$$A(\phi) = \frac{A(\phi, +z) - A(\phi, -z)}{A(\phi, +z) + A(\phi, -z)} \tag{6.11}$$

where $A(\phi, \pm z)$ are the PARA/PERP asymmetries for each state of target polarisation. For the simple case where the polarisations of the beam and the target do not change with polarisation mode, equation 6.11 can be described by a $\tan(2\phi)$ function;

$$A(\phi) = \frac{2P_\gamma P_z Gsin(2\phi)}{2P_\gamma \Sigma cos(2\phi)} = \frac{P_z G}{\Sigma} tan(2\phi) \tag{6.12}$$

To test the feasibility of extracting polarisation observables from such a double asymmetry, a phase space event generator [85] was used to produce high statistics sample data with known values of the Σ and G observables, and identical values of the beam and target polarisations for each of the four combinations of polarisation states. A double asymmetry was constructed and a fit function of the form of equation 6.12 used to extract the two observables.

Figure 6.15 shows the result of a simple test for 40 million events (10 million for each combination of polarisation states), where $\Sigma = 0.5$, G = 0.8, and beam and target polarisations are 100%. The fit function is able to extract these defined values with negligible errors and with no constraints on any of the variables.

The g9a data for the kaon channels is far from the simple situation described above. A limited number of hyperon events are available, with mean polarisations that vary between the combinations of beam and target polarisation states. These effects and others, such as the presence of bound nucleon events, act to make the

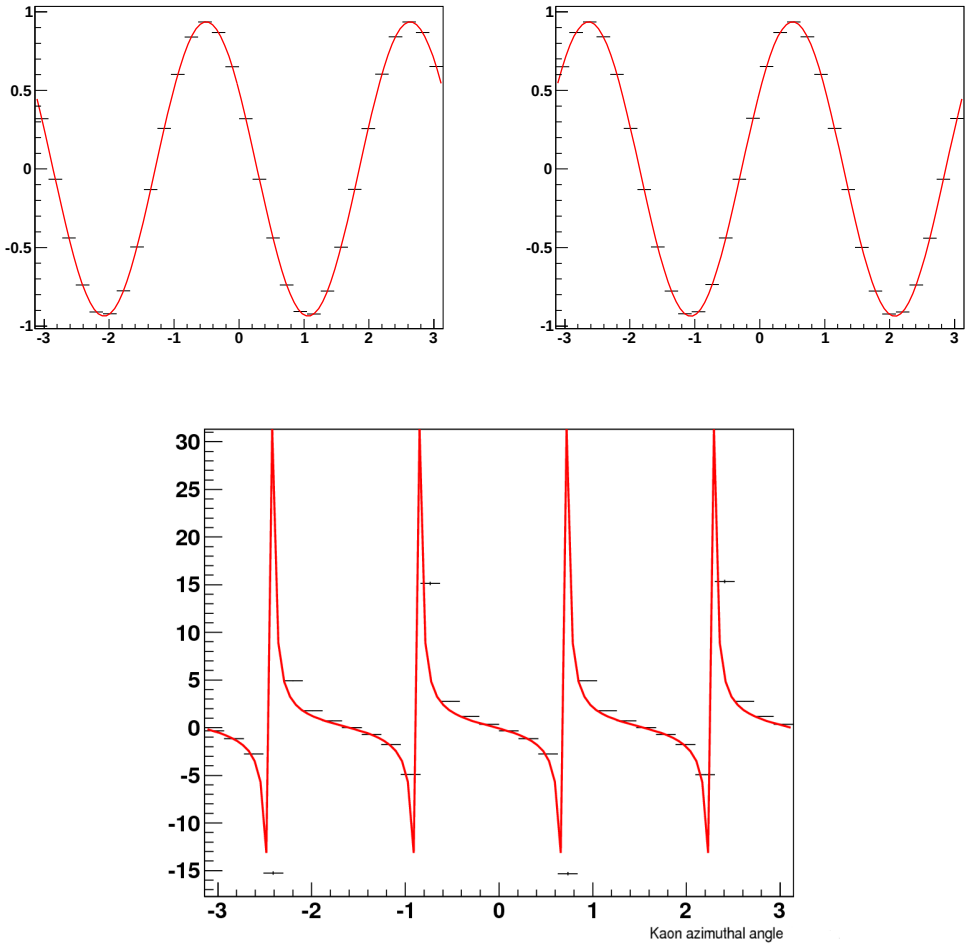

Figure 6.15: Construction of a double asymmetry from sample beam asymmetries for the positive (top left) and negative (top right) states of target polarisation from simulated data. No constraints were required on the double asymmetry fit to extract the simulated values of the Σ and G observables.

description of the resulting double asymmetry as a $\tan(2\phi)$ function invalid.

Construction of a fit function for more realistic situations would have too many parameters to feasibly constrain the fit and obtain values of G, and instead the data is appropriately scaled to account for these differences, as it was for the Σ extraction on beam asymmetries.

When fitting to data, the value of the parameter associated with $P_\gamma\Sigma$ is constrained to the measured values from the regular asymmetry described in the previous subsection. This reduces the error in the extraction of G from the double asymmetry, as the Σ observable is no longer a free parameter in the fit, and correlation effects between the Σ and G parameters should be eliminated.

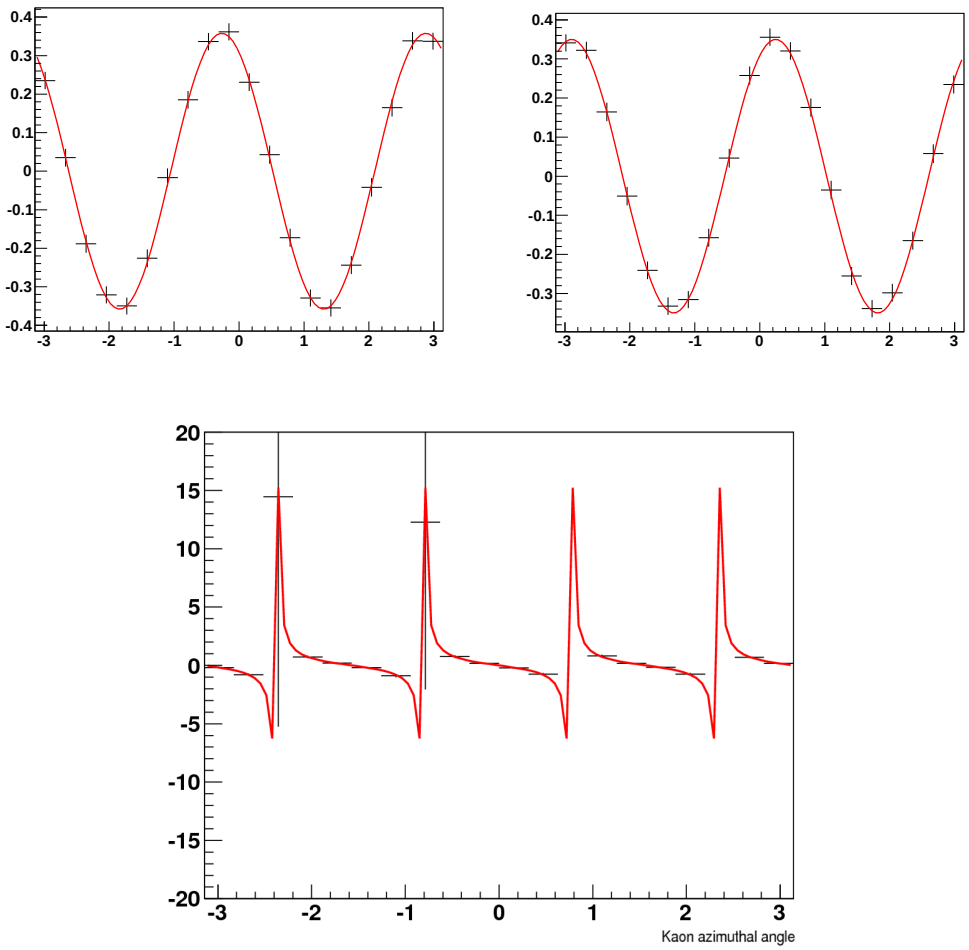

Figure 6.16: Construction of a double asymmetry for low statistics simulated data. The double asymmetry fit must now be constrained by the value of Σ extracted from the two beam asymmetries in order to extract the simulated value of the G observable.

A test of the double asymmetry fit on more realistic simulated data, with 20,000 events per polarisation state, is shown in figure 6.16. The parameter associated with $P_\gamma\Sigma$ is constrained to the mean value determined by $\cos(2\phi)$ + $\sin(2\phi)$ fits to the PARA/PERP beam asymmetries of the generated events for the two target states.

Both the double asymmetry technique, constrained by the Σ measurements on butanol, and the alternative extraction of G from the $\cos(2\phi)$ + $\sin(2\phi)$ fits for each target polarisation state, will be used in this analysis.

Both techniques have limitations, with the extraction of G from the $\cos(2\phi)$ + $\sin(2\phi)$ fits open to large systematic uncertainties, given its simultaneous extraction with Σ and its manifestation as a phase shift in the asymmetry distribution. Although the potential acceptance issues between target states and the return of a single measurement per kinematic bin make the double asymmetry an attractive proposition for the extraction of G, correlation effects between the Σ and G observables are significant without adequate constraint on Σ from other measurements.

6.5.3 Determination of ϕ_0

One potential source of systematic uncertainty in the extraction of polarisation observables via the asymmetry and double asymmetry techniques is associated with the accuracy of the alignment of the diamond in the goniometer. A small angular offset in the diamond orientation will manifest as a phase offset, ϕ_0, as the PARA and PERP photon polarisations will not be exactly aligned with their defined directions.

The diamond was aligned at the start of the experiment, and its angular offset remains fixed throughout the run. The offset also remains fixed regardless of energy or kaon polar angle (θ), and as such its measurement is made over all kinematic bins in W and θ^{K+}_{CM} to maximise the statistics used in the measurement.

Ideally, a high statistics channel, such as $\gamma p \rightarrow p\pi^0$ or $\gamma p \rightarrow n\pi^+$, would be used to determine ϕ_0 for the entire experiment, this makes the assumption that the phase offset is independent of the reaction channel. As a measurement on a high statistics pion channel was not available at time of writing, the offset was determined from the data on the strangeness channels.

This determination of ϕ_0 is made for each target individually, as their different

z-vertex positions may effect any offset angle determined, as will the presence of target polarisation in butanol, given that the G observable also acts as a phase shift in the kaon ϕ distributions.

For the unpolarised targets, determining ϕ_0 is a simple matter of including an extra parameter on the $\cos(2\phi)$ fit for the asymmetry of the kaon ϕ distributions, over all W and θ^{K+}_{CM} bins.

For the polarised butanol, ϕ_0 is measured by first adding the kaon ϕ distributions for each state of target polarisation, normalised to account for the different values of polarisation in each direction. This should cancel the effect of the G observable and ϕ_0 is extracted as it was for the unpolarised target. This cancellation of the G term will introduce some systematic uncertainty in the measurement of ϕ_0 for butanol, but is necessary as the manifestation of G as a phase shift in the PARA/PERP asymmetry would make a ϕ_0 measurement much harder.

The values of ϕ_0 measured for each target and reaction channel are shown in table 6.4. For carbon and polythene, these values are small and will have very little effect on the measurements of observables on these targets. For butanol, the values are much larger, underlining the difficulty in separating the offset angle from the G observable in an asymmetry of beam polarisation states.

Target Material	Phase offset angle for $K^+\Lambda$	Phase offset angle for $K^+\Sigma$
Carbon	-0.034±0.045	-0.017±0.050
Polythene	-0.115±0.055	-0.063±0.055
Butanol	-0.250±0.10	-0.153±0.051

Table 6.4: Phase offset angles for the three targets in FROST, for both the $K^+\Lambda$ and $K^+\Sigma^{)}$ reactions. Due to limited statistics on the carbon target, and difficulty separating the phase offset from the G polarisation observable on the polarised butanol target, only the polythene data is used to determine the phase offset.

Due to the difficulty in separating the G observable from the phase offset on the polarised target, the butanol data was not used in the determination of ϕ_0. Furthermore, because of the severely limited number of events available on the carbon target, the measured ϕ_0 values on carbon are also not used, leaving the polythene target as the only data used to measure ϕ_0.

Having determined a value of ϕ_0, it can now be included as a fixed parameter in

the fit functions used for extracting observables, reducing one source of systematic uncertainty in the final results.

6.5.4 Extraction of $P_\gamma\Sigma$ on Carbon

The quantity extracted from a $\cos(2\phi)$ fit on the PARA/PERP asymmetry of polythene data is a simultaneous measurement of $P_\gamma\Sigma$ for both the molecular protons in polythene and its carbon nuclei. This is also the case for the PARA/PERP asymmetry on butanol, where $P_\gamma\Sigma$ is the parameter associated with the cosine term in a $\cos(2\phi) + \sin(2\phi)$ fit.

In order to compute a value of $P_\gamma\Sigma$ for the molecular proton on both these targets, measurements of $P_\gamma\Sigma$ for the carbon data are required, using the same kinematic bins as used on the polythene and butanol targets.

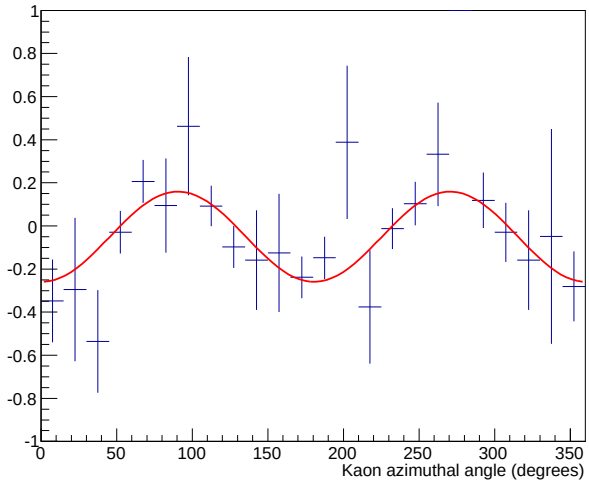

Figure 6.17: $cos(2\phi)$ fit to the asymmetry of beam polarisation states on the carbon data. $P_\gamma\Sigma$ for carbon is extracted from the magnitude of the fit.

The extraction of carbon from a $\cos(2\phi)$ fit to an asymmetry of PARA and PERP events from the carbon target is shown in figure 6.17. These measurements are used in conjunction with the carbon scaling factors to calculate $P_\gamma\Sigma$ for the molecular proton in polythene and butanol, which will be shown in the following subsections.

6.5.5 Extraction of Σ on Polythene

For the polythene data, a $\cos(2\phi)$ fit is performed on the PARA/PERP asymmetry of kaon ϕ distributions in order to extract an overall value of $P_\gamma\Sigma$ for polythene. This value, which will be referred to as $P_\gamma\Sigma_{polythene}$, is a measurement of two things; $P_\gamma\Sigma_{proton}$ associated with the molecular protons in the target, and $P_\gamma\Sigma_{carbon}$, which is contribution from the bound nucleons from the carbon present in polythene. These two contributions contribute to $P_\gamma\Sigma_{polythene}$ as follows;

$$P_\gamma\Sigma_{Polythene} = P_\gamma\left(\frac{N_{Proton}}{N_{Proton}+N_{Carbon}}\Sigma_{Proton} + \frac{N_{Carbon}}{N_{Proton}+N_{Carbon}}\Sigma_{Carbon}\right) \quad (6.13)$$

Where N_{Proton} is the number of events corresponding to interactions with a molecular proton in the target, estimated by subtracting the number of events on the carbon target in the same bin, multiplied by the carbon scaling factor for polythene, from the total number of events in the bin for polythene, $N_{Polythene}$ is the number of polythene events, N_{Carbon} is the carbon events, scaled by the carbon scaling factor for polythene, P_γ is the degree of photon polarisation, and Σ_{Proton}, $\Sigma_{Polythene}$ and Σ_{Carbon} are the beam polarisation observable on the molecular proton, the polythene target and carbon nuclei respectively.

By rearranging equation 6.13, a value of $P_\gamma\Sigma$ for the molecular proton can be estimated from the measured values of $P_\gamma\Sigma_{Polythene}$, $P_\gamma\Sigma_{Carbon}$, and the carbon scaling factor.

$$P_\gamma\Sigma_{Proton} = \left(\frac{1}{N_{Proton}}\right)(N_{Polythene}P_\gamma\Sigma_{Polythene} - N_{Carbon}P_\gamma\Sigma_{Carbon}) \quad (6.14)$$

The measured value of photon polarisation can then be divided off in order to arrive at a value of Σ for the molecular proton. The limited available data on the polythene and carbon targets mean that large statistical uncertainties are present in the measurement. These errors will be smaller for measurements on the butanol target, which has more data available, although the limited carbon data will act

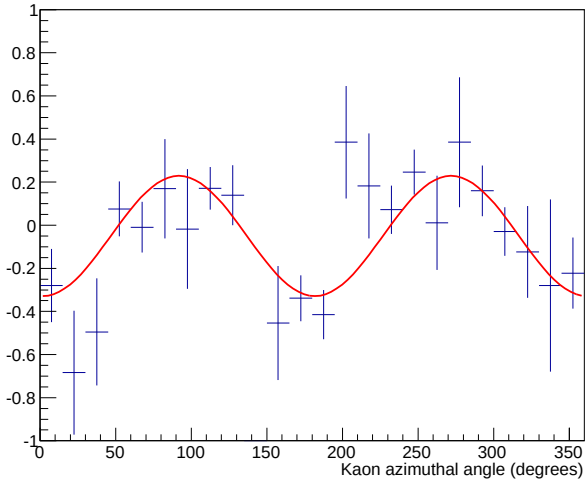

Figure 6.18: $cos(2\phi)$ fit to the asymmetry of beam polarisation states on the polythene data. $P_\gamma\Sigma$ for polythene is extracted from the magnitude of the fit. Further analysis is required to extract a value for the molecular protons in the target.

against the possible error reduction.

6.5.6 Extraction of Σ on Butanol

As section 6.5.1 describes, the presence of polarised molecular protons in the butanol target is accounted for by modifying the $\cos(2\phi)$ fit used for the unpolarised targets to deal with the effects of the G observable. The new fit is based on a $\cos(2\phi)$ + $\sin(2\phi)$ function, where $P_\gamma\Sigma$ is the parameter associated with the $\cos(2\phi)$ term.

Fits are performed on the butanol data for each kinematic bin and for each polarisation state of the target, giving two $P_\gamma\Sigma$ measurements per bin. Because the Σ observable is independent of G, these measurements can be combined into a single measurement, by producing a weighted mean of the two measurements.

As with the determination of ϕ_0 on butanol, the phase shift induced by the G observable can be cancelled by summation of the kaon ϕ distributions over the two target polarisation states, and a $\cos(2\phi)$ fit performed to extract one $P_\gamma\Sigma$ measurement per bin. As before, the distributions must be normalised first to account for the differences in target polarisation in order to properly cancel the $\sin(2\phi)$ associated with the G observable.

The resulting measurements of $P_\gamma\Sigma_{butanol}$ has the same nature as those made

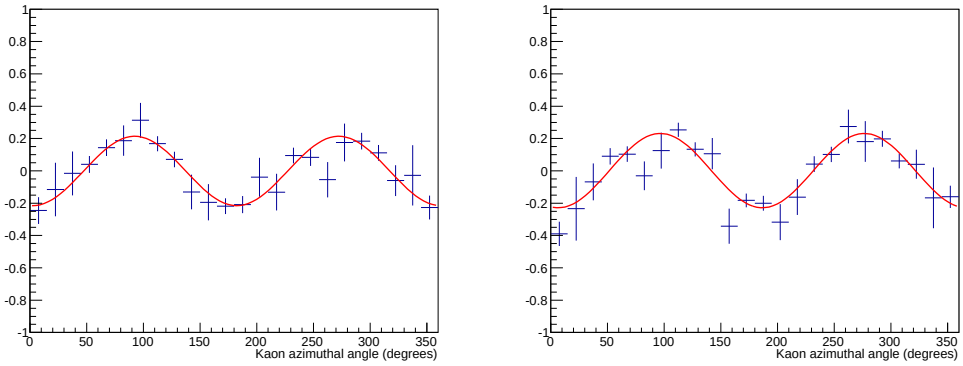

Figure 6.19: $cos(2\phi) + sin(2\phi)$ fit to the asymmetry of beam polarisation states for the two target polarisation states of butanol. $P_\gamma\Sigma$ for butanol is extracted from the magnitude of the $cos(2\phi)$ term. Further analysis is required to combine these measurements and extract a value for the molecular protons in the target.

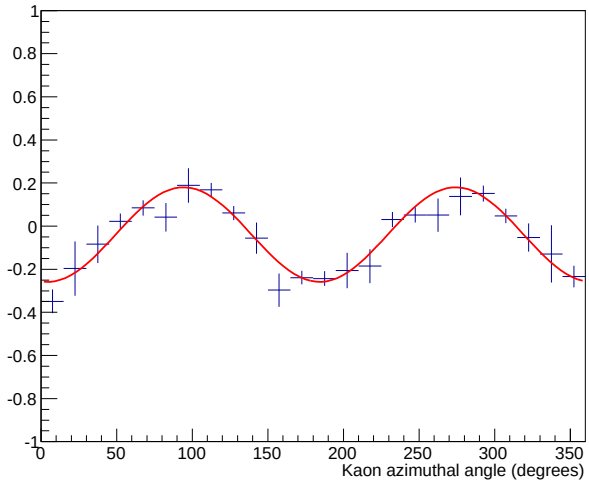

Figure 6.20: $cos(2\phi)$ fit to the asymmetry of beam polarisation states for the summation of the two target polarisation states of butanol. $P_\gamma\Sigma$ for butanol is extracted from the magnitude of the fit. Further analysis is required to extract a value for the molecular protons in the target.

on polythene, with contributions to the measurement from molecular protons and bound nucleons. These are handled in the same way as they were for polythene in order to arrive at a value of $P_\gamma\Sigma_{proton}$ for the butanol data, and the analogous expression to equation 6.14 for the butanol target is given by;

$$P_\gamma\Sigma_{Proton} = \left(\frac{1}{N_{Proton}}\right)(N_{Butanol}P_\gamma\Sigma_{Butanol} - N_{Carbon}P_\gamma\Sigma_{Carbon}) \qquad (6.15)$$

Where the symbols have similar meanings as before, and the butanol carbon scaling factors are used to scale the carbon measurements instead of those for polythene.

6.5.7 Extraction of G

For completeness, both methods described to measure the G observable; the cos(2ϕ) + sin(2ϕ) fit, where the sin(2ϕ) term is associated with $P_\gamma P_{Target} G$, and the double asymmetry technique, were used. As with the Σ measurements, the cos(2ϕ) + sin(2ϕ) fit will return two measurements of G for each kinematic bin.

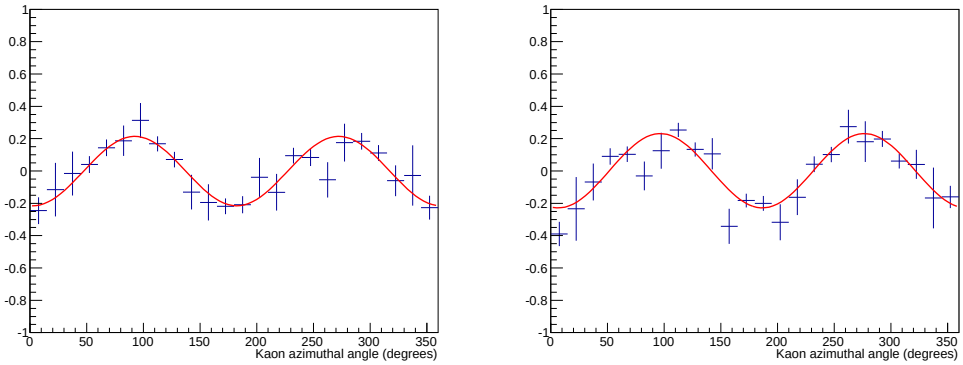

Figure 6.21: $cos(2\phi) + sin(2\phi)$ fit to the asymmetry of beam polarisation states for the two target polarisation states of butanol. $P_\gamma P_{Target} G$ is extracted from the magnitude of the $sin(2\phi)$ term. Further analysis is required to extract a value of G for the molecular protons in the target.

For the G observable, there is no contribution to $P_\gamma P_{Target} G$ from the carbon in butanol, as carbon nuclei are spin zero and hence unpolarisable. This makes handling dilution of the G observable somewhat simpler than for Σ;

$$P_\gamma P_{Target} G_{Proton} = \left(\frac{N_{Butanol}}{N_{Proton}} \right) P_\gamma P_{Target} G_{Butanol} \tag{6.16}$$

Where N_{Proton}, $N_{Butanol}$, and N_{Carbon} have the same meanings as in equation 6.15, P_γ is the degree of photon polarisation, P_{Target} is the degree of polarisation of the target, and G_{Proton} and $G_{Butanol}$ are the G polarisation observable for the molecular proton and on butanol.

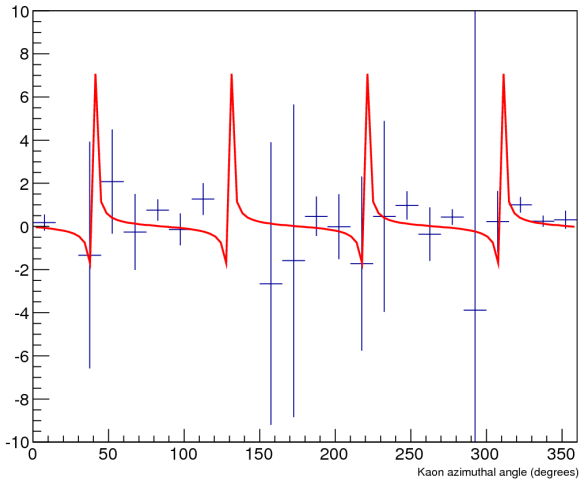

Figure 6.22: Extraction of $P_\gamma P_{Target} G$ from the double asymmetry technique. Large statistical uncertainties arise in the fit due to lack of available data. Further analysis is required to extract a value for the molecular protons in the target.

6.6 Summary

Two polarisation observables, Σ and G, have been measured for the reactions $\gamma p \rightarrow K^+\Lambda$ and $\gamma p \rightarrow K^+\Sigma^0$. For the Σ observable, these measurements have been made on both the unpolarised polythene and polarised butanol targets, and it has been demonstrated that the presence of target polarisation does not hamper such a measurement.

The G beam-target double observable was measured on the polarised target via two techniques, from the phase shift induced by the G observable in beam asymmetry measurements, and the novel double asymmetry method developed by the author.

The dilution effects of bound nucleons in the target material has been accounted for in the extraction of both these observables from the data, with the Σ measurement further complicated by an extra term in the dilution expression corresponsing to the ability to measure the Σ observable on carbon.

The next chapter will present the full results of this analysis, and comparisons will be made with previous data and theoretical predictions.

Chapter 7

Results and Discussion

This final chapter will present the results of the analysis described in the preceding chapters of this thesis. To recap, two polarisation observables, Σ and G, were measured for the reactions $\gamma p \rightarrow K^+\Lambda^0$ and $\gamma p \rightarrow K^+\Sigma^0$. The Σ results will be compared to those from a previous JLab analysis and, in the absence of data to compare the G results with, available model predictions will be used.

All results shown only display statistical errors for the quantities measured, with the main systematic errors being 10% in photon polarisation and 5% from the respective determinations of the dilution of the Σ and G observables in the target materials used. Additionally, the g8b data shown to compare with the Σ measurements has an associated 5% systematic uncertainty in photon polarisation not included in the error bars for the relevant plots.

7.1 Photon Asymmetry (Σ) Results

The Σ observable results on the polythene target are shown for each energy bin for the $K^+\Lambda$ channel as a function of kaon centre-of-mass angle ($cos\theta^{K+}_{cm}$) in figure 7.1 and for the butanol target, as a weighted mean of the result for each state of target polarisation, in figure 7.2. The butanol results are also compared with preliminary data from the g8b experiment at JLab, rebinned to the same kinematic bins used in the analysis [86] in figure 7.3.

Corresponding results for $K^+\Sigma^0$ on the polythene and butanol targets are shown

in figures 7.4 and 7.5.

7.2 Discussion of Photon Asymmetry Results

Despite the large statistical errors, agreement can be seen between the polythene and butanol data, for both the $K^+\Lambda$ and $K^+\Sigma$ results. The comparison between the butanol results and the rebinned g8b data in figure 7.3 for $K^+\Lambda$ shows the g9a results largely agree with this previous CLAS measurement, with the differences due to systematic uncertainties resulting from the target material, particularly in calculating the dilution in the asymmetry measurement associated with the presence of bound nucleons in the target material, as well as systematic effects in the photon and target polarisations. Photon polarisations for both the g8b and g9a experiments are still being studied, and the associated systematic uncertainties are not fully determined at this time.

For $K^+\Sigma$, rebinned data from the g8b experiment was not available at time of writing, and the preliminary results from the PhD thesis of C. Paterson [39], with different kinematic binning, are shown instead for this channel. The first two plots in figure 7.6 correspond to the W = 1.715 GeV bin of g9a results, with the g9a energy bins corresponding to the subsequent groups of four g8b plots, until the W = 2.195 GeV bin, which overlaps the final two plots in figure 7.6. Although not directly comparable, the g9a data appears to reproduce the same broad features in the Σ observable for $K^+\Sigma$ as g8b, but rebinned g8b data would be required to verify this properly.

7.3 Beam-Target Observable, G

The G observable results are shown for the same binning in energy and $cos\theta^{K+}_{cm}$ as the Σ results. Figure 7.7 shows the raw measurement of $P_\gamma P_{target} G$ from $K^+\Lambda$ on butanol, from which the dilution and polarisations are accounted for to produce a value of G for each state of target polarisation, shown in figure 7.8. A weighted mean value of G is calculated from the values obtained for the two target polarisation

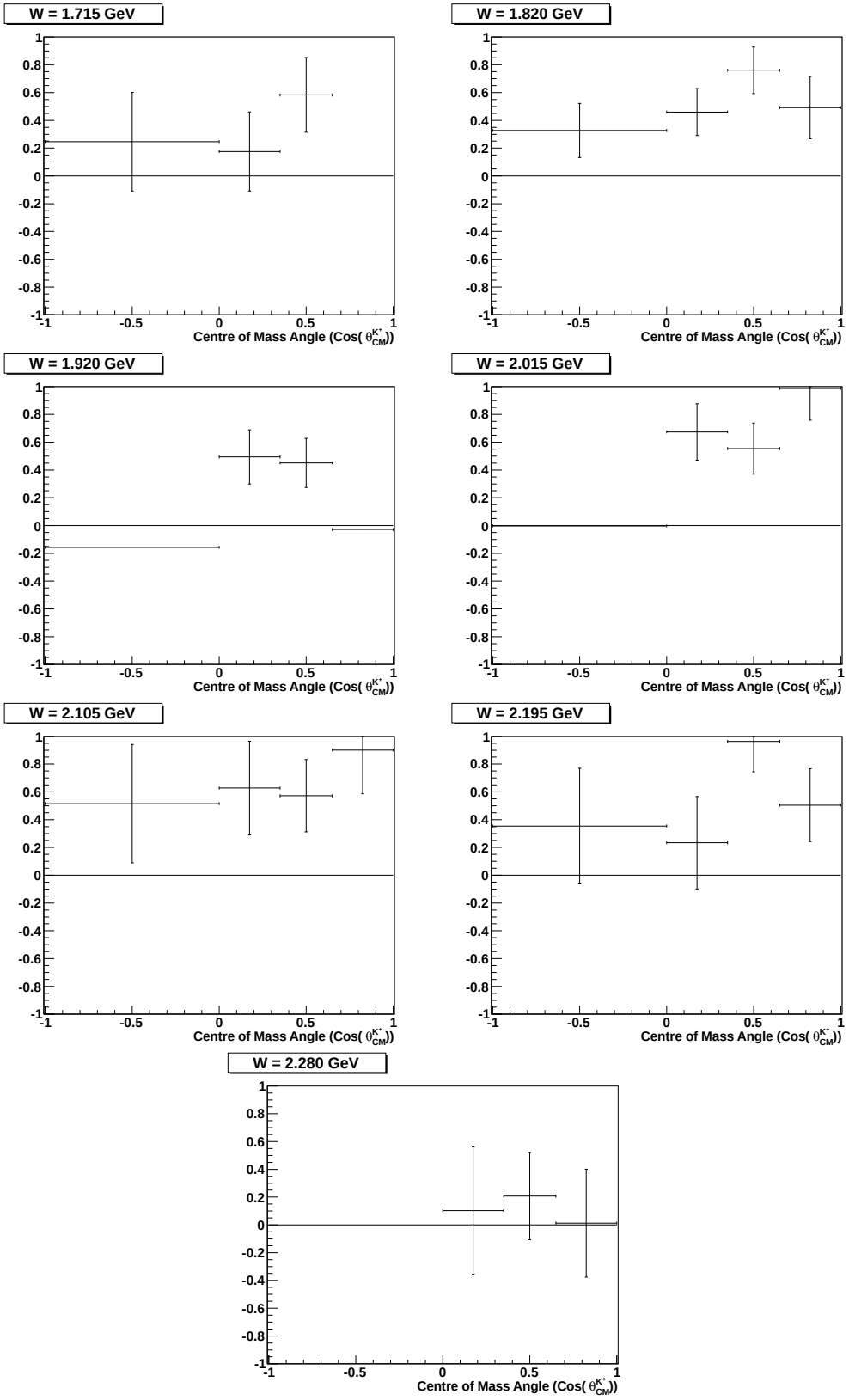

Figure 7.1: Photon asymmetry on polythene for $K^+\Lambda$ as a function of $cos(\theta^{K+}_{cm})$ for W = 1.715 to 2.280 GeV.

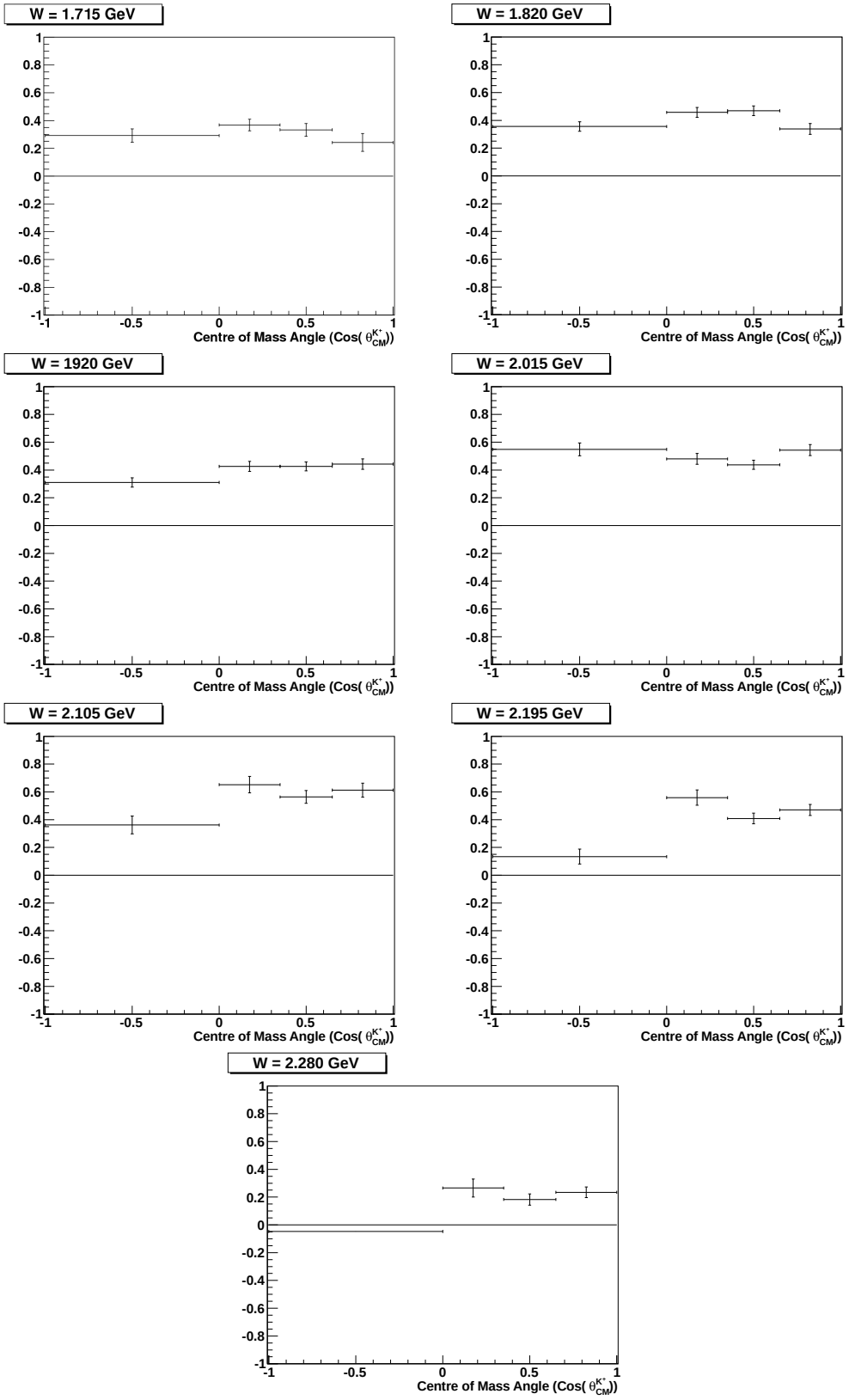

Figure 7.2: Photon asymmetry on butanol for $K^+\Lambda$ as a function of $cos(\theta^{K+}_{cm})$ for W = 1.715 to 2.280 GeV.

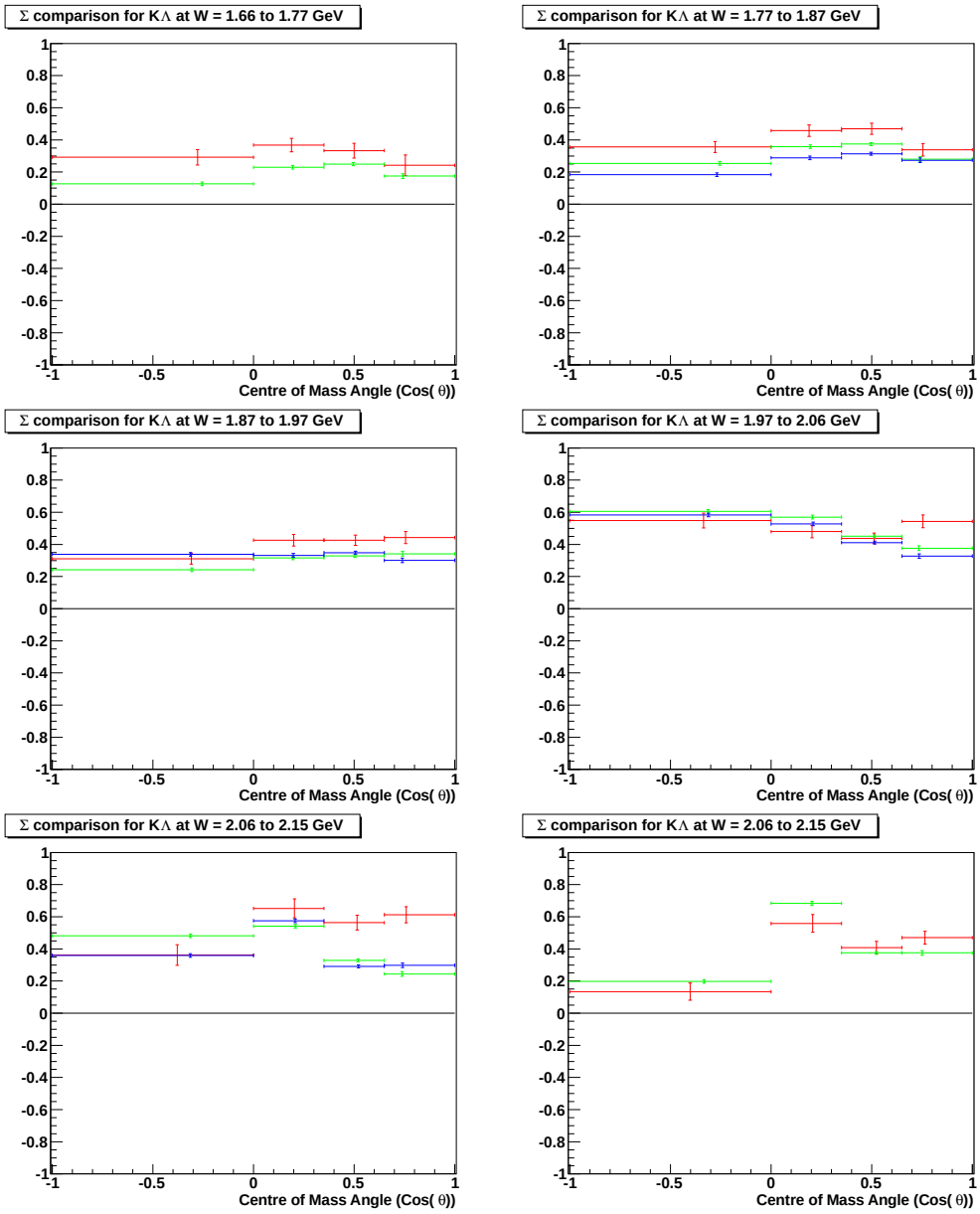

Figure 7.3: Comparison of g8b and g9a photon asymmetries for $K^+\Lambda$ as a function of $cos(\theta^{K+}_{cm})$ for W = 1.715 to 2.280 GeV. Red lines indicate the g9a data, green and blue lines indicate the corresponding W bin from g8b for adjacent coherent peak settings around the W bin.

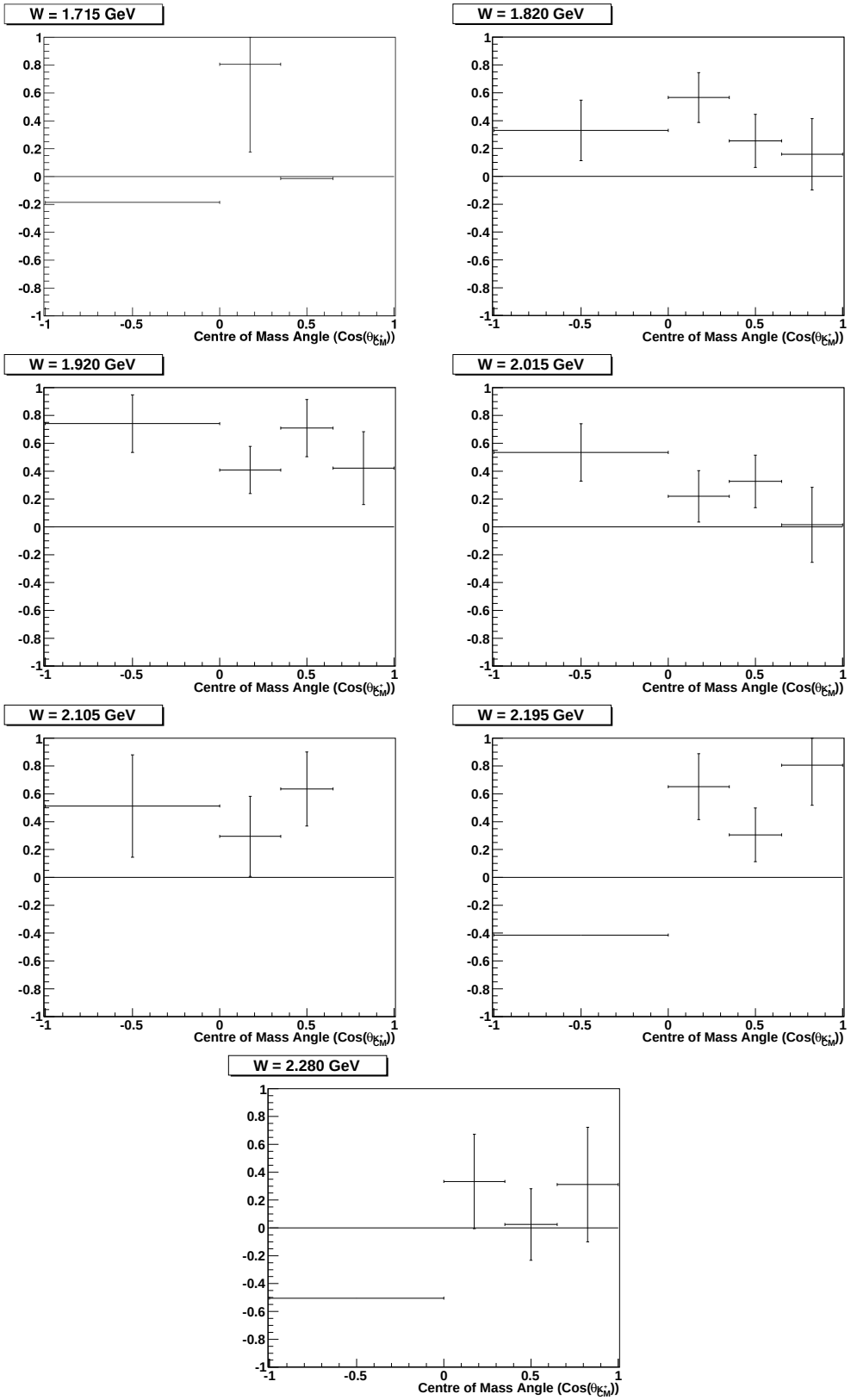

Figure 7.4: Photon asymmetry on polythene for $K^+\Sigma$ as a function of $cos(\theta^{K+}_{cm})$ for W = 1.715 to 2.280 GeV.

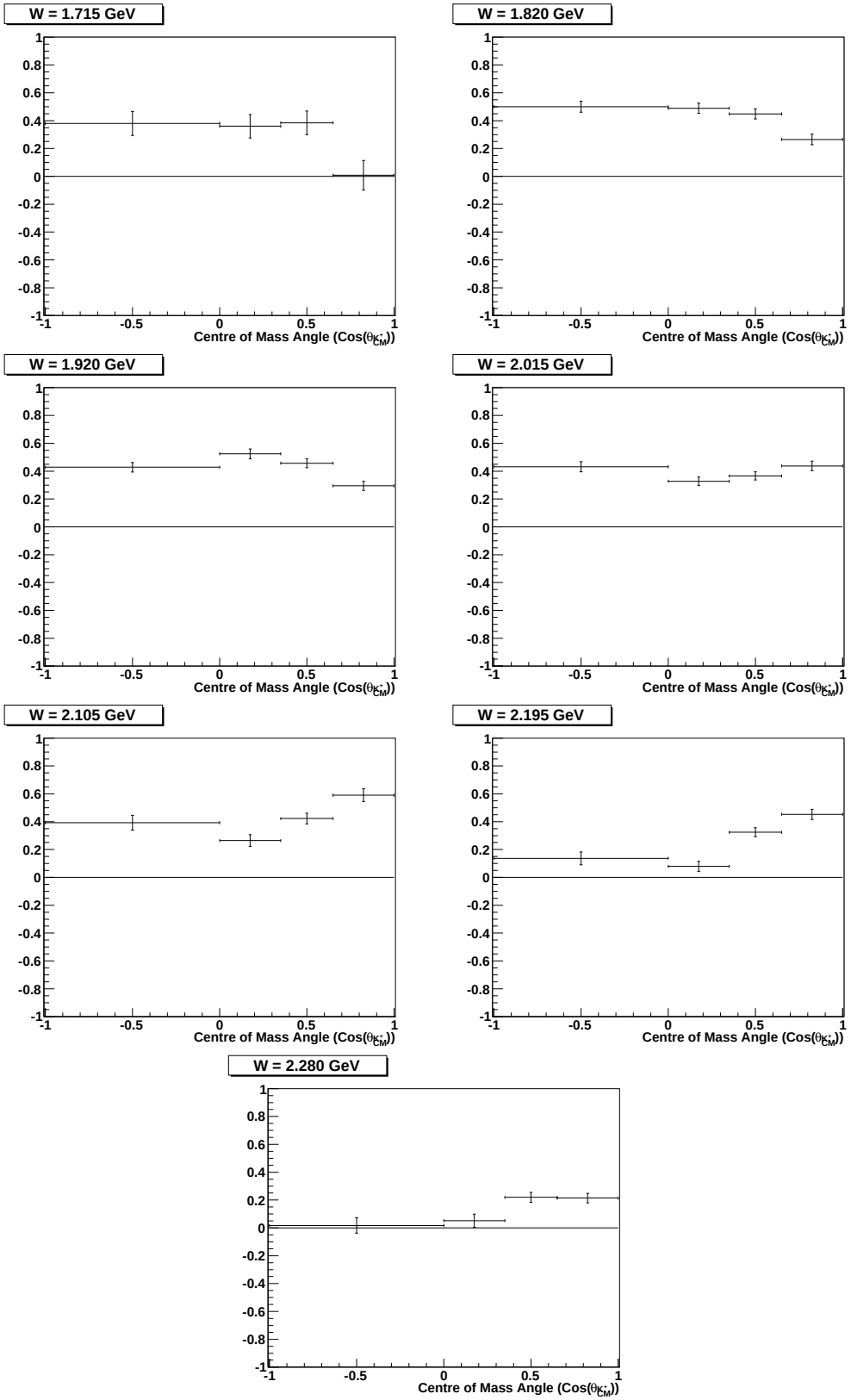

Figure 7.5: Photon asymmetry on butanol for $K^+\Sigma$ as a function of $cos(\theta^{K+}_{cm})$ for W = 1.715 to 2.280 GeV.

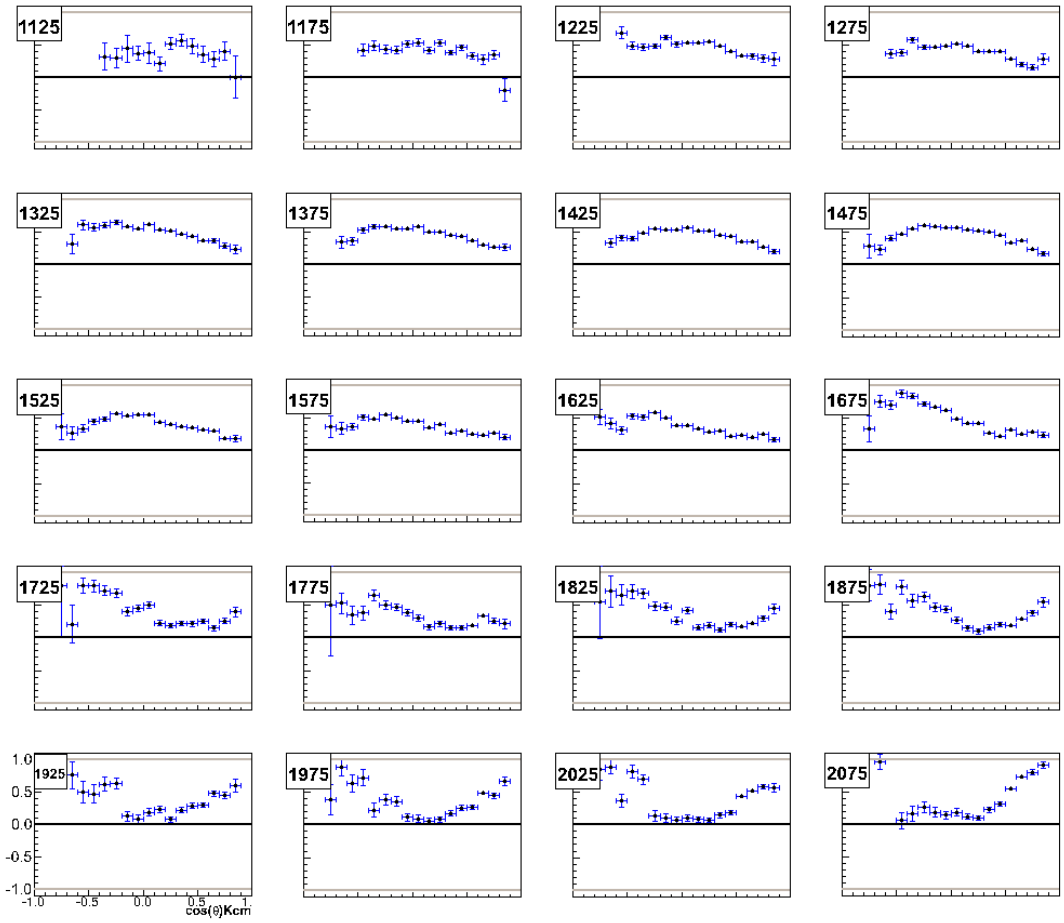

Figure 7.6: Preliminary measurements of the beam polarisation observable (Σ) for the reaction $\gamma p \rightarrow K^+\Sigma^0$ as a function of $cos\theta^{K+}_{cm}$ from the g8b experiment at CLAS [39] for a series of photon energy bins ranging from $E_\gamma = 1.125$ to 2.075 GeV. These energies are displayed in MeV in the boxes at the top left of each plot.

states, shown in figure 7.9. Finally, the G measurement for $K^+\Lambda$ from the double asymmetry technique described in the previous chapter is shown in figure 7.10. Figures 7.11 to 7.14 show the corresponding plots for the $K^+\Sigma^0$ channel.

The mean G results from the two target states for $K^+\Lambda$ are compared with the Kaon-MAID predictions for G, with and without the inclusion of a $D_{13}(1900)$ resonance in figure 7.15, and the $K^+\Sigma$ results compared with a Kaon-MAID line in figure 7.16.

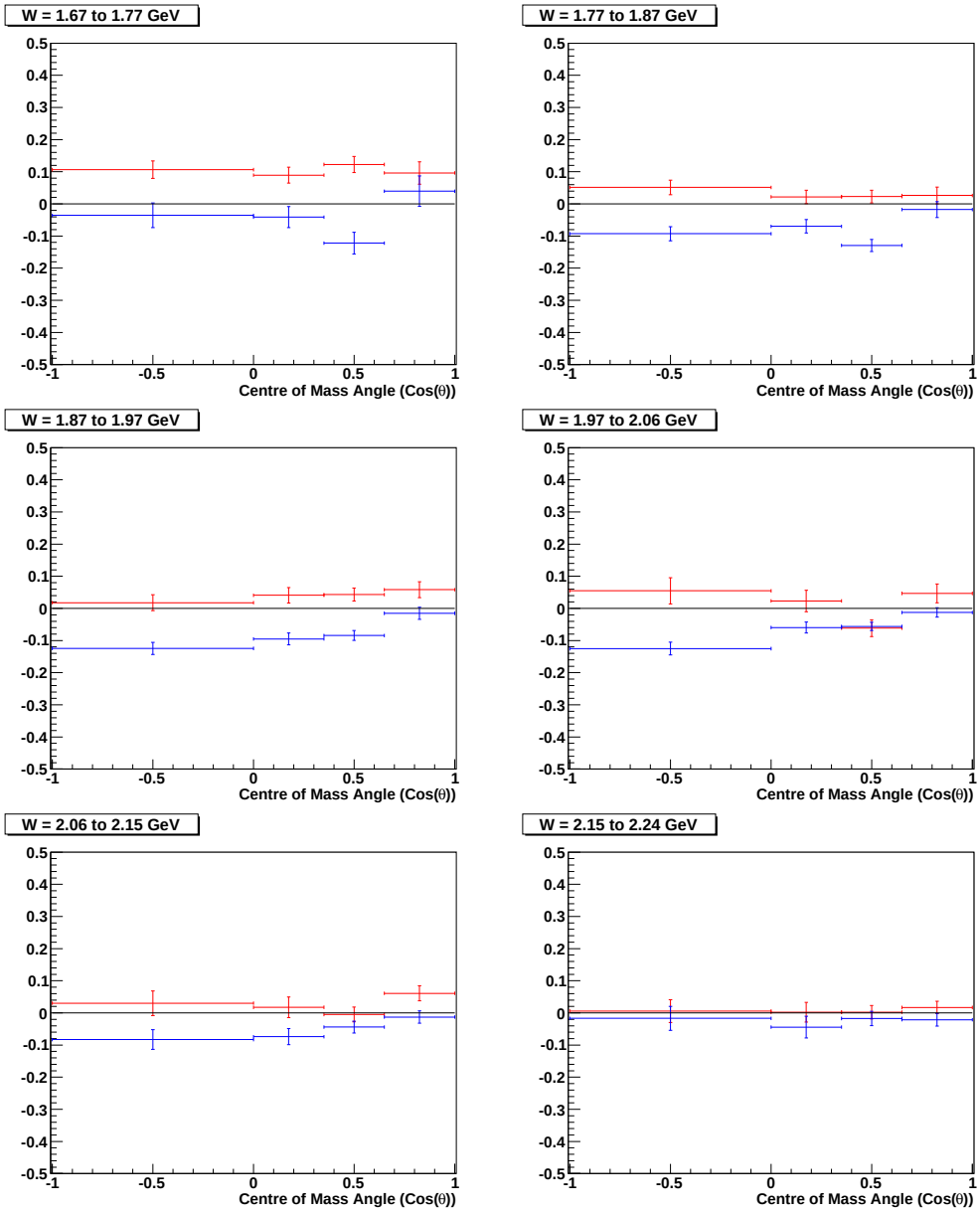

Figure 7.7: $P_\gamma P_{target} G$ for $K^+\Lambda$ as a function of $cos(\theta^{K^+}_{cm})$ for W bin centres ranging from 1.715 to 2.195 GeV. Red points indicate the positively polarised target and blue points the negatively polarised target.

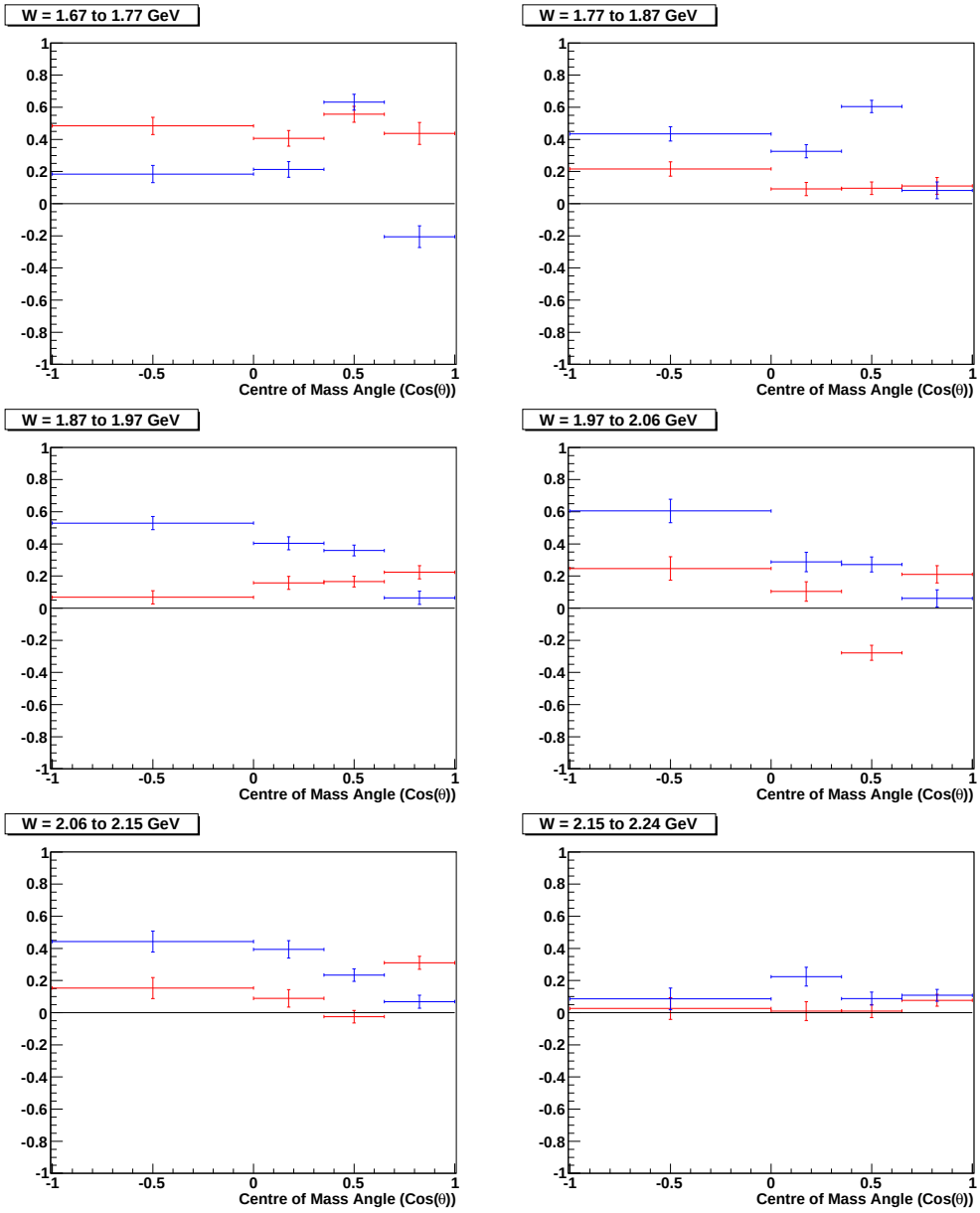

Figure 7.8: G observable for $K^+\Lambda$ as a function of $cos(\theta^{K+}_{cm})$ for W bin centres ranging from 1.715 to 2.195 GeV. Red points indicate the positively polarised target and blue points the negatively polarised target.

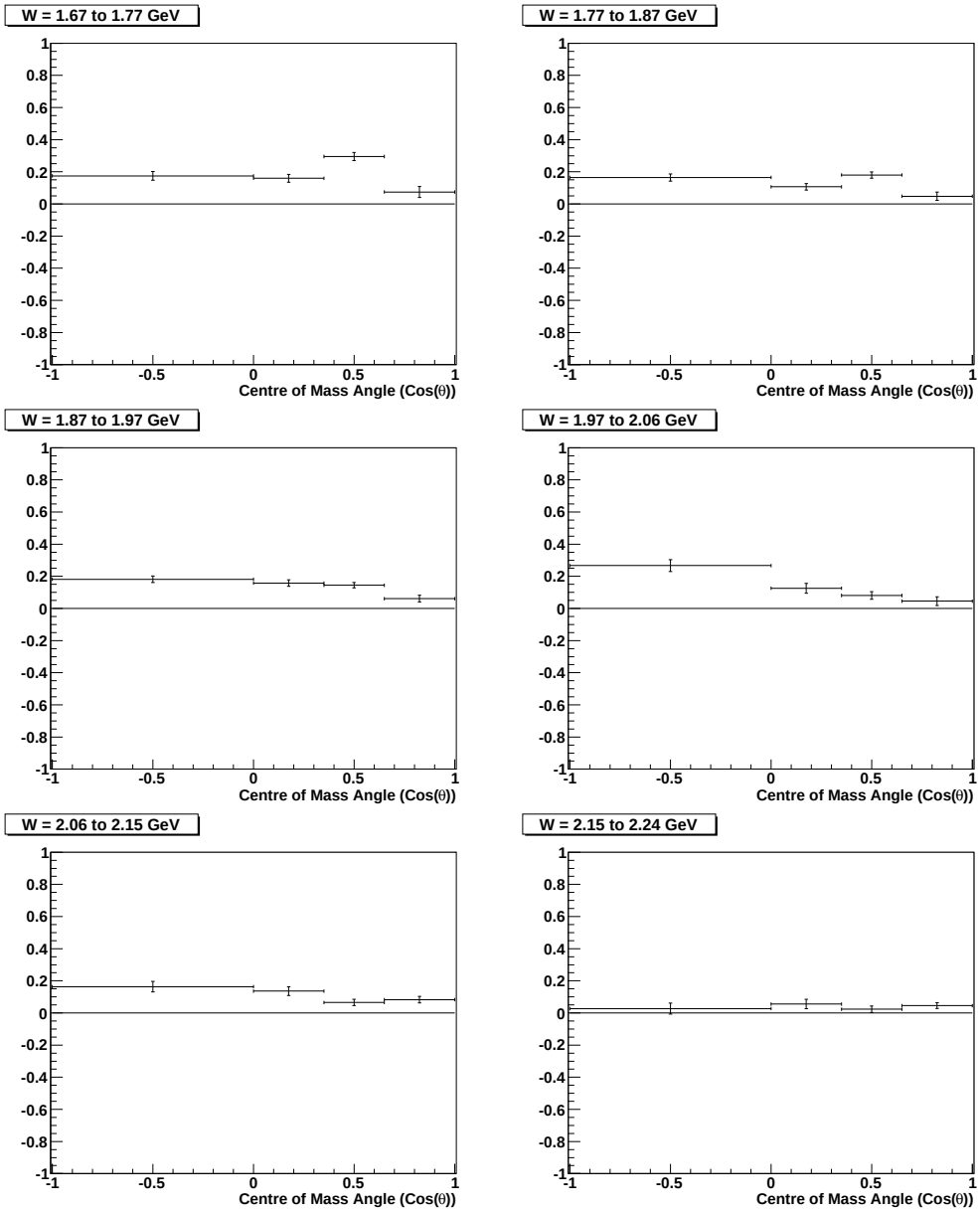

Figure 7.9: Mean of the positive and negative G observable measurements for $K^+\Lambda$ as a function of $cos(\theta^{K+}_{cm})$ for W bin centres ranging from 1.715 to 2.195 GeV.

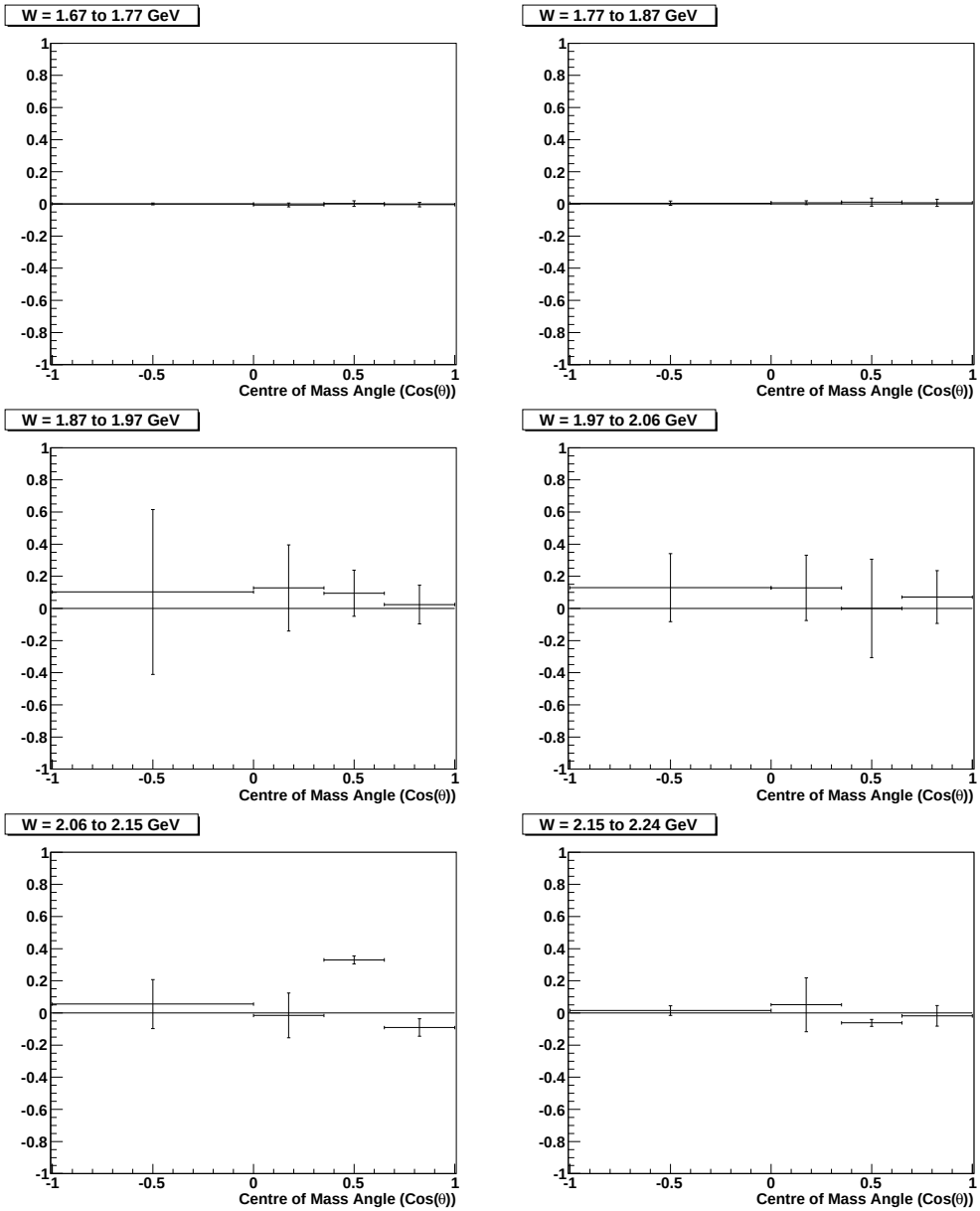

Figure 7.10: G observable for $K^+\Lambda$ from the double asymmetry as a function of $cos(\theta^{K+}_{cm})$ for W bin centres ranging from 1.715 to 2.195 GeV.

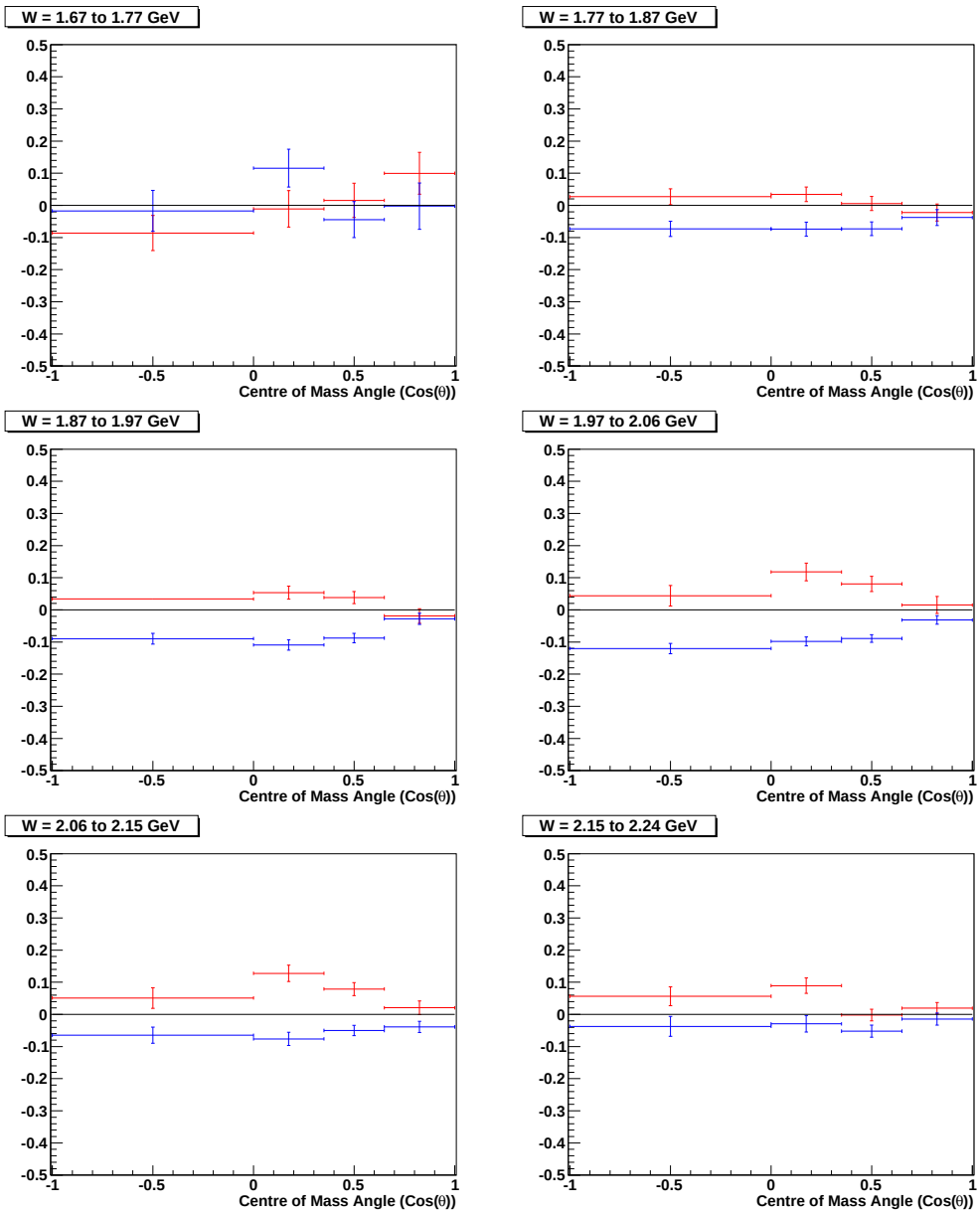

Figure 7.11: $p_{\gamma}p_{target}G$ for $K^{+}\Sigma$ as a function of $cos(\theta^{K+}_{cm})$ for W bin centres ranging from 1.715 to 2.195 GeV. Red points indicate the positively polarised target and blue points the negatively polarised target.

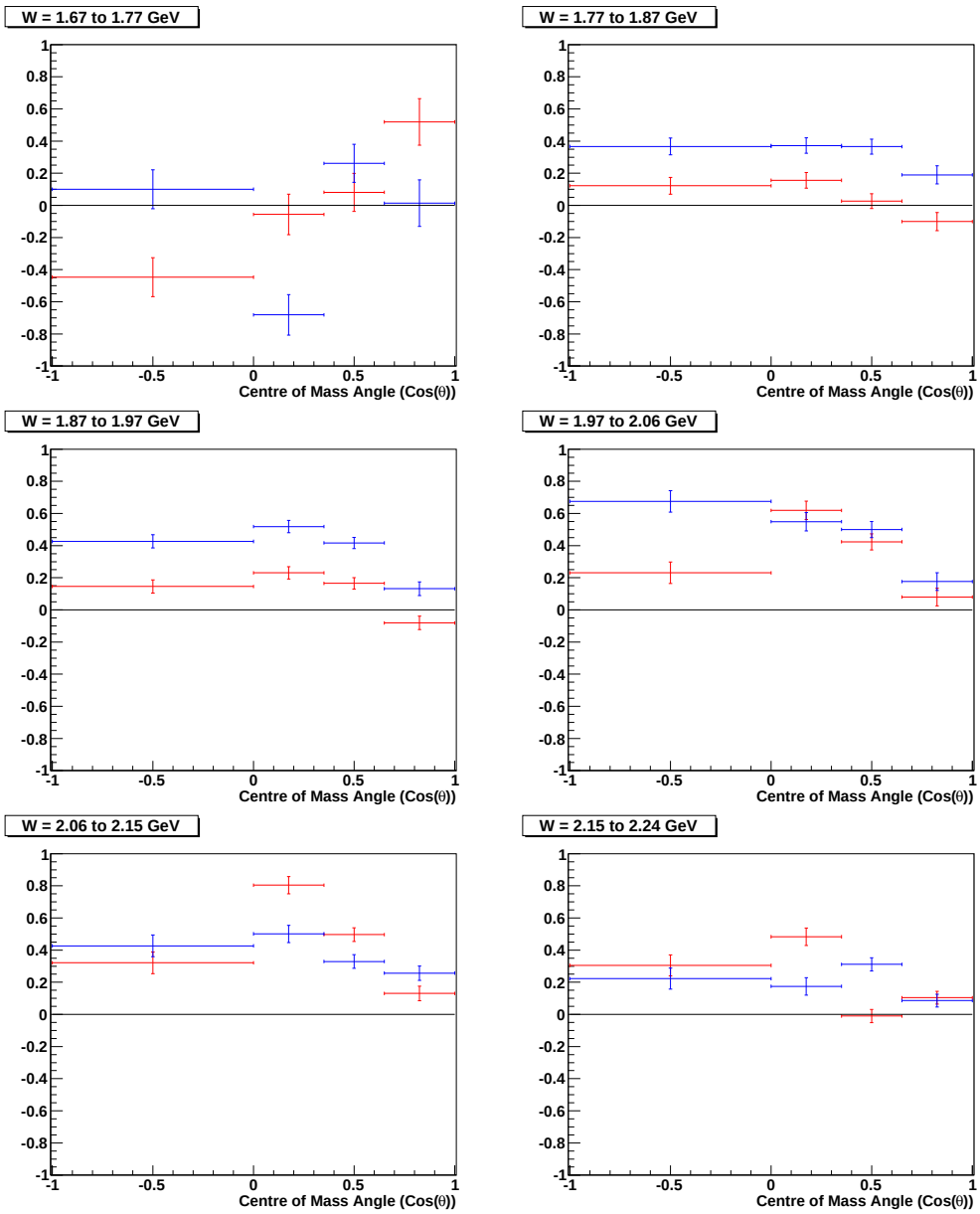

Figure 7.12: G observable for $K^+\Sigma$ as a function of $cos(\theta^{K+}_{cm})$ for W bin centres ranging from 1.715 to 2.195 GeV. Red points indicate the positively polarised target and blue points the negatively polarised target.

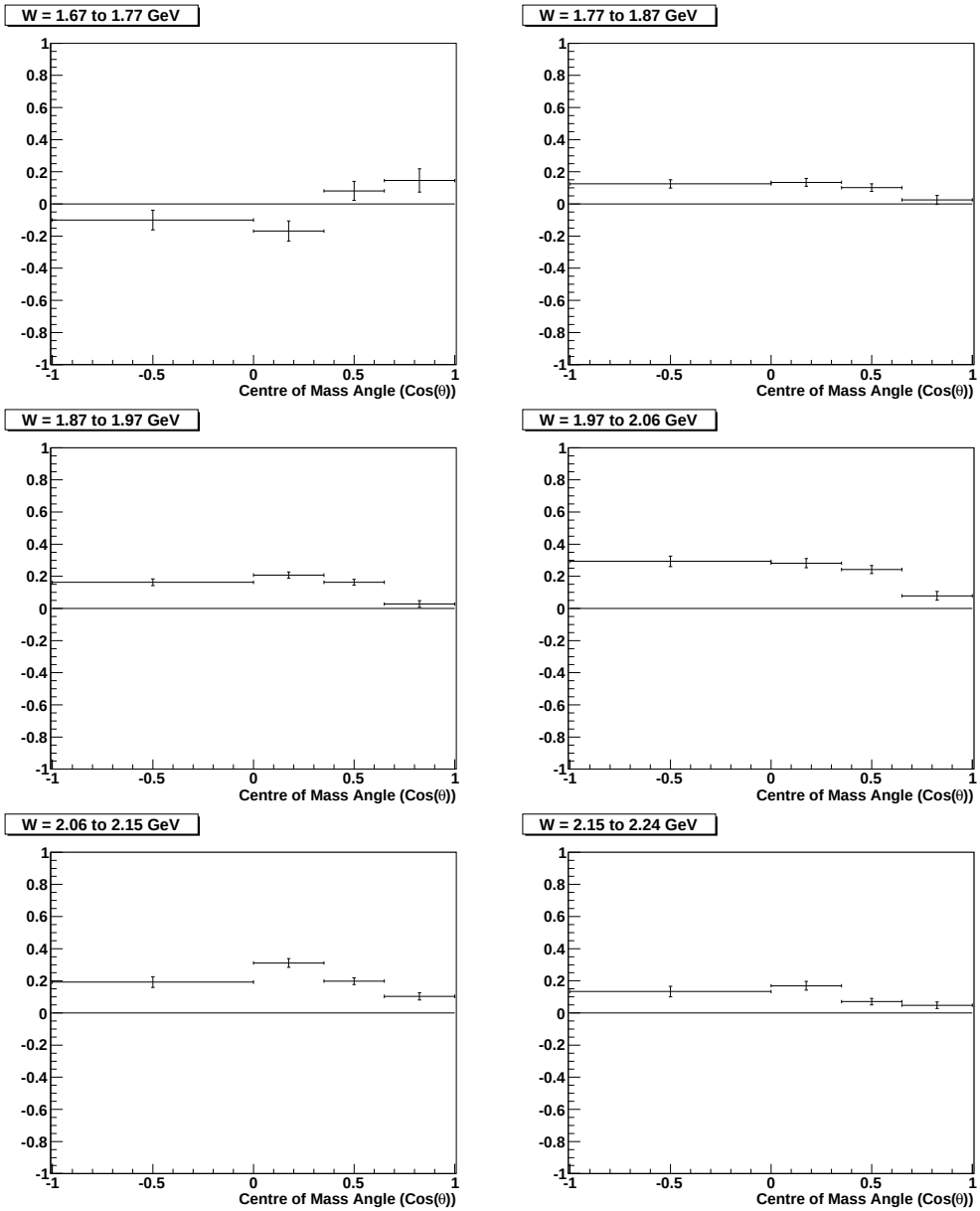

Figure 7.13: Mean of the positive and negative G observable measurements for $K^+\Sigma$as a function of $cos(\theta^{K+}_{cm})$ for W bin centres ranging from 1.715 to 2.195 GeV.

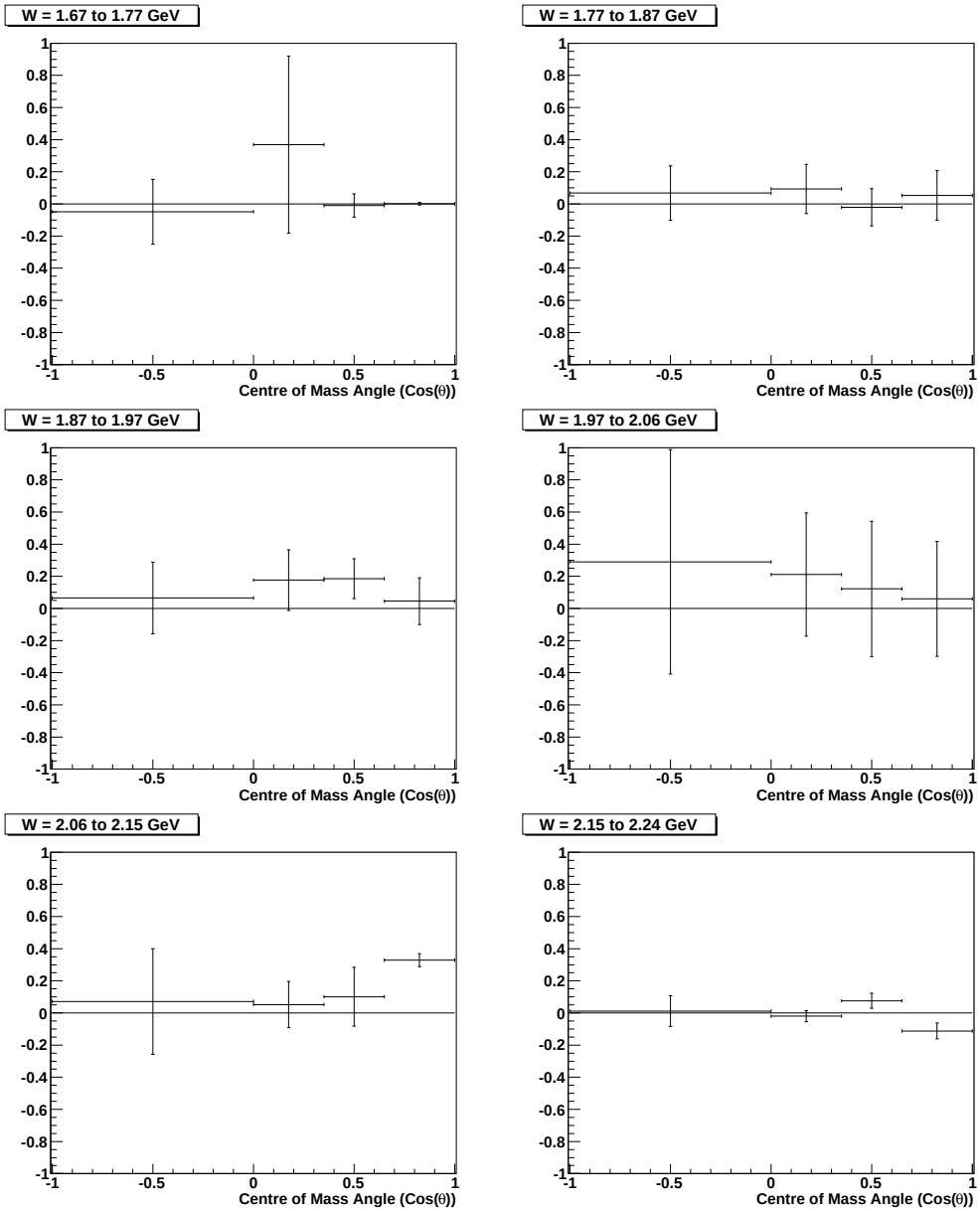

Figure 7.14: G observable for $K^+\Sigma$ from the double asymmetry as a function of $cos(\theta^{K+}_{cm})$ for W bin centres ranging from 1.715 to 2.195 GeV.

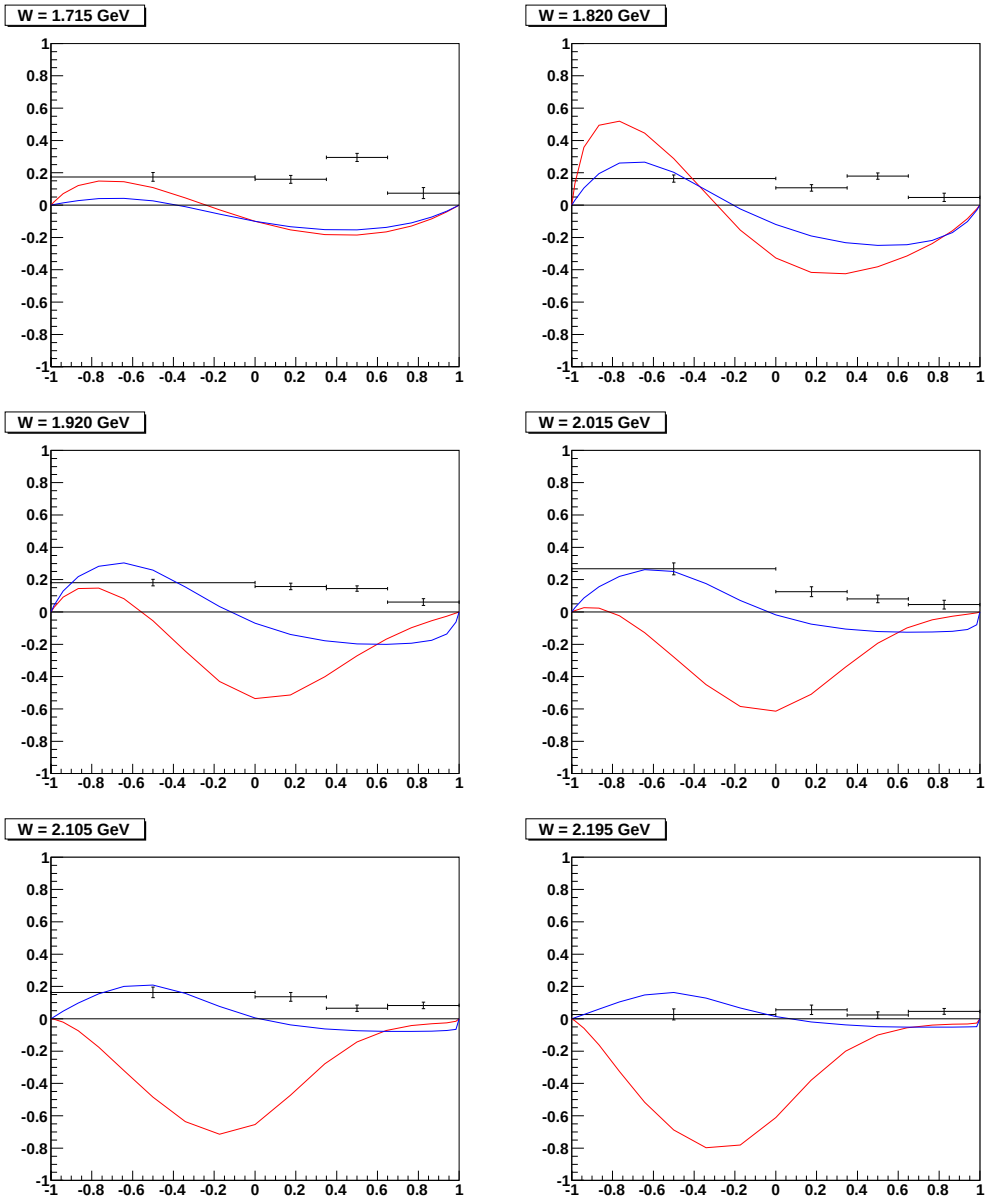

Figure 7.15: Mean values of the G observable for $K^+\Lambda$ compared with model predictions (red line represents Kaon-MAID with D_{13}, the blue line without)

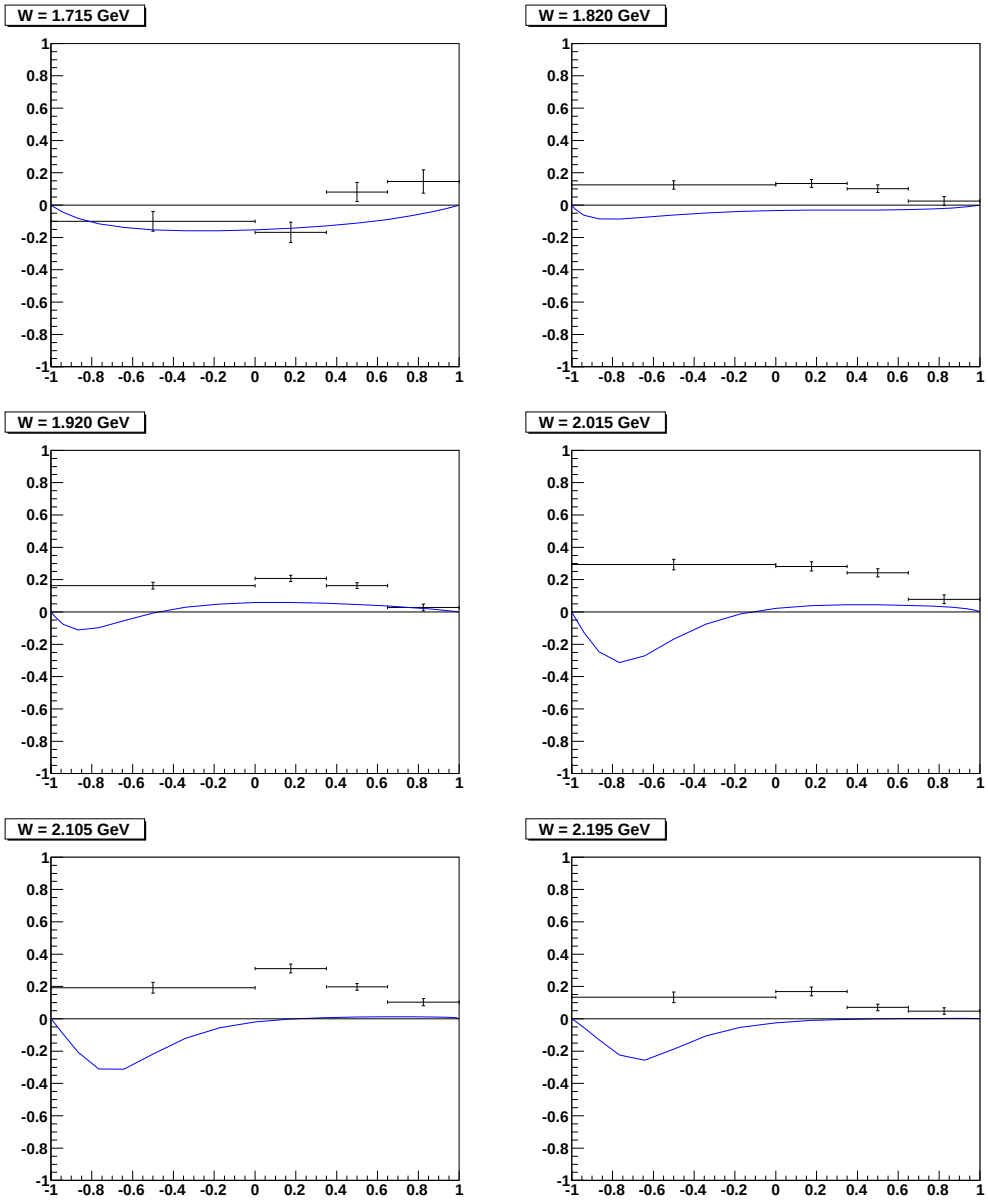

Figure 7.16: Mean values of the G observable for $K^+\Sigma$ compared with model predictions (blue line represents the Kaon-MAID prediction for $K^+\Sigma$)

7.4 Discussion of G Observable Results

Before the polarisation and dilution effects are taken into account, the $P_\gamma P_{target} G$ measurements on butanol for both $K^+\Lambda$ and $K^+\Sigma^0$ extracted for each state of target polarisation display similar magnitudes and opposite sign in each bin. The existence of several bins which do not obey this expected observation offers some explanation of the difficulty in obtaining consistent results between the target polarisation states once polarisation and dilution are accounted for, and the problems encountered in separating the G observable from the phase offset angle when measuring G via the asymmetry of beam polarisation states.

The double asymmetry measurements are also somewhat limited, by both a lack of available data and insufficient constraint in the fit of the Σ observable. Despite these problems, in bins where the double asymmetry fit does not fail completely, the values obtained have been consistent with the mean values of G measured over the two target polarisation states.

For both $K^+\Lambda$ and $K^+\Sigma^0$, the G observable appears to be positive over the entire kinematic range, with the exception of the backward angles for $K^+\Sigma^0$ near threshold energy.

When compared with the predictions of the Kaon-MAID model, some agreement between the $K^+\Lambda$ predictions without the D_{13} resonance can be seen, with the W = 2.015 results following the general trend of the line. For $K^+\Sigma^0$, several energy bins track the trend of the Kaon-MAID line, although no definitive conclusions should be drawn from such preliminary measurements.

7.5 Conclusions

This thesis presents the first, preliminary, measurements of the Σ and G polarisation observables from strangeness photoproduction on a frozen spin polarised target, for the $\gamma p \rightarrow K^+\Lambda$ and $\gamma p \rightarrow K^+\Sigma^0$ reactions. In addition, measurements of the photon asymmetry, Σ, and their agreement with previous CLAS measurements, have shown that polarisation observables can be measured on the target materials used in this experiment and that the background and dilution effects associated with such a

target can be accounted for.

The results for the G observable for the $K^+\Lambda$ channel tend not to agree with the available Kaon-MAID predictions, either with or without the presence of the missing D_{13} resonance. However, at higher energies the data does begin to show some behaviour that better matches Kaon-MAID when the D_{13} resonance is not included in the calculation. For $K^+\Sigma$, the calculation does not include any missing resonances, with the data also appearing to follow the trend of the model prediction, without conclusively matching it. By refitting the models to this new data, better agreement may be possible, and much work remains before the full theoretical implications of these measurements are realised.

Further studies are necessary to explain the inconsistencies between the G measurements for each state of target polarisation, particularly at forward angles, and the limitations encountered by the double asymmetry technique, whose development was intended to negate the need to measure G for individual states of target polarisation.

The inconsistencies between the target states are further exaggerated once dilution of the butanol data is accounted for to estimate G on the proton. The dilution calculation applied is identical across the entire $cos(\theta^{K^+}_{cm})$ range, and the assumption of invariant dilution across the entire angular range may be one reason for the differing values of G for each polarisation state. Time was not available to study this in more detail, and a lack of carbon data hampered preliminary attempts to calculate the dilution in each bin.

Another difficulty in obtaining reliable measurements of G between the target states is the separation of G from the phase offset angle, ϕ_0, as the observable manifests itself as a phase shift in the asymmetry of beam polarisation states. A measurement of the phase offset angle on the higher statistics pion photoproduction data from this experiment would be an important step in improving the reliability of measurements of the G observable.

In the double asymmetry, the constraint of parameters was insufficient to allow the fit to obtain values of G without large statistical uncertainties, and with a lack of data these constraints were even more important in successfully measur-

ing G. Constraining the parameter in the double asymmetry associated with the Σ observable using previous measurements, which have smaller errors than those obtained in this work, may allow the double asymmetry technique to measure G with reduced uncertainty. This would require additional work to take account of the current construction of the double asymmetry, whose Σ constraints are the undiluted measurements on the butanol target, whereas other data are from a free proton target.

It is anticipated that forthcoming analysis of the systematics of the beam polarisation, and a comparison of the scaling factors and resulting dilution of observables with higher statistics channels, such as single pion photoproduction will act to enable improved measurements on the strangeness channels. This, coupled with further investigations of the methods of extracting G from the available data, including the application of Bayesian techniques to the extraction of observables, will move these first measurements for $K^+\Lambda$ and $K^+\Sigma$ towards publishable status.

Bibliography

[1] S. Schadmand. Photoabsorbtion and photoproduction on nuclei in the resonance region. In *Proceedings of the first workshop on quark-hadron duality and the transition to pQCD*, 2005.

[2] D.H. Perkins. *Introduction to High Energy Physics*. Cambridge University Press, 4th edition, 2000.

[3] M. Gell-Mann and Y. Ne'eman. *The Eightfold Way*. W.A. Benjamin, 1964.

[4] R.G. Edwards, J.J. Dudek, D.G. Richards, and S.J. Wallace. Excited state baryon spectroscopy from lattice QCD. *Physical Review D*, 84:074508, 2011.

[5] Roman Koniuk and Nathan Isgur. Baryon decays in a quark model with chromodynamics. *Physical Review D*, 21:1868, 1980.

[6] Simon Capstick and Nathan Isgur. Baryons in a relativized quark model with chromodynamics. *Physical Review D*, 34:2809, 1986.

[7] Simon Capstick. Photo- and electroproduction of nonstrange baryon resonances in the relativized quark model. *Physical Review D*, 46:2864, 1992.

[8] C.P. Forsyth and R.E. Cutkosky. A quark model of baryons with natural flavor. *Z. Phys. C*, 18:219, 1983.

[9] C. Amsler et al. (Particle Data Group). Review of particle physics. *Physics Letters B*, 667:1, 2008.

[10] F. Close, S. Donnachie, and G. Shaw. *Electromagnetic Interactions and Hadronic Structure*. Cambridge University Press, 2007.

[11] G-Y. Chen, S. Kamalov, S.N. Yang, D. Drechsel, and L. Tiator. Excitation of S_{11} resonances in pion scattering and pion photoproduction on the proton. *Nuclear Physics A*, 723(3-4):447 – 463, 2003.

[12] T-S H Lee and L C Smith. Study of nucleon resonances with electromagnetic interactions. *Journal of Physics G: Nuclear and Particle Physics*, 34(7), 2007.

[13] Simon Capstick and W. Roberts. Strange decays of nonstrange baryons. *Physical Review D*, 58:074011, 1998.

[14] A.M. Sandorfi, S. Hoblit, H. Kamano, and T-S.H. Lee. Determining pseudoscalar meson photoproduction amplitudes from complete experiments. *Journal of Physics G: Nuclear and Particle Physics*, 38(5), 2011.

[15] G. Källén. *Elementary Particle Physics*. Addison-Wesley, 1964.

[16] R.K. Bradford, R.A. Schumacher, G. Adams, M.J. Amaryan, et al. First measurement of beam-recoil observables C_x and C_z in hyperon photoproduction. *Phys. Rev. C*, 75:035205, 2007.

[17] RA Adelseck and B. Saghai. Kaon photoproduction: Data consistency, coupling constants, and polarization observables. *Physical Review C*, 42(1):108–127, 1990.

[18] G.F. Chew, M.L. Goldberger, F.E. Low, and Y. Nambu. Relativistic dispersion relation approach to photomeson production. *Physical Review*, 106(6):1345, 1957.

[19] IS Barker, A. Donnachie, and JK Storrow. Complete experiments in pseudoscalar photoproduction. *Nuclear Physics B*, 95(2), 1975.

[20] W-T. Chiang and F. Tabakin. Completeness rules for spin observables in pseudoscalar meson photoproduction. *Phys. Rev. C*, 55:2054–2066, 1997.

[21] B. Saghai. From known to undiscovered resonances. Invited talk at International Symposium on Hadrons and Nuclei, Seoul, nucl-th/0105001, 2001.

[22] T. Mart and C. Bennhold. Evidence for a missing nucleon resonance in kaon photoproduction. *Physical Review C*, 61:012201, 1999.

[23] F.J. Klein et al. Search for missing nucleon resonances in the photoproduction of hyperons using a polarized photon beam and a polarised target. *Jefferson lab experimental proposal*, (E-02-112), 2003.

[24] M. Dugger and E. Pasyuk et. al. Measurement of polarization observables in eta-photoproduction with CLAS. *Jefferson lab experimental proposal*, (E-05-012), 2004.

[25] N. Benmouna et. al. Pion photoproduction from a polarised target. *Jefferson lab experimental proposal*, (E-03-105), 2003.

[26] R. Schumacher et al. Electromagnetic production of hyperons. *Jefferson lab experimental proposal*, (E-89-004), 1989.

[27] A.M. Sandorfi F.J. Klein et al. N* resonances in Pseudoscalar-meson photoproduction from Polarized Neutrons in $\vec{H}$ $\vec{D}$ and a complete determination of the $\gamma n \rightarrow K^0\Lambda$ amplitude. *Jefferson lab experimental proposal*, (E-06-101), 2006.

[28] V.D. Burkert. The N* Physics Program at Jefferson Lab. *Chinese Physics C*, 33(12):1043, 2009.

[29] BA Mecking, G. Adams, S. Ahmad, et al. The CEBAF large acceptance spectrometer (CLAS). *Nuclear Inst. and Methods in Physics Research, A*, 503(3):513–553, 2003.

[30] C.D. Keith. The jlab frozen spin target. In *Proceedings of the 18th international spin physics symposium, Charlottesville, VA*, 2008.

[31] R.L. Anderson, E. Gabathuler, D. Jones, B.D. McDaniel, and A.J. Sadoff. Photoproduction of K^+ Mesons in Hydrogen. *Physical Review Letters*, 9:131–133, 1962.

[32] D.E. Groom and J.H. Marshall. Λ Polarization at 90° in $K^+\Lambda$ Photoproduction. *Physical Review*, 159:1213–1219, 1967.

[33] H. Göing and W. Schorsch and J. Tietge and W. Weilnböck. Photoproduction of $K^+\Lambda$ and $K^+\Sigma^0$ in Hydrogen Between 1.19 and 1.68 GeV. *Nuclear Physics B*, 26:121–133, 1971.

[34] W.J. Schwille, M. Bockhorst, G. Burbach, et al. Design and construction of the SAPHIR detector. *Nuclear Inst. and Methods in Physics Research A*, 344(3):470 – 486, 1994.

[35] A. Sarantsev, V. Nikonov, A. Anisovich, E. Klempt, and U. Thoma. Decays of baryon resonances into ΛK^+, ΣK^+ and $\Sigma^+ K^0$. *European Physical Journal A*, 25:441–453, 2005.

[36] J.W.C. McNabb, R.A. Schumacher, L. Todor, G. Adams, et al. Hyperon photoproduction in the nucleon resonance region. *Phys. Rev. C*, 69:042201, 2004.

[37] R. Bradford, R.A. Schumacher, J.W.C. McNabb, L. Todor, et al. Differential cross sections for $\gamma + p \rightarrow K^+ + Y$ for Λ and Σ hyperons. *Phys. Rev. C*, 73:035202, 2006.

[38] R. Erbe et al. Multipion and strange-particle photoproduction on protons at energies up to 5.8 GeV. *Physical Review*, 188:2060, 1969.

[39] C.A. Paterson. *Polarization Observables in Strangeness Photoproduction with CLAS at Jefferson Lab.* PhD thesis, University of Glasgow, 2008.

[40] P. Nadel-Turonski et al. Kaon production on the deuteron using polarized photons. *Jefferson lab experimental proposal*, (E-06-103), 2006.

[41] J.R. Johnstone. *The Photon Beam Asymmetry for KY Production from the Bound Proton in Deuterium.* PhD thesis, University of Glasgow, 2009.

[42] N. Hassall. *Spin Observables in Kaon Photoproduction from the Bound Neutron in a Deuterium target with CLAS.* PhD thesis, University of Glasgow, 2010.

[43] R.G.T. Zegers, M. Sumihama, D.S. Ahn, J.K. Ahn, et al. Beam-Polarization Asymmetries for the $p(\vec{\gamma}, K^+)\Lambda$ and $p(\vec{\gamma}, K^+)\Sigma^0$ Reactions for E_γ = 1.5-2.4 GeV. *Phys. Rev. Lett.*, 91:092001, 2003.

[44] T. Mart et al. Kaon-MAID - An effective Lagrangian Model for Kaon Photo- and Electroproduction on the Nucleon, 2000. www.kph.uni-mainz.de/maid/kaon/kaonmaid.html.

[45] S. Janssen, J. Ryckebusch, D. Debruyne, and T. Van Cauteren. Σ photoproduction in the resonance region. *Physical Review C*, 66:035202, 2002.

[46] J.P. Bocquet, J. Ajaka, M. Anghinolfi, V. Bellini, et al. GRAAL: a polarized γ-ray beam at ESRF. *Nuclear Physics A*, 622(1-2):c124 – c129, 1997.

[47] A. Lleres, O. Bartalini, V. Bellini, J. Bocquet, et al. Polarization observable measurements for $\gamma p \rightarrow K^+\Lambda$ and $\gamma p \rightarrow K^+\Sigma$ for energies up to 1.5 GeV. *European Physical Journal A*, 31:79–93, 2007.

[48] A. Lleres, O. Bartalini, V. Bellini, J. Bocquet, et al. Measurement of beam-recoil observables O_x, O_z and target asymmetry T for the reaction $\gamma p \rightarrow K^+\Lambda$. *European Physical Journal A*, 39:149–161, 2009.

[49] P.J. Bussey, J.G. Rutherglen, P.S.L. Booth, et al. Measurements of the double polarisation parameters G and H in neutral pion photoproduction. *Nuclear Physics B*, 159:383–396, 1979.

[50] St. Goertz, W. Meyer, and G Reicherz. Polarized H, D, and ^{3}He Targets for Particle Physics Experiments. *Progress in Particle and nuclear Physics*, 49:403–489, 2002.

[51] M. Rost et al. Measurement of the G asymmetry in $\gamma p \rightarrow p\pi^0$ and $\gamma p \rightarrow n\pi^+$. *MAMI A2 experimental proposal.*

[52] L.R. Casey. *The Search for Missing Resonances in $\gamma p \rightarrow K^+\Lambda$ Using Circularly Polarized Photons on a Longitudinally Polarized Frozen Spin Target.* PhD thesis, The Catholic University of America, 2011.

[53] V. Shyklar, H. Lenske, and U. Mosel. Coupled-channel analysis of $K\Lambda$ photoproduction in the nucleon resonance region. *Physical Review C*, 72:015210, 2005.

[54] T. Corthals, J. Ryckebusch, and T. Van Cauteren. Forward-angle $K^+\Lambda$ photoproduction in a regge-plus-resonance approach. *Physical Review C*, 73:045207, 2006.

[55] Thomas Jefferson National Accelerator Facility. Jefferson lab webpage. www.jlab.org.

[56] C.W. Leemann, D.R. Douglas, and G.A. Krafft. The Continuous Electron Beam Accelerator Facility: CEBAF at the Jefferson Laboratory. *Annu. Rev. Nucl. Part. Sci*, 51:413–50, 2001.

[57] J. Hansknecht and M. Poelker. Synchronous photoinjection using a frequency-doubled gain-switched fiber-coupled seed laser and ErYb-doped fiber amplifier. *Phys. Rev. ST Accel. Beams*, 9:063501, 2006.

[58] U.S. Department of Energy/National Science Foundation Nuclear Science Advisory Committee. Opportunities in nuclear science: A long-range plan for the next decade. Nuclear Science Advisory Committee Long Range Plan, 2002.

[59] U. Timm. Coherent bremsstrahlung of electrons in crystals. *Fortschritt der Physik*, 17:765–808, 1969.

[60] D.I. Sober, H. Crannell, A. Longhi, et al. The bremsstrahlung tagged photon beam in hall b at jlab. *Nuclear Inst. and Methods in Physics Research, A*, 440:263–284, 2000.

[61] J. D. Kellie and P.J.M. Clive. The selection and performance of diamond radiators used in coherent bremsstrahlung experiments. *Nuclear Instruments and Methods in Physics Research A*, 545:164–180, 2005.

[62] G.L. Yang, R. Jones, F. Klein, K. Finkelstein, and K. Livingston. Rocking curve imaging for diamond radiator crystal selection. *Diamond & Related Materials*, 19:719, 2010.

[63] S. Taylor, S. Ahmad, J. Disteilbrink, G. S. Mutchler, E. Smith, and T. Smith. The CLAS start counter. *Nuclear Inst. and Methods in Physics Research, A*, 462(3):484–493, 2001.

[64] Y.G. Sharabian, M. Battaglieri, V.D. Burkert, R. DeVita, et al. A new highly segmented start counter for the CLAS detector. *Nuclear Inst. and Methods in Physics Research, A*, 556(1):246–258, 2006.

[65] M.D. Mestayer, D.S. Carman, et al. The CLAS drift chamber system. *Nuclear Inst. and Methods in Physics Research, A*, 449(1):81–111, 2000.

[66] G. Adams, V. Burkert, et al. The CLAS cerenkov detector. *Nuclear Inst. and Methods in Physics Research, A*, 465:414–427, 2001.

[67] E.S. Smith, T. Carstens, et al. The time-of-flight system for CLAS. *Nuclear Inst. and Methods in Physics Research, A*, 432:265–298, 1999.

[68] M. Amarian, G. Asryan, et al. The CLAS foward electromagnetic calorimiter. *Nuclear Inst. and Methods in Physics Research, A*, 460:239–265, 2001.

[69] C.D. Jeffries. Dynamic orientation of nuclei by forbidden transitions in paramagnetic resonance. *Physical Review*, 117:1056, 1960.

[70] Y.A. Prok. *Measurement of the spin structure function $g_1(x,Q^2)$ of the proton in the resonance region.* PhD thesis, University of Virginia, 2004.

[71] Chris Keith. Frozen spin targets in a nutshell iii: results. Jefferson Lab Seminar, 2008.

[72] C.D. Keith, M. Anghinolfi, M. Battaglieri, P. Bosted, et al. A polarized target for the clas detector. *Nuclear Instruments and Methods in Physics Research A*, 501:327–339, 2003.

[73] *Encyclopedia of Reagents for Organic Synthesis.* John Wiley and Sons, Chichester, 2010.

[74] David S. Betts. *An introduction to millikelvin technology.* Cambridge University Press, Cambridge, first edition, 1989.

[75] F.A. Natter et al. ANB - ANalytic Bremstrahlungs Calculation. www.pit.physik.uni-tuebingen.de/grabmayr/software/brems/brems-analytic.html.

[76] K. Livingston. Linear polarisation tables. Private Communication, 2011.

[77] J. McAndrew. *Measurement of the G Double-Polarisation Observable in Positive Pion Photoproduction*. PhD thesis, University of Edinburgh, 2011.

[78] K. Livingston. ROOTBEER - a package for the analysis and conversion of CLAS BOS format data using ROOT. http://nuclear.gla.ac.uk/∼kl/rootbeer.

[79] R. Brun et al. ROOT. http://root.cern.ch/drupal/.

[80] E. Pasyuk. CLAS-note: Energy loss corrections for charged particles in CLAS. Technical report, 2007.

[81] D. Sokhan. *Beam Asymmetry Measurement from Pion Photoproduction on the Neutron*. PhD thesis, University of Edinburgh, 2009.

[82] S. Chen. *First Measurement of Deeply Virtual Compton Scattering with a polarized proton target*. PhD thesis, Florida State University, 2006.

[83] M. Dugger and B.G. Ritchie. Draft of CLAS-note: Phase space dependent scale factors for FROST g9a data. Technical report, Arizona State University, 2010.

[84] K. Livingston. g8b run list, http://nuclear.gla.ac.uk/ kl/g8b/linpol/allruns2.dat. Private Communication, 2010.

[85] D. J. Hamilton. A phase space event generator for strangeness photoproduction. Private Communication, 2010.

[86] D. G. Ireland. Rebinned g8b data for the $K^+\Lambda$ reaction. Private Communication, 2011.